Bi-state Control of Microelectromechanical Nonlinear and Parametric Resonance

Submitted in partial fulfillment of the requirements for the degree of

Doctor of Philosophy

in

Electrical and Computer Engineering

Congzhong Guo

B.S., Electronic Science and Technology, Zhejiang University (2009)
M.S., Electrical Engineering, Carnegie Mellon University (2011)

Carnegie Mellon University
Pittsburgh, PA

September, 2013

To my parents and sister,

and to my wife Yun,

Their love and patience made this possible.

ACKNOWLEDGMENTS

I would like to begin by thanking all people who brought me one step closer to the completion of my Ph.D. I am grateful for all the insights, supports, encouragement, understanding, and collaboration that helped me throughout my entire four years as an independent researcher at Carnegie Mellon University.

Prof. Gary Fedder, my advisor, a humble friend, and my role model for academic excellence, encouraged and inspired me to pursue truth and quality research. His invaluable guidance paved the way for extending the impact of a single analysis, a complex simulation, and an experimental validation. I will always cherish the days when experiments fail and the wisdom he offers sails me out of the puzzles. Prof. Fedder showed me my responsibility in the research community is to provide the highest standard of ideation, analysis, experimentation, and writing. His professional expertise and creativity, boosted by initiative in implementation and attentiveness to details, sets the standard that I will always carry with me.

I am so lucky to have my wife, Yun, work side-by-side with me through difficulties and obstacles. Her love has always been my source of happiness even though I spent uncounted days and nights in the lab doing experiments and analysis. Her dedication to the family inspires me to strive for excellence. Her sense of humor energizes my work and life with smartness. I can't express how thankful I am to my father, mother, and sister Congjing back at home for their encouragement and continued support for every decision I made. Without their determination and understanding, I would not have completed this thesis work.

ABSTRACT

Parametric resonance provides a sharp jump in resonance amplitude at the bifurcation setpoint and is, therefore, ideal for ultrasensitive detection of mass or stress shifts that modify the resonance frequency and hence the bifurcation frequency. This work investigates a bi-state controller capable of servoing along the microelectromechanical (MEMS) parametric resonant bifurcation point at large displacement amplitudes. The control plant is a large-stroke (8 µm) parametric resonator excited by an in-plane "shaped-finger" electrostatic comb drive fabricated using a 15 µm-thick silicon-on-insulator MEMS (SOI-MEMS) process. The large-stroke parametric resonance and the ability to track the bifurcation jump point promote future implementation of ultrasensitive bifurcation-based chemical gravimetric sensors, strain gauges, and mode-matched gyroscope applications.

The controller feedback states are two levels of the electrostatic-drive voltage that shift the nonlinear resonance characteristics. The system is driven at a fixed frequency. The feedback states correspond to two steady-state conditions: the "on" state experiencing parametric resonance and the "off" state at zero amplitude. The states are cycled by 200 kHz pulse-width-modulation that circumvents the slow hysteretic latch-on that would occur in steady-state operation. The closed-loop control avoids the necessary setup and ring-down time that are required to settle between the "on" and the "off" states. The exemplary system demonstrated has 1.9 µm servo amplitude with a minimum normalized Allan deviation of 2.36×10^{-4}. A second

experimental embodiment of the bi-state bifurcation-based controller uses a crab-leg Duffing resonator to servo at the maximum "on" point (5 μm) prior to the bifurcation jump.

A quadratic capacitance-displacement response is synthesized by engineering a "shaped-finger" comb profile. The excitation of the nonlinear parametric resonance is realized by selecting an appropriate combination of the electrostatic stiffness coefficients through a specific varying-gap comb-finger design. A large frequency tuning range of 17% is demonstrated in an example crab-leg resonator.

A predictive simulation methodology for the nonlinear parametric resonance systems uses elemental behavioral models to compose the system. The mixed MEMS/analog behavioral composable modeling methodology is validated by the characterization of a canonical CMOS-MEMS non-interdigitated comb finger resonator.

TABLE OF CONTENTS

LIST OF TABLES AND LISTINGS

LIST OF FIGURES AND ILLUSTRATIONS

xvi

CHAPTER 1   INTRODUCTION

R esonant-based sensing has long been exploited to gauge micromechanical system parameters such as mass and spring constant. Gravimetric sensors and mass flow meters that measure the mass change and the stress sensors that link to changes in suspension spring constant all exemplify this approach. As harmonic resonators suffer from a direct link between amplitude and frequency noise that degrades sensitivity, there is interest in using a class of nonlinear parametric resonators to develop an extremely sensitive mechanism [1] to detect very small (*e.g.* millihertz) changes in resonance frequency. This improved sensitivity stems from an instantaneous "jump" transition from near-zero to high displacement at the bifurcation frequency.

1.1.   BENEFITS OF PARAMETRIC RESONANCE

One of the benefits of the parametric resonance is the bifurcation phenomenon in the case of a directional sweep of parametric drive frequency in the region around twice the resonant frequency. The bifurcation occurs in a system that exhibits bi-stability. A bi-stable system has two states. A simple example of the bi-stable system is a digital bit which has "0" and "1" states. A state transition from "0" to "1" is analogous to the bifurcation phenomenon. In a parametric resonator, a sharp jump in the mechanical displacement amplitude from zero to a non-zero value takes place at a "pitch-fork" bifurcation frequency. The frequency at which the jump happens

depends upon the direction of the frequency sweep, providing a hysteresis effect. Detecting this sharp jump enables sensitive detection of changes in the resonant frequency, which can either be caused by a change in mass [1] or stress which affects the spring constant.

The bi-stability at the bifurcation point makes measurement of the bifurcation frequency possible to extremely good precision. Because of this ability, this class of nonlinear resonators is a good candidate for highly sensitive mass (*i.e.*, gravimetric) and stress detectors. Measuring the frequency shift on the sharp boundary of the parametric resonance relates directly to any change in the vibrating mass [1]. Compared to a harmonic-mode resonant mass sensor, the parametric-mode gravimetric detector is immune to the injected amplitude noise [2] because the bifurcation response retains its sharpness in the presence of the detection noise. The prior demonstration of attogram mass sensitivity by enhancing frequency resolution in a parametrically excited mass sensor [3] offers motivation for bifurcation–based control [4], which can then result in extremely sensitive detection of mass or stress.

Sensing application

Certain kinds of mechanical and electrostatic nonlinearity give rise to flat and large amplitude response over relatively wide frequency ranges that are potentially useful in making manufacturable resonant devices. Wide-band response of electrostatic drives encompasses mismatched modes and avoids the need for tuning. Matched-mode gyroscopes in the presence of process mismatch [5], scanning tunneling microscopes [6], scanning mirrors [7], and sensors that need motion for chopper stabilization all benefit from this behavior.

Wide-band response

Parametric resonance finds further applications in noise squeezing [8] and signal parametric amplification [9] for effective Q enhancement, mechanical modulation [10], and parasitic signal

Other applications

reduction. Some classes of nonlinear systems can induce chaos [11] and the random motion might be used for random number generation.

1.2.   PARAMETRIC RESONANCE

A system is excited parametrically when its state is modified by time-varying parameters. A Definition classic example is a pendulum with its rotational moment of inertia varying at twice the resonant frequency to "pump" it into resonance. In electrostatically driven resonant MEMS, the most effective time-varying parameter arises from nonlinear electrostatic actuators that introduce an equivalent electrostatic stiffness that varies with excitation voltage. The mechanical flexure stiffness is another design variable that is set by spring topology and dimensions and that can be set to intentionally introduce essential nonlinearity to the system behavior. Turner *et al.* [6] experimentally measured five parametric resonant modes in a torsional oscillator, and verified that, as predicted by theory, parametric resonance occurs near drive frequencies of $2\omega_r / n$, where ω_r is the natural mechanical resonant frequency and n is an integer larger or equal to 1. The scope of this work covers the principal parametric resonance occurring at twice the resonant frequency ($2\omega_r$).

The harmonic and parametric resonators differ in the way the resonance is excited. The Parametric force harmonic resonator has a fixed spring constant, with an external drive that is sinusoidal in time t and invariant in displacement x. Electrostatically-driven parametric excitation arises when the electrostatic force applied on a MEMS resonator is not only a function of the time but also a function of the displacement of the resonator [15]. An electrostatic drive actuates the parametric

3

resonator at an electrical frequency, ω_d, which creates a time-varying displacement-dependent spring constant, k_{eff}. Parametric resonance conditions are satisfied when the periodic variation of k_{eff} is at twice the resonance frequency, *i.e.*, $\omega_d = 2\omega_r$. A typical electrostatic sinusoidally varying parametric force, F_p, can be expressed as

$$F_p = -\left(\gamma_1 x + \gamma_3 x^3\right)\left[V_{dc}^2 + V_{ac}^2 \cos(2\omega_r t)\right] \tag{1.1}$$

where t is time, x is the x-directed displacement of the mass, and V_{dc} and V_{ac} are the voltages applied on an electrostatic drive comb that are designed to create a voltage-controlled linear spring constant, γ_1, along with a cubic-displacement nonlinearity, γ_3.

The second-order differential equation describing a mass-spring-damper system is

Mathieu
equation

$$m\,\ddot{x} + b\,\dot{x} + k_1 x + k_3 x^3 = F_p(t, x) \tag{1.2}$$

where m is mass, b is the damping coefficient, and k_1 and k_3 are linear and cubic spring constants, respectively. $\dot{x}$ is the first derivative of x with respect to time t. Substituting the force in (1.1) into (1.2) and rearranging terms yields a nonlinear Mathieu equation

$$m\,\ddot{x} + b\,\dot{x} + \left(k_1 + \gamma_1 V_{dc}^2\right)x + \left(k_3 + \gamma_3 V_{dc}^2\right)x^3 = -\left(\gamma_1 x + \gamma_3 x^3\right)V_{ac}^2 \cos(2\omega_r t) \tag{1.3}$$

An example of parametric excitation is conceptually shown in Figure 1-1. A block material Example suspended by a spring experiences a parametric excitation in the form of (1.1). Simplifying (1.1) by enforcing $V_{dc} = 0$ and $\gamma_3 = 0$, (1.1) can be rewritten as

$$F_p = -\gamma_1 x\, V_{ac}^2 \cos(2\omega_r t) \tag{1.4}$$

The waveforms of the displacement, x, velocity, $\dot{x}$, parametric voltage, $V_{p,ac}\cos(2\omega_r t)$, and parametric force, F_p, are plotted in Figure 1-2. The applied parametric force is always in the
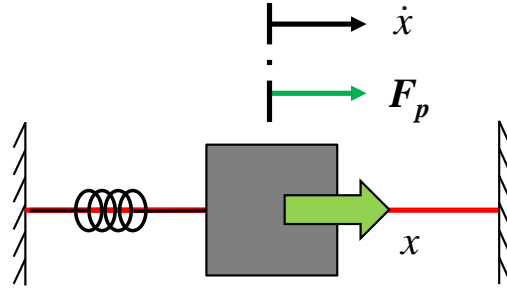
Figure 1-1: A block material suspended by a spring experiencing a parametric excitation.
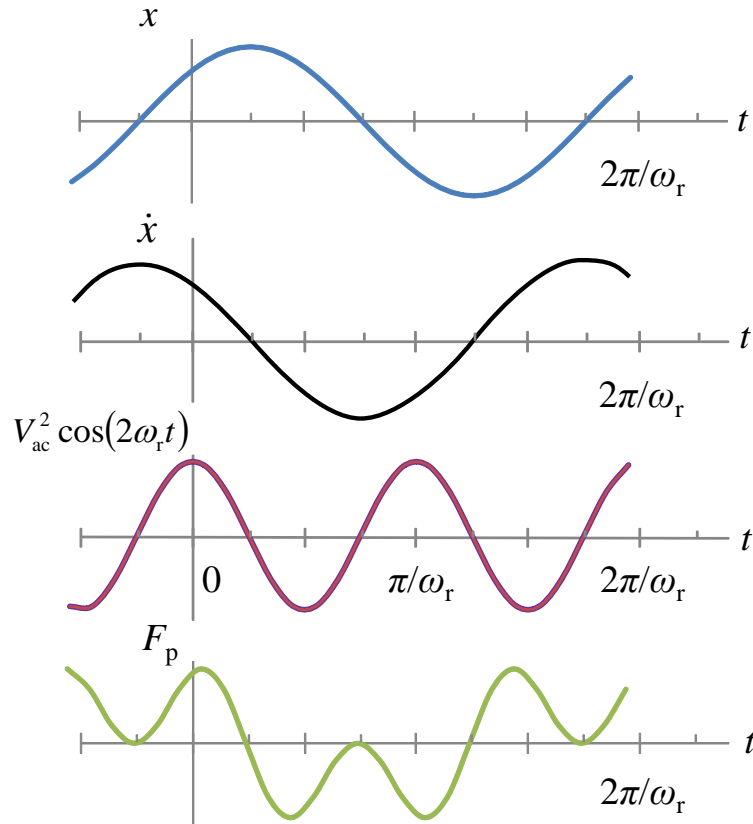
Figure 1-2: The waveforms of the displacement, x, velocity, $\dot{x}$, parametric voltage, $V_{p,ac}\cos(2\omega_r t)$, and parametric force, F_p, for the conceptual example in Figure 1-1.

same direction of the velocity, pumping energy into the system at a rate equal to twice the system's resonant frequency.

One solution to (1.3) is $x = 0$. The parametric force degenerates to zero when the resonator is at rest, which is generally realized by symmetric electrode design [16] that is force-balanced when the displacement is zero. With the existence of thermomechanical noise due to the air damping, a very small but non-zero noise displacement on the order of 10 fm/rtHz is present and as a result, the force becomes non-zero and is proportional to the displacement. In a second-order mechanical system, electrostatic mechanical force exerted on a moving mass acts like a spring. This electrostatic spring constant is controlled by the applied voltage. With non-zero displacement and parametric drive voltage, the mass-spring-damper system periodically increases (hardens) or decreases (softens) the total effective spring constant. The excitation parametric force and the velocity of the resonator are in phase, pumping the mass into parametric resonance at $2\omega_r$.

Qualitative description of parametric resonance

When parametrically excited, the effective spring constant is periodically modified twice within one period of the oscillation by the time-varying pump voltage. The system establishes parametric resonant amplification which builds exponentially-growing oscillation amplitude. The pumped displacement amplitude and phase are strong functions [17] of the system parameters such as the resonator mass, mechanical spring constant, and electrostatic spring constant of the actuator that excites the parametric resonance. The exponential growth is limited by the mechanical and electrostatic nonlinearities; the latter is controlled by the drive voltage. Detailed description of the perturbation analysis in solving (1.3), and the amplitude and phase responses can be found in Appendix A and [40].

1.3. EXCITATION OF PARAMETRIC RESONANCE

Parametric excitation in (1.1) arises from several different electromechanical drive Electro-static parametric excitation topologies. One simple example is a parallel-plate capacitive voltage-force transducer (shown in Figure 1-3 (a)), which provides a linear softening electrostatic spring constant for sufficiently small displacement relative to the gap. A class of non-interdigitated finger (NIF) comb drives [16], [17], and [18] (Figure 1-3 (b)) has been widely used to provide a well-defined displacement-dependent force source. The NIF comb drive is constrained to move in a direction orthogonal to the finger length and makes use of the fringing electric field generated between non-overlapping comb fingers. Both the linear and cubic stiffness can be independently tuned by the percentage of the finger width to its pitch [19] so the parametric frequency response can be adjusted correspondingly.
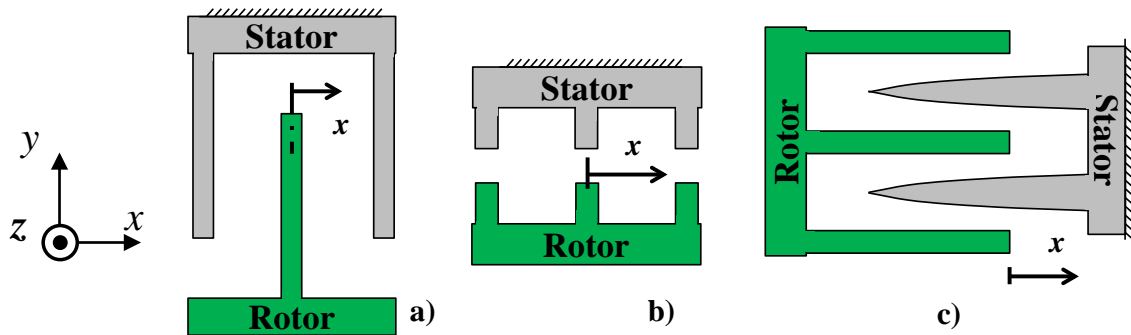
Figure 1-3: Methods of achieving parametric excitation in the form of (1.1) include (a) parallel-plate drive, (b) NIF, and (c) shaped-finger comb. x indicates the direction of motion.

However, the NIF design is limited in displacement stroke to a maximum of $\pm 1/2$ of the Limitation of NIF

comb pitch (usually on the order of $1\,\mu m$). This design constraint is due to the necessary

nonlinearity required to excite the parametric resonance. Many applications, *e.g.*,

gyroscopes [20] and scanning mirrors, benefit from a large motional stroke to provide a better

signal-to-noise ratio.

Towards this end, a compact electrostatic comb is synthesized to have a large stroke with a Benefits of shaped-finger comb

small design footprint. This "shaped-finger" comb (Figure 1-3 (c)) utilizes a nonlinearly varying

electrode gap to provide the necessary electrostatic stiffness for exciting parametric resonance

with much larger stroke (up to $8\,\mu m$). Like the parallel-moving straight-finger capacitive comb

(the same comb as Figure 1-3 (a) but moves in *y*), the shaped-finger comb moves laterally in the

plane of the wafer, allowing sufficient clearance for large displacement motion. For a resonator

that utilizes the shaped-finger comb, separate linear displacement sensing combs can be included

to electronically measure the parametric resonance in these large-stroke systems.

The shaped-finger comb concept was originally introduced by Hirano [21] to achieve a Prior art

smaller gap beyond the fabrication constraints. Further studies of the finger shape focus on its

tuning applications, in which the planar comb shape is designed such that an electrostatic force

with specific nonlinearity is applied. The analytic model and its tuning dynamics were reported

in [22] and [25]. Several patents also cover a variety of in-plane curved features [23] and out-of-

plane shaped structures using chemical mechanical polishing [24].

The possibility of a shaped-finger comb in exciting the parametric mode was briefly Thesis contribution

mentioned in a prior paper [22] but no further work was done. This work presents analysis,

simulation, and experimental validation of large-stroke parametric resonance using a "quadratic-shaped-finger" comb. Study of the shaped-finger comb in exciting high-stroke parametric resonance represents a major contribution of this thesis. A quadratic-shaped-finger comb parametric drive and the characterization of a nonlinear parametric resonator utilizing this class of comb design will be discussed in detail in Chapter 3.

1.4.   NONLINEAR MATHIEU EQUATION AND PERTURBATION ANALYSIS

Quantitative descriptions of MEMS parametric resonance have been extensively studied in [17], [16], and [18] by solving the nonlinear Mathieu equation with perturbation techniques. The governing nonlinear Mathieu equation (1.3) of the nonlinear resonators under investigation is a second-order differential equation with an oscillating external excitation, which is difficult to solve analytically. Perturbation techniques [15] provide a mathematical approach to an estimated solution. In particular, the method of multiple scales and the method of averaging [17], [18], and [30] provide an approximate closed-form solution to (1.3).

Perturbation technique

The perturbation approach starts with normalizing (in Appendix A.1) the dimensional equation into a general form. It then finds the steady-state amplitude and phase solutions, *i.e.* equilibria, using the method of averaging [30], and linearizes the equations about these equilibria. The details of the derivations are located in Appendix A.2 and A.3. The stability of these equilibria, described in Appendix A.4, is determined by allowing the system state to move along the linearized approximation by a small amount.

Procedures of perturbation technique

This work expands on the perturbation method used in [17] and details the stability analysis using a two-step straightforward linear transformation, in the interest of establishing the relationship between the transition frequencies and amplitudes with system parameters. In this section, we will focus on three important aspects of the Mathieu equation solutions: the steady-state amplitudes; the bifurcation frequencies, *i.e.*, the transition frequencies between the "stable" and "unstable" states; and the frequency response. The steady-state frequency response plots the steady-state amplitude versus the frequency of the sweep and denotes the stability of each amplitude solution branch.

1.4.1. NONLINEAR MATHIEU EQUATION

The equation of motion of a nonlinear parametric resonator describes a mass-spring-damper system with linear and cubic stiffness coefficients, driven by an electrostatic force that is not only a function of time but also of the displacement. The nonlinear Mathieu equation (1.3) may be written into the more general form:

$$m\,\ddot{x} + b\,\dot{x} + k_1 x + k_3 x^3 = F_p(t,x) = -\left(\gamma_1 x + \gamma_3 x^3\right)V^2\,, \tag{1.5}$$

Taking MEMS resonators described in Appendix B as examples, the sources of damping are usually dominated by the Couette damping of the plate mass interacting with the underlying substrate, as well as Stokes damping of the plate, and the squeeze-film damping between the gaps of any interdigitated comb fingers that are used as the capacitive sensing electrostatic drive.

At rest, the damping force, $b\dot{x}$, and inertial force, $m\ddot{x}$, are zero valued. In this case, the spring force, $k_1 x + k_3 x^3$, is equal to the parametric force term, $-\left(\gamma_1 x + \gamma_3 x^3\right)V^2$, and $x = 0$ is a

solution. The parametric force, F_p, exerted by the nonlinear electrostatic drive is an odd function of the displacement. The force term, F_p, is generally realized by a symmetric electrode actuator design [16] (*i.e.*, drive combs located on both sides of the resonating mass) that is force-balanced when the displacement is zero (*i.e.,* $F_p = 0$). In the presence of thermomechanical noise due to the air damping, a small displacement takes place and as a result, the force becomes non-zero and is approximately proportional to the displacement for these small motions. When the parametric excitation frequency is around twice the natural frequency, the excitation parametric force and the velocity of the resonator are in phase, pumping the device into resonance, as graphically shown in Figure 1-2. The effective spring constant is modified twice within one period of the oscillation by the time-varying pump voltage. The pumped displacement amplitude and phase are strong functions [17] of the system parameters, which include the resonator mass, the mechanical spring constant, and the electrostatic spring constant of the actuator.

1.4.2. PARAMETRIC DRIVE AND PARAMETRIC FORCE

The voltage applied across the parametric excitation comb fingers is

Drive
voltage

$$V(t) = V_{p,dc} + V_{p,ac} \cos(\omega_d t), \tag{1.6}$$

where ω_d is the electrical excitation frequency and $V_{p,dc}$ and $V_{p,ac}$ are the effective DC and AC parametric drive voltages. Squaring both the left-hand-side and right-hand-side of (1.6) yields

$$V^2(t) = V_{p,dc}^2 + 2V_{p,dc}V_{p,ac} \cos(\omega_d t) + V_{p,ac}^2 \cos^2(\omega_d t), \tag{1.7}$$

which can be rewritten as

$$V^2(t) \cong V_{\mathrm{dc}}^2 + V_{\mathrm{ac}}^2 \cos(\omega_{\mathrm{d}} t), \tag{1.8}$$

in the case of $V_{\mathrm{dc}}{}^2 \gg V_{\mathrm{ac}}{}^2$, where $V_{\mathrm{dc}} = V_{\mathrm{p,dc}}$, and $V_{\mathrm{ac}} = \sqrt{2 V_{\mathrm{p,dc}} V_{\mathrm{p,ac}}}$. These drive conditions provide a DC force term and an AC force term with one frequency ω_{d} [29] that decouples the parametric and direct harmonic excitation and adds independent control of V_{dc} and V_{ac}. If $V_{\mathrm{ac}}{}^2$ is close in value to $V_{\mathrm{dc}}{}^2$, higher-order frequency term $\left(V_{\mathrm{ac}}^2 / 2 V_{\mathrm{dc}} \right)^2 \cdot \cos^2(\omega_{\mathrm{d}} t)$ becomes significant that cannot be neglected.

As a comparison, using the same voltage in (1.8), for a class of parallel-moving interdigitated linear comb fingers (shown in Figure 1-3(a) whose movable comb moves in y, where the gap remains constant), the capacitance – displacement profile is linear along y. The electrostatic force is only a function of time and not of displacement:

Inter-digitated comb v.s. Non-inter-digitated comb

$$F_{\mathrm{p}} = \frac{1}{2} \frac{\mathrm{d}C}{\mathrm{d}y} V^2 = \frac{1}{2} \frac{\mathrm{d}C}{\mathrm{d}y} \left[V_{\mathrm{dc}}^2 + V_{\mathrm{ac}}^2 \cos(\omega_{\mathrm{d}} t) \right]. \tag{1.9}$$

where the derivative of capacitance $\dfrac{\mathrm{d}C}{\mathrm{d}y}$ is a constant because C is a linear function of y.

However, when driven by a parametric drive [for example, a non-interdigitated comb (Figure 1-3b) or a shaped-finger-comb (Figure 1-3c)], the force is both a function of time and displacement. For the special case of a linear parametric drive (*i.e.,* $\gamma_3 = 0$),

$$F_{\mathrm{p}} = -\gamma_1 \left[V_{\mathrm{dc}}^2 + V_{\mathrm{ac}}^2 \cos(\omega_{\mathrm{d}} t) \right] x. \tag{1.10}$$

This linear parametric force periodically modulates the total effective spring constant of the system, leading to linear parametric resonance effect.

Substituting (1.10) into (1.5) and neglecting the mechanical cubic nonlinearity, $k_3 x$, yields the

linear Mathieu equation

$$m\,\ddot{x} + b\,\dot{x} + \left(k_1 + \gamma_1 V_{dc}^2\right)x = -\gamma_1 V_{ac}^2 \cos(\omega_d t)x. \qquad (1.11)$$

The resonant frequency of the linear Mathieu equation, taking into account the linear

electrostatic spring effect, is

$$\omega_r = \sqrt{\frac{k_1 + \gamma_1 V_{dc}^2}{m}}. \qquad (1.12)$$

More generally, including the nonlinear term, γ_3 and k_3, yields the expanded nonlinear Mathieu

equation given in (1.3).

1.4.3. STEADY-STATE SOLUTIONS

In general, the perturbation methods linearize the equation about its equilibria and use an

asymptotic expansion to determine their stability. A nondimensionalization step is used to

rewrite the nonlinear Mathieu equation (1.3) into a general form so its solutions can be

universally applied in comparison of system behavior.

$$\ddot{s} + \varepsilon\,\mu\dot{s} + s(\delta + 2\varepsilon\cos 2T) + \varepsilon\,s^3(\delta_3 + r_3\cos 2T) = 0 \qquad (1.13)$$

The dimensionless displacement is

$$s = \frac{x}{x_0} \qquad (1.14)$$

where x_0 is the characteristic displacement. For example, x_0 may be the comb finger pitch (center-to-center distance between fingers in Figure 1-3b) for a non-interdigitated finger resonator, or the maximum stroke of a lateral comb resonator. The dimensionless time is

$$T = \frac{\omega_d t}{2}, \tag{1.15}$$

The dimensionless damping, μ, is

$$\mu = \frac{2b}{\varepsilon m \omega_d}. \tag{1.16a}$$

The dimensionless linear mechanical stiffness, δ, is

$$\delta = \frac{4(k_1 + \gamma_1 V_{dc}^2)}{m \omega_d^2}. \tag{1.16b}$$

The dimensionless parametric linear electromechanical stiffness, ε, is

$$\varepsilon = \frac{2\gamma_1 V_{ac}^2}{m \omega_d^2}. \tag{1.16c}$$

The dimensionless cubic mechanical stiffness, δ_3, is

$$\delta_3 = \frac{2(k_3 + \gamma_3 V_{dc}^2)x_0^2}{\gamma_1 V_{ac}^2}. \tag{1.16d}$$

The dimensionless parametric cubic electromechanical stiffness, r_3, is

$$r_3 = \frac{2\gamma_3 x_0^2}{\gamma_1}. \tag{1.16e}$$

The magnitude of these dimensionless parameters represents their relative importance.

To arrive at the steady-state solution, an assumed solution

Assumed
solutions

14

$$s(T) = A(T)\cos[\Omega T + B(T)],$$
(1.17)

and its time derivative

$$\dot{s}(T) = -A(T)\Omega\sin[\Omega T + B(T)],$$
(1.18)

are imposed to rewrite the normalized Mathieu equation into a state-space model in the amplitude, A, and phase, B, domain. The dimensionless mechanical frequency is

$$\Omega \overset{\Delta}{=} \frac{\omega_d}{2\omega_r}.$$
(1.19)

The method of averaging yields normalized steady-state amplitude by discarding fast-varying Averaged equations transients. The averaged equations are in the form of first derivative of amplitude and phase:

$$\dot{A} = \frac{1}{8}x_0\,\varepsilon A\Big[-4\mu + \big(4 + r_3 A^2\big)\sin(2B)\Big].$$
(1.20)

$$\dot{B} = \frac{1}{8}\varepsilon\Big[3A^2\delta_3 - 8\omega_1 + \big(4 + 2r_3 A^2\big)\cos(2B)\Big].$$
(1.21)

where a detuning parameter, ω_1, is defined as

$$\Omega = 1 + \varepsilon\omega_1.$$
(1.22)

The quantity $\varepsilon\omega_1$ measures the closeness of excitation frequency, ω_d, to the principal parametric resonance frequency (equal to twice the resonance frequency, $2\omega_r$). The averaged model is then used to determine the steady-state response and stability as in [17] and [18].

The dimensional steady-state amplitude, α_i, and phase solutions, β_i, are considered constants Steady-state solutions with respect to time. In the case when the effect of the air damping can be neglected, one steady-state stable trivial (zero) and three steady-state non-trivial responses [17] are derived by setting $\dot{A} = 0$ and $\dot{B} = 0$.

$\alpha_1 = \pm 2x_0 \sqrt{\dfrac{1+2\omega_1}{3\delta_3 - 2r_3}}$;	(1.23a)	$\beta_1 = \pm\pi\left(n+\dfrac{1}{2}\right)$, where $n = 0, 1, 2, \ldots$;	(1.23b)
$\alpha_2 = \pm 2x_0 \sqrt{\dfrac{-1+2\omega_1}{3\delta_3 + 2r_3}}$;	(1.23c)	$\beta_2 = \pm n\pi$, where $n = 0, 1, 2, \ldots$;	(1.23d)
$\alpha_3 = \pm x_0 \sqrt{-\dfrac{4}{r_3}}$;	(1.23e)	$\beta_3 = \pm\dfrac{1}{2}\arccos\left(-\dfrac{3\delta_3}{r_3} - 2\omega_1\right)$;	(1.23f)
$\alpha_4 = 0$;	(1.23g)	$\beta_4 = \pm\dfrac{1}{2}\arccos(2\omega_1)$,	(1.23h)

The resulting four dimensional steady-state solutions are $[\alpha_i\ \beta_i]^T$, where $i = 1, 2, 3$, and 4.

1.4.4. FREQUENCY RESPONSE

This section describes the denormalized transition frequency and its dependence on the observable system parameters such as the excitation voltages and frequency. With the parametric amplification occurring at excitation frequency, $\omega_d \cong 2\omega_r$, the dimensional mechanical response is

$$x(t) = \alpha_i \cos\left[\left(1 + \varepsilon\omega_1\right)\omega_r t + \beta_i(t)\right].$$ (1.24)

The stability of the steady-state amplitude and phase in (1.23) was extensively studied in [29] and [31]. A special case of the generalized stability analysis is included in Appendix A.4 to derive the "boundaries" between the stable and unstable solution branches. The stability analysis determines the bifurcation frequencies where bi-stable jumps occur. These transition frequencies are defined in (A.48).

Mechanical frequency response

Stability of solutions

Using an experimental non-interdigitated finger (NIF) parametric resonator described in Graphical representation

Chapter 2 as an example, four denormalized steady-state mechanical response amplitudes α_i and

the corresponding denormalized transition excitation frequencies $f_{tran} = f_{ij} = 2f_r\left(1 + \varepsilon\omega_{1,ij}\right)$ are

plotted in Figure 1-4, where i denotes the ith steady-state solution, and j denotes the jth bifurcation

frequency. The design variables are from Table 2-1 and Table 2-2 in Chapter 2 and the

dimensional bifurcation frequency values are summarized in Table 1-1. The driving voltages are

$V_{dc} = 40$ V and $V_{ac} = 20$ V.

Table 1-1: The dimensional bifurcation frequencies of the NIF resonator

Symbol	Physical interpretation	Value (kHz)
f_{11}	pitchfork bifurcation from trivial solution to the unstable region of α_1	29.2
f_{12}	saddle-node bifurcation of α_1 to α_3	25.0
f_{21}	pitchfork bifurcation where α_2 annihilates into the trivial solution	30.0
f_{22}	saddle-node bifurcation of α_2 to α_3	24.2

The frequencies f_{11} and f_{21} are called "pitchfork" bifurcation frequencies and f_{12} and f_{22}

are called the "saddle-node" bifurcation frequencies. At parametric resonance, two "pitchfork"

bifurcation frequencies spread out symmetrically corresponding to $\omega_{1,i1} = \pm 0.5$, where $i = 1,2$ on

the frequency axis.
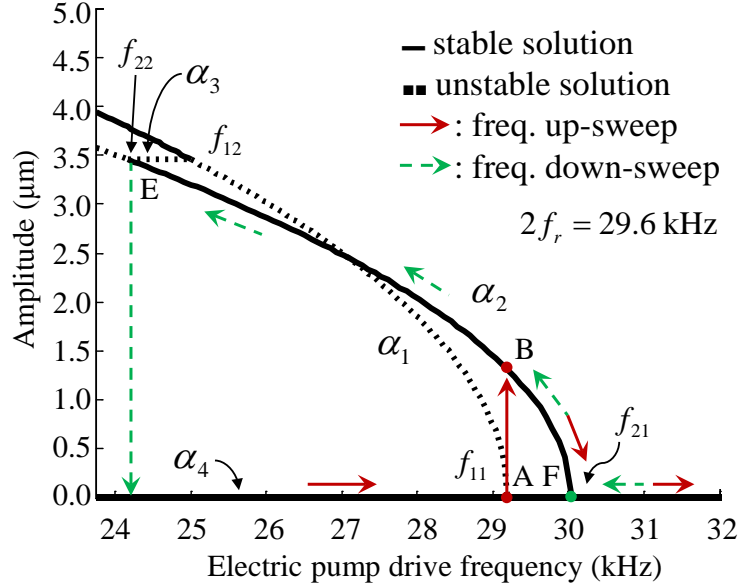
Figure 1-4: Measured steady-state response of a MEMS nonlinear resonator driven by the aligned NIF showing softening nonlinearity.

The non-zero stable solutions emanating from the bifurcation points f_{11} and f_{21} in Figure 1-4 emerge when the amplitude solutions are real-valued. Specifically for the amplitude solutions in (1.23), because $3\delta_3 \pm 2r_3 < 0$, the solution α_1 becomes real-valued when $\omega_1 < -\frac{1}{2}$. Similarly, the solution α_2 is real-valued when $\omega_1 < \frac{1}{2}$. The direction of the bending is determined by the sign of the combined nonlinearity $(3\delta_3 \pm 2r_3)$ in (1.23). For this particular aligned NIF resonator example, $3\delta_3 \pm 2r_3 < 0$, the amplitude-frequency solutions bend to the left, indicative of a "cubic softening" nonlinearity. The linear electrostatic stiffness, γ_1, changes the normalized parameter ε, which affects the resonance frequency and frequency scaling but not the bending behavior. The resonant amplitude is limited by the cubic stiffness nonlinearity. The

resonator maintains resonating state along the non-zero solution curves. The type of nonlinearity can vary from spring softening as reported in [16] and [17], to mixed nonlinearity and further to spring hardening with different NIF placement.

The steady-state response amplitude and phase versus the frequency (known as the frequency response) are experimentally validated by chirping the frequency slowly and recording the steady-state displacement by a lock-in amplifier or an optical vibration testbed. Details of experimental validation are described in Section 2.3 and 3.4.

1.4.5. HYSTERESIS AND BIFURCATION BEHAVIOR

The "bending" of the curve results in multi-valued solutions at the same excitation frequency to the left of pitchfork bifurcation point f_{21}. Depending on the initial condition, the response amplitude will land on one of the two solution branches. When the frequency is swept from low to high values (frequency up-sweep), the system amplitude first follows the trivial (zero) solution with a very small motion in x created by the thermomechanical noise, until it reaches the bifurcation frequency f_{11} of solution α_1 where the parametric stable trivial solution intersects with the parametric unstable region of α_1 (point A). At point A, solution α_1 is unstable while α_2 is stable. With the presence of a small motion perturbed from the zero displacement by the Brownian noise force, the system jumps from the zero solution to the stable region of α_2 (red line from A to B) as soon as its trajectory passes through bifurcation frequency f_{11}. The jump amplitude a_{tran} is defined as the amplitude difference between B and A. At the "pitchfork"

bifurcation A, $\omega_{1,11} = -0.5$, the denormalized up-sweep transition frequency and the jump amplitude are

$$f_{11} = 2f_r \left(1 + \varepsilon\omega_{1,11}\right) \cong 2f_{r0}\sqrt{1 + \frac{\gamma_1 V_{dc}^2}{k_1}\left(1 - \frac{\gamma_1 V_{ac}^2}{4k_1}\right)} \tag{1.25}$$

$$a_{tran} = a_2\big|_{f=f_{11}} = 2\sqrt{\frac{\gamma_1 V_{ac}^2}{-\left(3k_3 + 3\gamma_3 V_{dc}^2 + 2\gamma_3 V_{ac}^2\right)}} \tag{1.26}$$

where $f_{r0} = (1/2\pi)\sqrt{k_1/m}$ is the natural frequency and the rest of the terms are independent of mass m. Using the design parameters in Table 2-1 in Chapter 2, the perturbation parameter $\varepsilon = 0.028$ yields a very small perturbed term $\varepsilon\omega_{1,11} = -0.014$. The up-transition frequency, though perturbed, is very close to twice the resonance frequency, which provides guidance to the search of the bifurcation setpoints. Equation (1.25) also indicates that V_{dc} provides an electrostatic tuning effect that shifts the location of the bifurcation. V_{ac} affects the location of the bifurcation and the width of the non-zero solution region for non-zero V_{dc}. In the case of extremely small V_{ac}, both the non-zero solution branches, namely α_1 and α_2, converge, making it difficult to search for the bifurcation because of the very small jump step. With a large enough DC polarization voltage V_{dc}, (1.25) is approximately a linear function of V_{dc}, which is later verified by behavioral modeling results in Chapter 2.

When frequency is swept from high to low values (frequency down-sweep), the system Frequency decreasing sweep amplitude first follows the stable solution branch of α_2 until it reaches the saddle-node bifurcation point E where a stable solution turns into a saddle point. The amplitude step jumps

from the edge of α_2 to the trivial solution α_4. The corresponding saddle-node bifurcation

frequency at E is $\omega_{1,22} = -0.5 - \dfrac{3\delta_3}{2r_3}$, giving a denormalized down-sweep transition frequency

$$f_{22} = 2f_{r0}\sqrt{1 + \frac{\gamma_1 V_{dc}^2}{k_1}}\left[1 - \frac{\gamma_1 V_{ac}^2}{4k_1} - \frac{3(k_3 + \gamma_3 V_{dc}^2)\gamma_1}{4k_1\gamma_3}\right]. \tag{1.27}$$

All the terms in the expression except the natural frequency, f_{r0}, are independent of mass.

1.5. BIFURCATION-BASED CONTROL

To explore the capability of parametric resonance in making an ultrasensitive mass sensor or Open-loop method

a sensitive strain gauge, a drive scheme is needed to excite the parametric resonance and reveal

the bifurcation behavior. An open-loop frequency sweep had been extensively used by Turner,

et al. [1], [13] to measure the change in the bifurcation frequency point. This change had been

exploited to establish a link between the bifurcation frequency and the mass [1] or chemical

absorption [2]. However, the open-loop method is slow due to a long transient frequency chirp

tests (on the order of minutes) that exploits quasistatic operation points. This drawback makes

the open-loop sweep method impractical for sensor applications.

An operation point servo at or near the bifurcation setpoint can be designed to facilitate the Challenges

control right at the "jump" event. However, the nonlinear parametric resonance system exhibits

latch-up instability in the quasistatic operation. This instability is due to the slow-time scale that

is required to collapse from a zero state and move along the bifurcation manifold [14] to a non-

zero state. Due to salient nonlinearity, such a system also has hysteretic behavior, which limits

21

the range of the servo operation. Moreover, these underdamped systems have relatively long ring-down and build-up time. The latch-up instability, hysteresis, and long resettling time render classical linear control possibilities ineffective.

Different approaches exist for the closed-loop control at the bifurcation point. Both Closed-loop amplitude- and phase-based bifurcation analog controllers were previously implemented. methods Burgner *et al.* implemented a bifurcation-based analog control scheme [4] by observing the coherency of the signal phase. The controller is designed such that the resonant amplitude is kept very small (140 pm) in order to lock into the phase coherency to avoid the slow-time bifurcation jump event that is required to travel from the zero state to the non-zero state. The separation of the time scales is accomplished by adjusting the pump drive voltage to maintain a near-zero state. The controller is impractical for on-chip integration, at least in current technology, since it is implemented in a field-programmable gate array and takes as the input the statistics of the phase. The loop relies on a small stroke to avoid the jump and the long reset time that follows, leading to low ratio of steady-state amplitude to the system noise. A year later, Burgner *et al.* reported an improved controller with vibration amplitude as the controlled variable [26]. The technique settles at relatively small amplitude of below 1.5 nm, making it unsuitable for robust control applications.

Chapter 4 proposes a bi-state parametric controller that utilizes both "on" and "off" drive- Parametric amplitude states to avoid the latch-up instabilities and address the issue of limit cycle and controller instability. The servo controls the system at a bifurcation frequency setpoint with relatively high drive amplitude (on the order of 1.9 μm). The control plant is a large-stroke shaped-finger comb

parametric resonator [25] made in a silicon-on-insulator-MEMS (SOI–MEMS) process. An electrostatic comb comprising a set of interdigitated "quadratic-shaped-finger" is the parametric drive.

Chapter 5 presents details on a bi-state controller for the control of a Duffing microresonator on the falling edge of the instability [34]. The Duffing servo point was chosen at the maximum "on" amplitude prior to the bifurcation jump event.

Duffing controller

1.6. THESIS CONTRIBUTIONS

This work demonstrates a novel drive-amplitude state control technique capable of servoing along the microelectromechanical parametric resonant bifurcation jump point. The controller is capable of large amplitude operation, which enhances its robustness in the presence of detection noise. The servo states are cycled by a fast pulse width modulation that circumvents the latch-up or latch-off instability and slow amplitude build-up or ring-down as would happen in quasistatic operation with analog feedback. The controller is experimentally validated to achieve sensitive detection of bifurcation frequency curve shifts down to millihertz range. The predicted equivalent minimum detectable mass change is 12 pg if the controller were to form the core of a future mass sensor. The controller plant is driven by a high-stroke parametric-mode electromechanical drive with 8 μm amplitude and 17% large frequency tuning range. This "shaped-finger" comb drive topology is achievable by tailoring the finger shape of a laterally-moving comb. The high-stroke shaped-finger drive enhances the ratio of steady-state amplitude to the minimum Allan deviation beyond 120 dB.

Contribu-
tions

The primary contributions of this work are:

- The first experimental validation of large-stroke parametric resonance driven by a laterally-moving "shaped-finger" comb topology with differential capacitive transducer readout. Two embodiments of "quadratic-shaped-finger" comb parametric resonators are successfully fabricated to accommodate up to 8 μm bifurcation jump. Frequency domain and time domain bifurcation response are characterized. Experimentation matches the analytic model within 2%.

- Design and analysis of the finger profile of the "shaped-finger" comb to customize the linear and cubic electrostatic spring stiffness coefficients. The effective electrostatic spring constant in combination with system mechanical nonlinearities generate a large-displacement parametric response. Both the design space and the tuning dynamics of the "quadratic-shaped-finger" comb are discussed.

- Invention and successful implementation of a DC drive-amplitude state closed-loop bifurcation-point parametric controller to control on the bifurcation edge with a large drive amplitude while avoiding latch-up instabilities. The controller uses the "quadratic-shaped-finger" comb resonator as the control plant and off-chip electronics as the feedback controller. An exemplary system is demonstrated at 1.9 μm amplitude with 4.5 Å resolution in a 0.2 Hz bandwidth and a predicted equivalent mass sensitivity of 12 pg.

- Implementation of an AC drive-amplitude state closed-loop bifurcation-point controller to control a crab-leg Duffing resonator on the falling edge of the instability.

- Behavioral simulation of MEMS parametric resonance that provides insights into the response of the nonlinear system and its dependence on system parameters. In this work, behavioral models are built with mechanical primitives from a hierarchical MEMS circuit library to simulate and explore the controller topology and optimize control loop parameters.

Other supporting work includes:

Other contributions

- Design and characterization of a CMOS-MEMS version of a non-interdigitated finger resonator that validates the general parametric resonance theory and its behavioral simulation model.

- Design and characterization of a prototype CMOS-MEMS tangential drive "T-drive" resonator demonstrating large-stroke parametric response.

- Developed 2-DoF twisting-type electrothermal actuator for scanning laser rangefinder application by independently actuating two parallel metal-polysilicon-oxide CMOS-MEMS vertical electrothermal actuators.

- Co-developed an in-house silicon-on-insulator (SOI)-MEMS fabrication process to promote electromechanical ideations such as the shaped-finger comb parametric drives and mode-matched gyroscopes.

- Designed integrated stress and temperature sensors for investigating the interaction effects of temperature and packaged stress gradients on the mode-matched gyroscopes. Developed stress sensing techniques and prototyping boards. Mapped stress gradient by piezoresistive inversion layer transducers.

1.7.   THESIS OUTLINE

The thesis is organized as follows. Chapter 1 starts with general descriptions of parametric Outline
resonance, its benefits, and excitation methods. It then introduces the perturbation analysis and
the steady-state solutions of the governing nonlinear Mathieu equation, its frequency response
and the associated bifurcation diagram. Detailed mathematical treatments to the nonlinear
Mathieu equation, including nondimensionalization, method of averaging, and the stability
analysis, are described in rich detail in Appendix A. Circuit-level interoperable behavioral
modeling for accurate predictive designs is presented in Chapter 2 using a CMOS-MEMS non-
intedigitated comb finger resonator as a modeling example. Chapter 3 focuses on synthesizing a
class of high-stroke parametric-mode electromechanical drives, together with experimental
verification of a quadratic-shaped-finger comb parametric resonator. Experimentation regarding
the frequency domain and time domain responses is presented. Chapter 4 and Chapter 5 discuss
technical challenges in building a feedback servo on the edge of the bifurcation jump point, and
presents amplitude-state bifurcation controllers that successfully servo along the pitch-fork
bifurcation manifold of a parametric resonator in Chapter 4 and on the falling edge of a Duffing
resonance in Chapter 5. Chapter 6 concludes the thesis and suggests possibilities for future
work.

(end)

CHAPTER 2   CMOS-MEMS NON-INTERDIGITATED

COMB FINGER PARAMETRIC RESONATOR

P arametric resonance in electrostatically actuated MEMS gives rise to complex nonlinear phenomena. The need for accurate predictive design of nonlinear systems featuring parametric resonance provides motivation to refine mixed MEMS/analog behavioral composable modeling and simulation methodologies. As a first step toward validating these methodologies, a parameterized schematic of a canonical parametric resonator testbed is built with primitive beam, plate and gap models from a MEMS Verilog-A library [32] and with a macro model of the nonlinear drive with coefficients extracted from a finite element simulation [16]. The behavioral models are coded in Verilog-A and the composable MEMS schematic [17] is simulated in Cadence Spectre. For an example micromechanical non-interdigitated comb parametric resonator, the behavioral modeling and the analytic perturbation solutions are validated by optical vibration measurements matching to 0.6% and 2.1%, respectively. The simulation schematics and modeling methodology were reported in [16], [17], and [40]. Full description of this methodology using circuit-level interoperable behavioral modeling for accurate predictive designs is presented in this chapter, where a CMOS-MEMS non-interdigitated comb finger resonator is used as a modeling example.

This work presents details on system-level modeling of the example non-interdigitated comb resonator and its transient chirp frequency response [16], and elaborates on the schematic-based

composable modeling methodology. To investigate the dynamics on the edge of the instability, the transient behavior at the bifurcation jump and the step turn-on transient of the parametric drive are presented. The effects of damping and parametric voltage amplitude on the bifurcation frequency and amplitude are characterized. A testbed using video microscopy is used to validate the analytical solution of the transition frequency and its jump amplitude along with the behavioral modeling simulation results. Using the validated behavioral simulation, the variation in the jump behavior is quantified by statistical analysis considering the process variation and mismatch in the beam width, thickness, Young's modulus, and density.

2.1. NON-INTERDIGITATED COMB FINGER RESONATOR EXAMPLE

Shown in Figure 2-1 is an SEM image of the fabricated CMOS-MEMS nonlinear plate-mass Device resonator as a first exploration of parametric resonance. The resonator is characterized in air to accommodate the optical-based measurement. Four serpentine springs exhibiting a small cubic stiffening nonlinearity suspend the 224 μm by 264 μm perforated plate mass of 461 ng. The curl-match frame allows the stator and rotor fingers to align evenly in the presence of the vertical residual stress gradient in the released CMOS metal-oxide stack. The curl-matched structure is borrowed from a prior CMOS-MEMS accelerometer design [42]. Electrostatic force from the aligned non-interdigitated comb fingers (NIF), modulated by the parametric drive voltage amplitude, excites the resonator. The NIF design makes use of the symmetric fringing field between non-interlocking comb fingers to generate a cubic force–displacement relationship adopted from [1], [18], [43], and [44]. Four sets of parallel-plate interdigitated comb fingers (IF)

are included in the design to directly excite natural resonance to measure the system's resonant frequency ω_r during a separate test state. In the designed resonator, mechanical limit stop fingers are used to limit the displacement of the motion to protect against electrical short circuit. These fingers constrain the x-directed motion of the resonator to the range of $-1.6\ \mu m < x < 1.6\ \mu m$. The design parameters are summarized in Table 2-1. The nonlinear stiffness k_3 is obtained by fitting the force-displacement curve to a 3rd order polynomial $F_k = k_3 x^3 + k_1 x$.
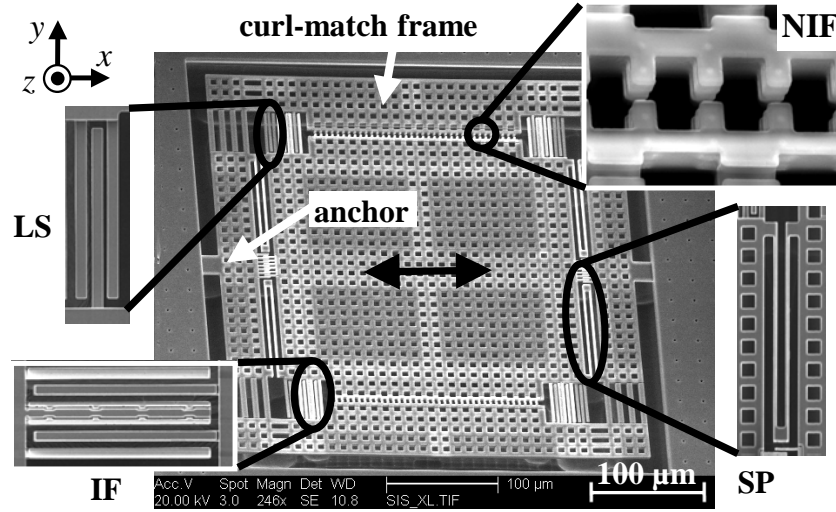
Figure 2-1: SEM of a CMOS-MEMS nonlinear parametric resonator that moves in x, with zoom-in view of non-interdigitated comb fingers (NIF), interdigitated comb fingers (IF), serpentine spring (SP), and mechanical limit stop fingers (LS).

From symmetry, the non-interlocking fingers exert zero net force when aligned directly or when evenly staggered. Near equilibrium, the electrostatic force can exhibit either a hardening or softening nonlinearity as depicted in Figure 2-2. This chapter uses an aligned finger setup providing a cubic electrostatic hardening nonlinearity.

Finger alignment
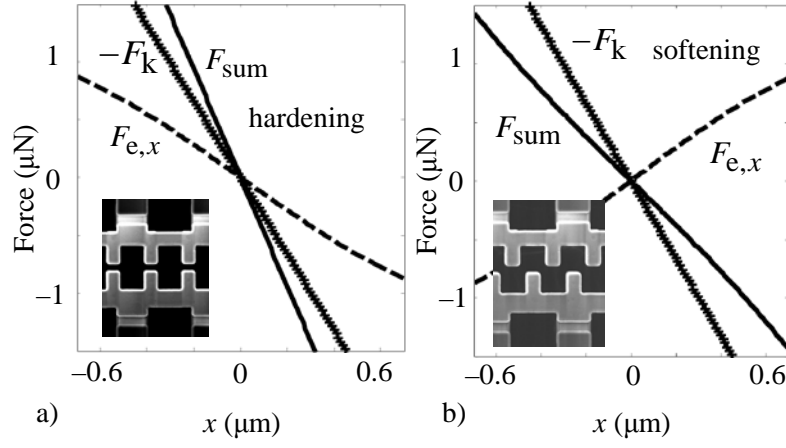
Figure 2-2: Steady-state force-displacement relationships of a) aligned fingers exhibiting electrostatic hardening nonlinearity, b) evenly staggered fingers showing electrostatic softening nonlinearity.

Table 2-1: Design parameters of the NIF resonator

Symbol	Dimensional parameter	Value
x_0	NIF x-directed spatial period	5.00 μm
l_{NIF}	NIF length	2.55 μm
w_{NIF}	NIF width	1.84 μm
g_{NIF}	NIF y-directed gap	0.81 μm
t_{NIF}	NIF equivalent thickness	5.40 μm
γ_1	NIF linear electrostatic stiffness	6.1×10^{-4} N/m/V^2
γ_3	NIF cubic electrostatic stiffness	-1.0×10^8 N/m^3/V^2
w_f	flexure width	1.41 μm
l_f	flexure length	83.10 μm
t_{Al}	flexure Al total thickness	2.90 μm
t_{ox}	flexure oxide total thickness	1.90 μm
k_1	flexure linear spring constant (4 sets)	3.3 N/m
k_3	flexure cubic spring constant (4 sets)	4.8×10^6 N/m^3
b	damping coefficient	141×10^{-9} nkg/s
f_r	plate-mass resonator resonant frequency	14 kHz

Analytical solutions to the governing Mathieu equation are introduced in Chapter 1 and Analytic frequency response

Appendix A. For the NIF resonator, Table 2-2 summarizes the dimensionless parameters with ___response___

values when V_{ac} = 20 V and V_{dc} = 40 V. The dimensionless parameters are used in the analysis

of the steady-state responses and their stability.   The steady-state frequency response is

graphically shown in Figure 1-4 with ensuing discussion on the instability and the hysteretic

operation. This chapter focuses on the behavioral modeling of this class of nonlinear resonator

and the simulation of the bifurcation behavior as well as the step turn-on dynamics.

Table 2-2: The normalized dimensionless parameters of the NIF resonator

Symbol	Dimensionless parameter	Value (unitless)
δ	linear mechanical stiffness	~1
ε	parametric linear electromechanical stiffness	0.028
δ_3	cubic mechanical stiffness	–33.465
r_3	parametric cubic electromechanical stiffness	–8.367
μ	damping	0.1084

2.2. SYSTEM SIMULATION METHODOLOGY

Replacing a rather complex nonlinear coupled-domain electromechanical system with its Motivation

equivalent behavioral model not only aids in model-order reduction but also incorporates

secondary effects that would not be accounted for in an analytic analysis. The inadequacy of

analytical perturbation methods in simultaneously dealing with damping and nonlinearities,

together with the constraint of the nonlinear Mathieu equation in handling only x and x^3

nonlinearities, motivates the use of behavioral modeling and simulation of the complete system.

A conceptual schematic of the parametric resonator is built in Figure 2-3. The beam, plate, and gap models composing the resonator are the primitives from an interoperable MEMS behavioral model library – NODAS, implemented in the Verilog-A analog hardware description language [32]. In NODAS, the MEMS translational discipline is defined such that the Kirchhoffian through variable, force, is analogous to electrical current; and the across variable, displacement, is analogous to electrical voltage. The mass, damping, and spring forces are lumped to the mechanical ports of the models. Primitives from this library are used to form mechanical subsystems, such as a mass-spring-damper subsystem. These subsystems are combined with electrical subsystems, *i.e.*, voltage source and low-pass-filter module, to form functional electromechanical systems.
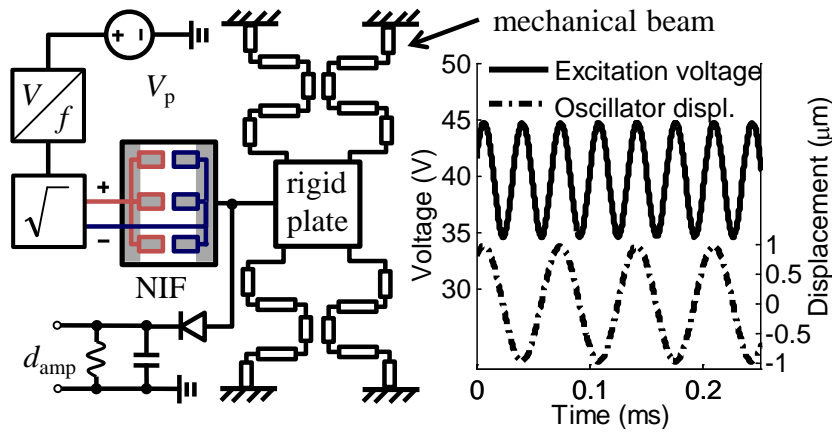
Figure 2-3: Conceptual MEMS schematic of the nonlinear parametric resonator, together with the excitation and oscillation waveforms at the parametric resonance. The piecewise linear voltage source V_p controls the output frequency of the V/f model to perform transient chirp simulation.

2.2.1. NONLINEAR ELECTROSTATIC FORCE MODEL

The non-interdigitated comb actuators were first introduced by Adams et al. [43]. By <u>NIF history and modeling</u> adjusting the softening and stiffening comb ratio, the total linear and cubic stiffness can be tuned independently so the parametric frequency response can be adjusted. The nonlinearity of the NIF was treated in [44] by a polynomial fit localized to the augmentation (stiffening) and reduction (softening) regions with vibration amplitude below half of the comb finger pitch. General behavioral modeling and simulation of the NIF, however, requires modeling of the NIF beyond ±½ of the comb pitch to include the periodicity of the NIF comb and for the NODAS simulation to converge to a self-consistent solution. The force-displacement curve is fit numerically to a spatial Fourier series to be capable of simulating displacement stroke beyond one pitch of the NIF comb. Although the validation experiments in section 2.3 are limited to within one comb pitch, the development of the behavioral nonlinear actuator model can be used towards exploring parametric excitation of high stroke [25] and is an augmentation to the well-established small-stroke NIF model.

Finite element methods provide the energy–displacement relationship [17]. The NIF comb is <u>FEM simulation of the NIF</u> fabricated in a CMOS-MEMS process [36] that results in comb fingers composed of three stacked CMOS aluminum layers with interposing oxide. The modeling of the NIF combines the results of two planar finite-element analysis (FEA) simulations: a plan view FEA to compute fringe fields in plane (x and y directed) and a cross-section FEA to compute fileds out of plane (z directed). The simulated electric energy density–displacement behavior spanning five finger periods is shown in Figure 2-4.
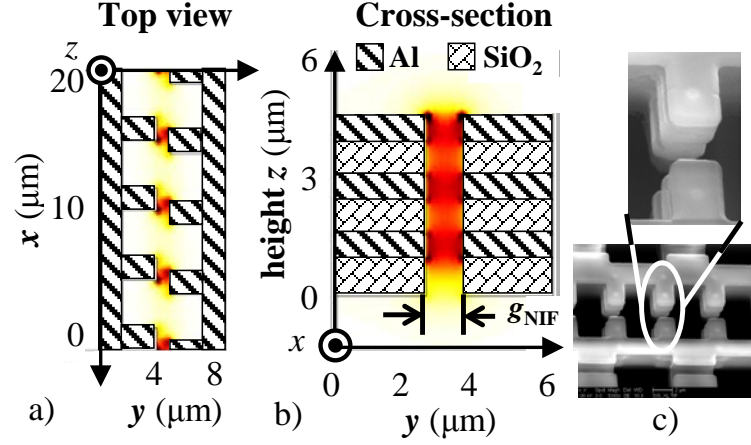
Figure 2-4: a) The top view of the electric energy density distribution for 1 μm x-displacement over a region of five finger periods. b) The cross-section spanning the comb fingers overlaid with the electric energy density distribution. c) An SEM of the sidewall profile of the fabricated NIF.

As shown in Figure 2-5, the nonlinear force by the NIF is realized by moving one set of $\overline{\text{Periodicity of } C \text{ and } F}$ fingers perpendicular to the direction of the electric field in such a way that the change in electric energy density W_e including fringe field effects gives rise to a periodic electrostatic force F_e acting along the direction of motion. The resonator is then assumed to operate in a small displacement around a setpoint that forms a null in the force. This small displacement stroke is limited roughly to a quarter of the finger pitch (5.0 μm) for the required nonlinearity. Under this stroke, the electrostatic force can be approximated as a 3rd order polynomial in x in the perturbation analysis. In the behavioral simulation, however, a spatial Fourier series is applied to capture not only the electrostatic spring constants for small displacement but also the periodic variation of the capacitance and the force.

34
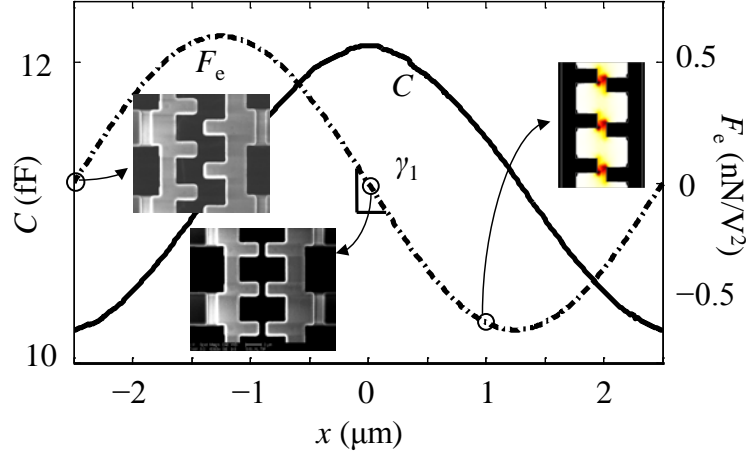
Figure 2-5: Periodicity of capacitance C and x-directed electrostatic force F_e with respect to the x-displacement for y-directed gap of 1 μm. The callouts are the relative positions of the non-interdigitated comb fingers.

Modeling the capacitance C as the energy storage element for an applied voltage of 1 V,

Analytic model

$$C = 2\int_A t\, W_{e,\text{plan}}\left(x, y\right) \mathrm{d}x\mathrm{d}y ,\qquad (2.1)$$

where $W_{e,\ \text{plan}}(x,\ y)$ is provided by the 2D x-y plan-view FEA (Figure 2-4a). The equivalent parallel-plate finger thickness is

$$t = 2g_{\text{NIF}}W_{e,\text{cs}}\big/\varepsilon_0 ,\qquad (2.2)$$

where $W_{e,\ \text{cs}}$ is determined from the 2D z-y cross-section FEA [17], as described in Figure 2-4b. The equivalent thickness value is 5.4 μm for fingers made from the three metal-oxide stack in the CMOS-MEMS process. The surface integration is carried out through the total air area surrounding the NIF. In the behavioral NIF model, the capacitance

35

$$C(x) = a_0 + \sum_{i=1}^{8} a_i \cos\left(i\frac{2\pi}{\tilde{x}_0}x\right), \tag{2.3}$$

and the electrostatic force

$$F_e(x) = -\frac{\pi V^2}{\tilde{x}_0} \sum_{n=1}^{8} n a_n \sin\left(n\frac{2\pi}{\tilde{x}_0}x\right) \tag{2.4}$$

are modeled as spatial Fourier series. Coefficients for eight spatial harmonics a_n are fit to the capacitance–displacement plot in Figure 2-5. The flexure, the NIF electrode dimensions and the gap are measured using SEM images and calibrated against the pitch of the etch holes on the plate mass.

2.2.2. TRANSIENT CHIRP SIMULATION

A transient chirp simulation using Cadence Spectre is used to sweep the excitation frequency Drive voltage to yield the frequency response relationship. The simulation uses the design values specified in Table 2-1. The behavioral modeling preserves the same form of voltage excitation as that of the perturbation analysis in (1.8). A piecewise-linear voltage source supplies a time-varying control voltage $v_{in}(\tau)$ to the voltage-controlled oscillator (VCO) model whose output is $v_{out}(t)$, so that

$$v_{out}^2(t) = V_{dc}^2 + V_{ac}^2 \cos\left[2\pi\int_0^t \left[Kv_{in}(\tau) + f_0\right]d\tau - 2\pi k(t) + \varphi_{ini}\right], \tag{2.5}$$

where K (Hz/V) is the frequency gain, f_0 is the center frequency, t is the "fast" varying time, which is on the order of the reciprocal of the resonant frequency, and τ is the "slow" varying time, which is related to the time rate change of the control voltage and is usually 3 to 4 orders of magnitude longer than t. φ_{ini} represents the initial phase, and $k(t)$ is an integer chosen such that

the phase $\varphi(t) \in \left[-\pi, \pi \right]$. The control voltage $v_{in}(\tau)$ is chosen such that the output frequency is swept through the principal parametric resonance condition ($2\omega_r$). The amplitude of the response is extracted in schematic simulation by passing the displacement signal through an envelope detector.

Transient chirp frequency response of the parametric mode is shown in Figure 2-6 with the Chirp simulation zoom-in view of the transient exponential growth on the edge of the bifurcation point. The 3 s results transient chirp simulation ramps frequency from 27 kHz to 32 kHz and reveals a "pitchfork" bifurcation emerging at 29.31 kHz. The simulation uses the same voltage values as those of Figure 1-4.
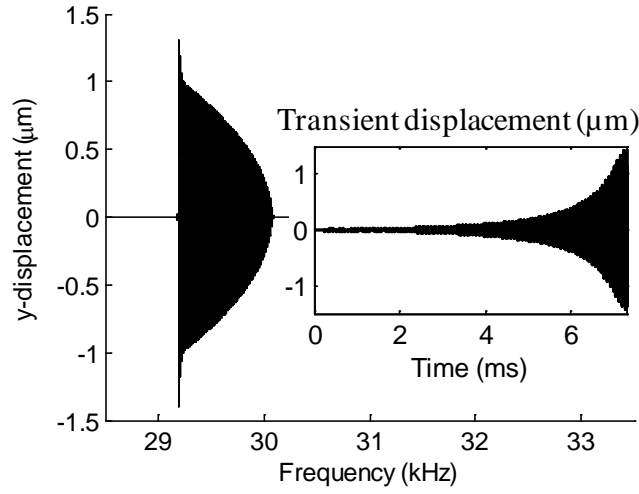
Figure 2-6: Transient chirp frequency response of the NIF plate-mass resonator in the parametric mode, together with the transient exponential growth on the edge of the bifurcation point.

The transition frequencies around the principal parametric resonance and the type of Discussion nonlinearity have a strong relation with finger placement, DC bias voltage, oscillating AC

magnitude, mass of the resonating plate, linear stiffness of the spring, and linear electrostatic stiffness coefficient of the NIF comb.
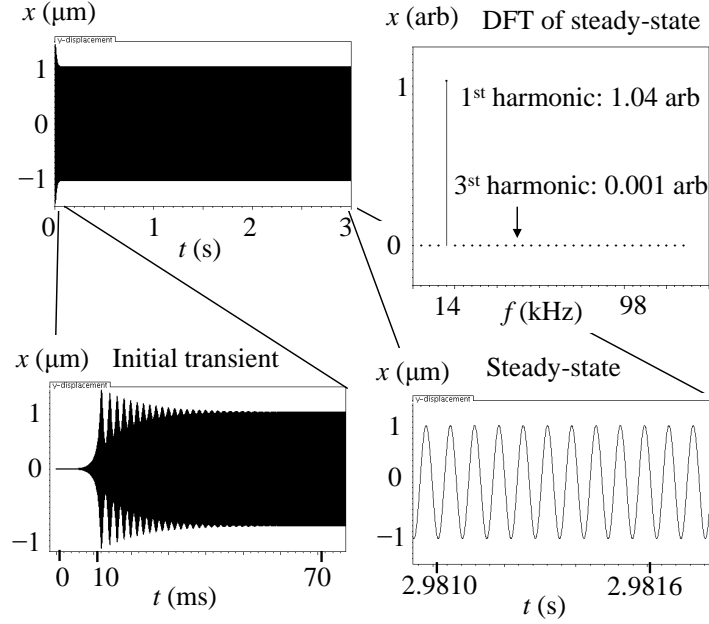
Figure 2-7: Transient for a step turn-on of the parametric drive, whose frequency is fixed at 29.5 kHz (within the non-trivial resonance region).

2.2.3. SYSTEM TRANSIENTS AND DAMPING

Turn-on transient is shown in Figure 2-7 for a step turn-on of the parametric drive voltage. Turn-on transient

The parametric drive frequency is fixed at 29.50 kHz, which is within the non-zero resonance region. The lower-left inset shows the initial exponential growth occurring at 6 ms. An amplitude-modulated transient follows immediately after the growth and dies out on the order of

38

Q/ω_r, where Q is the quality factor of 50. The steady-state oscillation is included in the lower-right inset. In the time range after the exponential growth settles, the system resonates at 14.75 kHz, as shown by the DFT of the steady-state waveform in the upper right inset. A similar turn-on transient experiment is found in [12].

For a fixed polarization voltage, V_{dc}, from (1.25), increasing the oscillating pump drive V_{ac} Effect of V_{ac} increases ε, and thus moves the up-transition setpoint to a lower frequency. This fact is verified by the behavioral modeling results in Figure 2-8; the transition frequency decreases by 9% as V_{ac} varies from 10 V to 50 V, whereas the jump amplitude increases, consistent with (1.25) and (1.26). This justifies the choice of V_{ac} in the experimental setup to be 20 V to excite approximately 1 µm amplitude motion while not risking using higher voltage that could result in an electric breakdown.
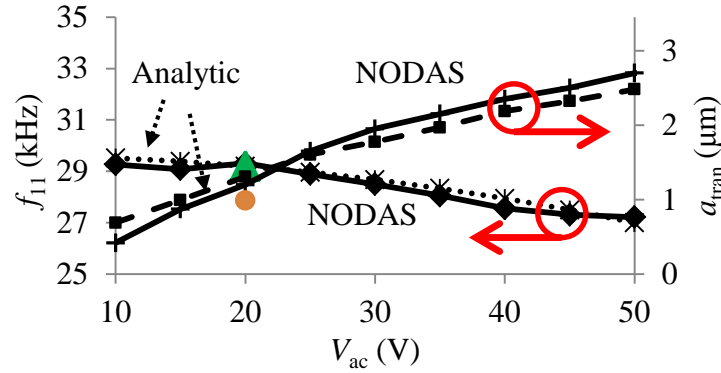
Figure 2-8: The up-sweep transition frequency f_{11} and the jump amplitude a_{tran} with varying AC oscillating amplitude V_{ac}, with V_{dc} fixed to 40 V. Also plotted are the experimentally measured transition frequency (triangle) and jump amplitude (circle).

Increasing the DC bias voltage V_{dc} shifts the principal bifurcation frequency to a higher value, because the NIF used is an electrostatic stiffening comb (*i.e.*, $\gamma_1 > 0$). Thus, the upper and lower bounds of the hysteresis effect shift to higher frequencies. The up-sweep transition frequency f_{11} and jump amplitude a_{tran} are plotted in Figure 2-9 with varying DC bias voltage V_{dc} and damping coefficient b. The up-sweep transition frequency varies in an approximately linear fashion with large DC actuation voltage, which also follows the analytic results in (1.25) [16].
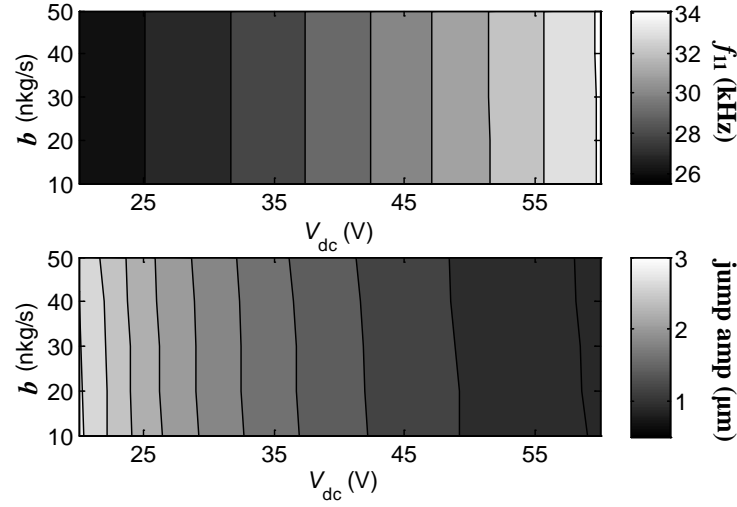
Figure 2-9: The up-sweep transition frequency (upper) increases while jump amplitude (lower) decreases with increasing DC bias voltage V_{dc}, with V_{ac} fixed to 20 V. The damping has little effect on the transition frequency and decreases the jump amplitude by 10 nm for each 10^{-8} kg·s^{-1} increase in damping coefficient.

2.3. DEVICE CHARACTERIZATION

2.3.1. VIBRATION MEASUREMENT TESTBED

A transition sweep measurement using video microscopy with stroboscopic illumination [37]   Testbed description

was set up to characterize the bi-directional transition frequencies and their jump amplitude. The

diagram of the measurement testbed built around the MIT Microvision optical vibration test

system [16] is shown in Figure 2-10. The testbed generates an oscillating voltage without an

offset that is fed into an off-chip frequency doubler circuit to yield the voltage in (1.6) [16]. The

validation experiments carried out using this optical vibration measurement setup operate under

atmospheric pressure.
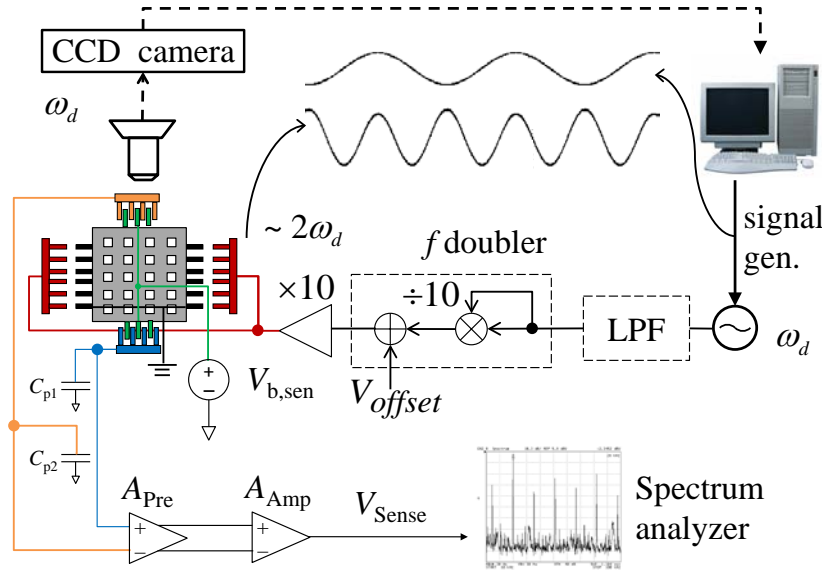
Figure 2-10: Testbed using video microscopy with stroboscopic illumination and an off-chip
frequency doubling circuit.

After a preliminary estimation of the stiffened resonance frequency given by (1.12), a sweep Frequency chirp sweep method

of electric excitation frequency around the predicted principal parametric resonance $f = 2f_r =$

29.6 kHz was performed until a "jump" in amplitude was observed and the corresponding

transition frequency was recorded. The measurement resolution was limited by the frequency

increment of the signal generator of the Microvision system. For the up-sweep and down-sweep

measurements, the frequency increments were 50 Hz and 100 Hz, allowing ±100 Hz and

±200 Hz resolution, respectively. All testing was performed in air and observed under 500X

magnification.

2.3.2. VIBRATION MEASUREMENT RESULTS

Characteristics of both parametric resonance excited by the non-interdigitated comb and the Harmonic and parametric responses

harmonic resonance excited by the interdigitated comb are plotted with respect to the mechanical

frequency in Figure 2-11. Both responses are plotted with respect to the mechanical frequency.

Harmonic response reveals a small spring softening effect. The parametric resonance gives rise

to a sharp resonant peak at the "jump" point, despite that the harmonic mode has only a quality

factor (Q) of 50 in air. The sharp transition in the parametric mode at relatively high damping

was demonstrated previously [8]. The sharpness of the transition boundary is independent of the

quality factor [33] which is inversely proportional to the system loss due to the air damping,

anchor loss, and thermoelastic damping.
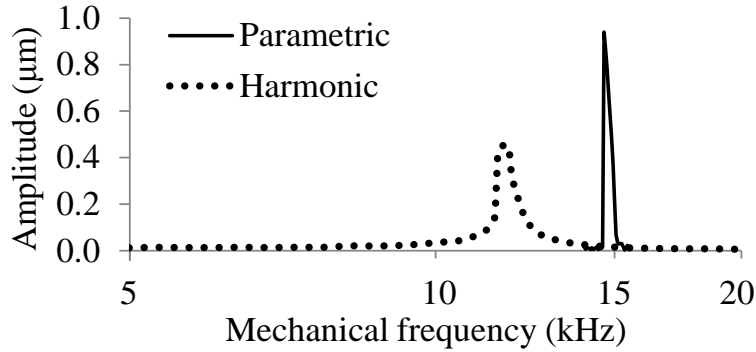
Figure 2-11: Experimental up-sweep frequency response of the harmonic mode excited by the interdigitated comb and the parametric mode excited by the non-interdigitated comb in air.

Figure 2-12 is an overlaid comparison of the analysis, behavioral model simulation and experimental results for both up-sweep and down-sweep tests. When performing a frequency down-sweep, the system amplitude first follows α_2 until the displacement is 1.6 μm when the mechanical limit stop fingers hit each other (point C), forcing the bi-stable system to degenerate to the trivial state of motion (dashed line from C to D), far before it reaches the "saddle-node" bifurcation at point E in Figure 1-4. The measured transition frequencies are compared with perturbation analysis and behavioral simulation in Table 2-3. As discussed in Chapter 1, the sharp transition property is applicable for many ultra-sensitive sensor applications such as mass flow rate sensors [2] and magnetometers [9], and is used in noise-squeezing applications for parametric amplification [8]. For both sweep directions, the behavioral model simulation matches within 0.2% and the analytical model matches within 2.1%. The down-sweep analytic model neglects the effects of damping and the limited displacement. These effects may give rise to the discrepancy between the measured and analytic results. The maximum achievable

Overlaid comparison of analysis, simulation, and test results

43

displacement is constrained by the limit stop fingers, thus leading to the measured result being at

a higher transition frequency than the predicted saddle-node bifurcation.

Table 2-3: Comparison of bi-directional bifurcation frequencies for the aligned NIF testbed

Transition frequency [kHz]	Analysis	NODAS	Measurement	Comparison vs measurement	
				Analysis	NODAS
Up-sweep	29.20	29.31	29.30	–0.34%	0.03%
Down-sweep	28.78	28.15	28.20	2.06%	–0.18%
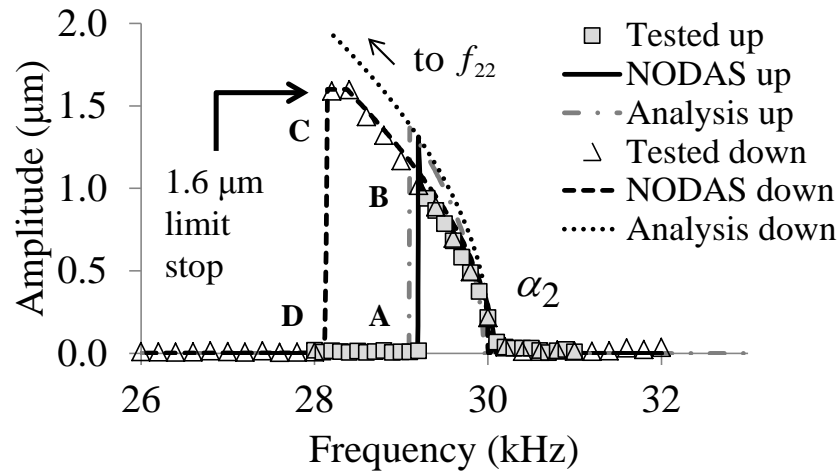
Figure 2-12: Analytic solution, behavioral simulation, and experimental results for bi-directional

sweeps. The experimental results are obtained with $V_{dc} = 40$ V and $V_{ac} = 20$ V. The contact of the

mechanical limit stop fingers forces the down-sweep to degenerate to the trivial solution.

In order to better predict the down-sweep transition frequency, a revision in design could be Simulation

made to increase the comb pitch such that it exceeds the maximum possible displacement of the limit stop

amplitude. In this case, the bifurcation at point E in Figure 1-4 could be experimentally validated; however, such a design revision is beyond the current scope of work. To predict the down-sweep bifurcation point with the presence of the limit stop fingers, a behavioral model of the limit-stop fingers is included to accurately predict the down-sweep transition frequency with the existing device in Figure 2-13.
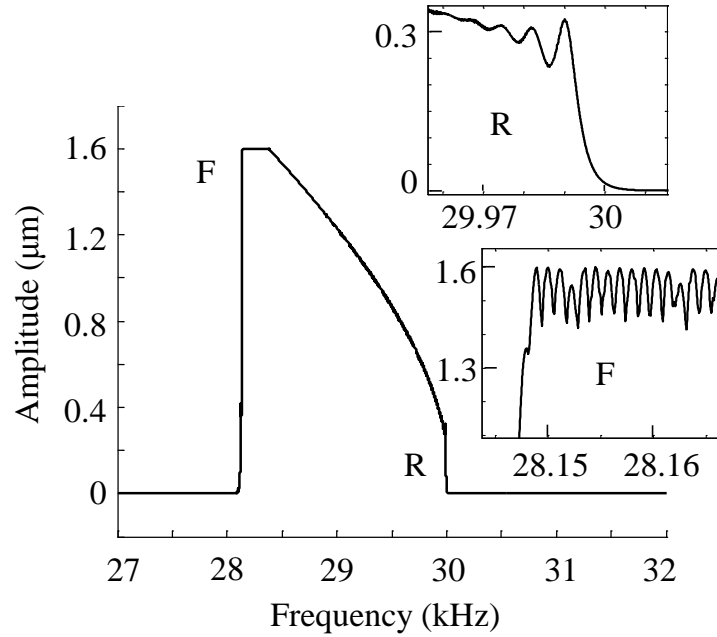
Figure 2-13: Amplitude response of the behavioral simulation for the frequency down-sweep with zoomed-in transients of the two bifurcation points (R and F). A limit stop model is included in the simulation to model the maximum allowable amplitude.

The transients at the "pitchfork" bifurcation point R and the transition point F at 1.6 μm (maximum displacement allowed by the limit stop) are shown in the zoom-in plots. The jump happens after the amplitude reaches the limit stop followed by a 190 ms dwell time, during

which time the limit stop fingers are in mechanical contact, creating the transients as shown in the zoomed-in plot F. The length of the dwell time depends on the speed at which the frequency is swept. The simulated down-sweep transition frequency with the limit stop model improves the match of the experiment to within 0.2%. The simulated frequency response is overlaid with analysis and experimental results in Figure 2-12.
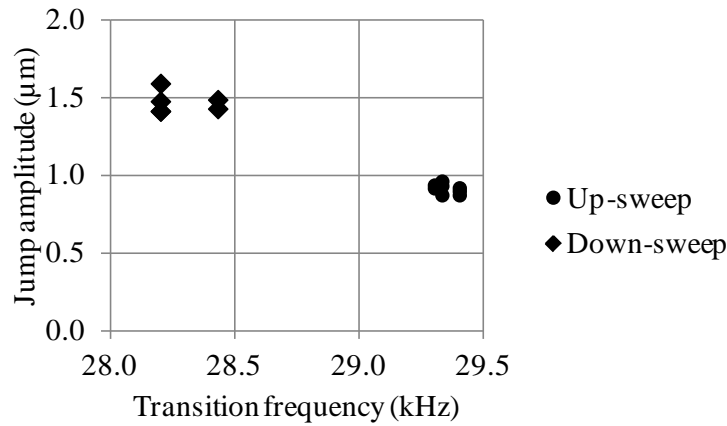
Figure 2-14: Repeatability of the parametric resonance envelope for bi-directional sweep tests. Each data point on the transition frequency–jump amplitude parameter space represents one test.

Repeatability tests are performed on the same testbed within a 12 hr time frame. The Confidence of measurement resonance state is observed optically at several ROI (region of interests) on the resonating plate and NIF. Measurement results are plotted in Figure 2-14 in the transition frequency–jump amplitude parameter space. Mechanical noise gives rise to variations in the bifurcation frequency and the amplitude. The variation in the down-sweep transition frequency is due to the relatively large frequency range that needs to be scanned in order to find the transition point,

46

which leads to a larger increment given the maximum number of measurement points allowed in the Microvision system.

Statistical analysis of the up-sweep transition frequency and the jump amplitude is performed Statistical analysis
under the presence of the uncertainty. The histograms produced from the Monte Carlo analysis of 100 samples are shown in Figure 2-15. The sidewall deposition of the metal-oxide stack which forms the CMOS-MEMS suspension contributes to the beam width uncertainty, which in turn, varies the spring stiffness coefficients. The effective Young's modulus of 70 GPa [38] also varies in the CMOS process. The bifurcation frequency, as a function of the mass, varies with metal layer area defining the moving structure, with the density of aluminum interconnect and inter-layer dielectric (ILD), and with the thickness of the metal-oxide stack, which is 4.83 μm measured from a FIB (focused ion beam)-etched cross section. Gaussian distribution is assumed in the uncertainty of the beam width w (standard deviation $\sigma = 23$ nm), thickness t ($\sigma = 0.05\ t$), Young's modulus E ($\sigma = 0.05\ E$), density ρ ($\sigma = 0.05\ \rho$) and the air gap ($\sigma = 20$ nm). These statistical data are from prior process test structures that were used to quantify the process and mismatch variation. The statistical analysis reveals that the mean of the bifurcation frequency and mean of the amplitude are 29.40 kHz and 1.36 μm, respectively, with corresponding standard deviations of 0.86 kHz and 0.02 μm. In the Monte Carlo analysis, the parametric resonance envelope in Figure 2-12 changes from run to run; the variation in the bifurcation frequency and amplitude are indicated by the horizontal axes of the histograms in Figure 2-15. Process variation of w, E and t are the three main contributors to the uncertainty of the bifurcation behavior, as determined by evaluating the correlation between these parameters. The

transition frequency and the jump amplitude are negatively correlated, as demonstrated by plotting all the data points on the frequency-amplitude parameter space.
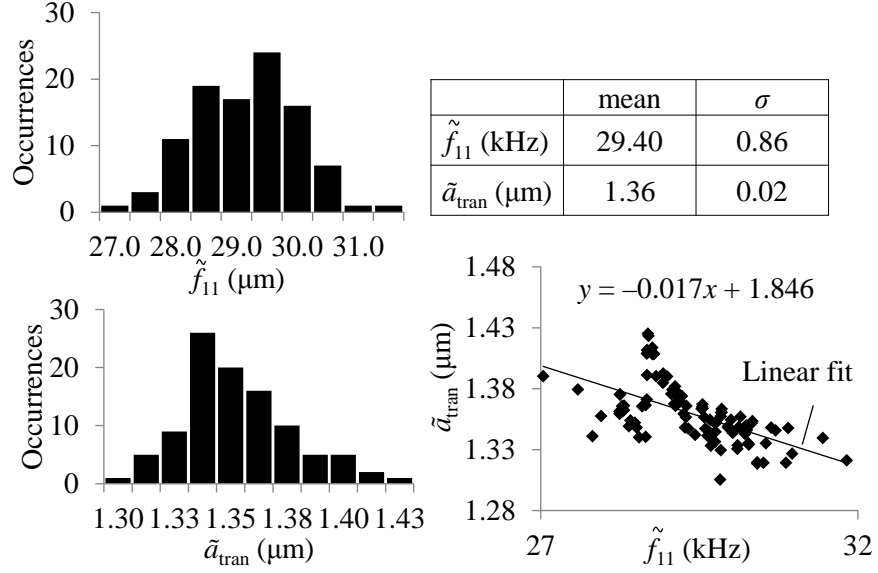
Figure 2-15: Statistical analysis of the transition frequency and the jump amplitude in the presence of the process variation and mismatch.

2.4. SUMMARY

This chapter validates the use of behavioral modeling in the analysis and design of nonlinear Summary parametric systems. A non-interdigitated finger comb resonator fabricated in the CMOS-MEMS process is used as the modeling example. A perturbation approach introduced in Chapter 1 is used to analyze the bifurcation phenomenon and provide physical interpretation of the jump event. The abilities of schematic-based simulation in exploring the transient behavior and damping facilitate the understanding of the complex system. Using parametric sweep in a

hierarchical system simulation, the relationship between the transition frequencies and the excitation voltages is established. The analysis and simulation match the experiment within 2.1% and 0.2%, respectively.

The behavioral modeling and the lumped model simulation provides an alternative design Outlook approach to complex nonlinear systems that could potentially lead to the exploration of new physical effects. Applicable to various MEMS dynamic designs, the model building methodology and the MEMS circuit library serve as a toolbox to shorten the design phase. Specifically, the exploration of parametric resonant topologies and corresponding control methods will benefit from the ability to accurately simulate full systems.

(end)

CHAPTER 3   HIGH-STROKE PARAMETRIC-MODE
ELECTROMECHANICAL DRIVES

E lectrostatic excitation of parametric resonance in (1.1) arises from several different electromechanical drive topologies. A class of non-interdigitated finger (NIF) comb drives [16], [17], and [18] has been widely used to provide a well-defined displacement-dependent force source. The NIF comb drive described in Chapter 2 has been widely used due to its simplicity in the comb finger design. It makes use of the fringing electric field generated between non-overlapping comb fingers to provide both linear and nonlinear electrostatic spring constants. However, since the NIF comb motion is constrained in the axis orthogonal to the finger length, its use is limited to a small stroke due to the required nonlinearity that only extends to a displacement equal to $\pm 1/2$ of the comb pitch. The maximum displacement is usually on the order of 1 μm, which is illustrated along the *x* axis in Figure 2-1 in Chapter 2.

Other applications requiring actuation schemes capable of a large motional stroke include $\boxed{\text{Motivation}}$ gyroscopes [20] that need larger displacement for better sensitivity and random number generators with high stroke chaos [11] behavior. Towards these ends, an electrostatic comb is synthesized that demonstrates a large stroke for parametric drive with a small design layout footprint. The "shaped-finger" comb utilizes a nonlinearly varying electrode gap to provide the necessary electrostatic stiffness for exciting parametric resonance with much larger stroke than

NIF combs. The shaped-finger comb moves laterally in the plane of the wafer, allowing sufficient clearance for large displacement motion.
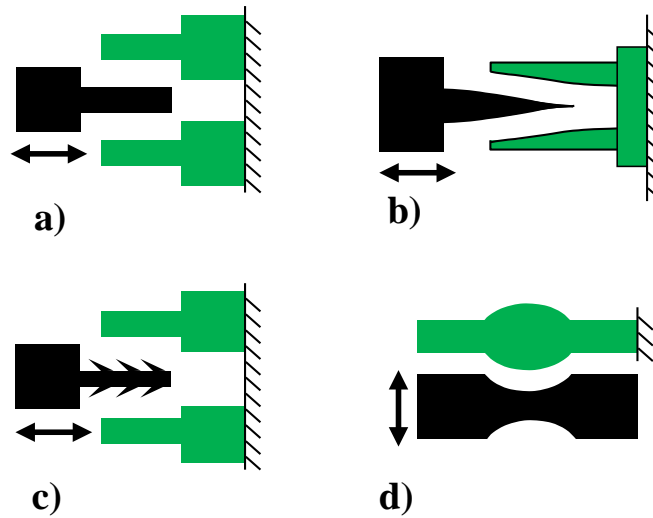
Figure 3-1: Shaped-finger designs for (a) assembly of small gap, (b)-(c) shaping force-engagement relationship, and (d) creating vertically-curved membranes. Arrows indicate motional direction.

Hirano *et al.* first reported the shaped-finger comb concept for the assembly of a small gap [Figure 3-1 (a)] to maximize the electrostatic force using a segmented comb with different widths [21]. The segmented comb used a stair-stepped finger profile with gradually decreasing widths to maximize the force magnitude as the fingers are engaged. In [22], Jensen *et al.* demonstrated the analytic model of planar shaped combs [Figure 3-1 (b)] for delivering electrostatic force with specific nonlinearity and described their tuning dynamics. The comb fingers were shaped by specific "shape functions" to allow customized force-displacement

History of the shaped-finger comb

responses. Additive curved features on planar rotor structures were extensively studied by O'Brien in [23] [Figure 3-1 (c)]. In an alternative design, Graham created out-of-plane shaped structures by forming a vertically-curved membrane using chemical mechanical polishing (CMP) [24] [Figure 3-1 (d)].

This chapter introduces a quadratic-shaped-finger comb that is intentionally designed to <u>Chapter outline</u> provide a linear electrostatic spring constant. Section 3.2 follows with the analytical parametric resonance solutions. The use of the quadratic-shaped-finger comb in a crab-leg resonator [25] to excite large-stroke (5 µm) parametric resonance is characterized in Section 3.3. A revised design with a folded-flexure suspension is characterized in Section 3.4. The revised design is stiff enough to constrain the in-plane body rotation while delivering a larger parametric stroke of 8 µm, providing a robust parametric excitation scheme.

3.1. QUADRATIC-SHAPED-FINGER COMB PARAMETRIC DRIVE

Shown in Figure 3-2 (a) is a micro optical image of the quadratic-shaped-finger comb <u>Device</u> parametric resonator with a close-up view of part of the folded-flexure suspension in Figure 3-2 b). The 45° tilted SEM views of the shaped-finger comb drive electrode (labeled I) and the straight-finger comb sense capacitor (labeled II) are shown in Figure 3-2 c). The resonator is fabricated in a silicon-on-insulator MEMS (SOI-MEMS) process [25] (Appendix C) with a 15 µm-thick silicon device layer and a 2 µm-thick buried oxide (BOX) spacer over a 480 µm-thick <111> silicon handle layer. The Si device layer is heavily boron doped to have a low resistivity of 0.001~0.003 Ω-cm.

The H-shaped shuttle mass consists of six stiff cantilevered plates along y and a connecting backbone truss along x. The folded flexure constrains the body rotation while allowing lateral motion in x. Both the shaped and the straight fingers are symmetrically placed along the periphery of the plates, and move in the x-direction. For the shaped-finger comb, the curved fingers are anchored and the straight fingers are attached to the rotor mass.
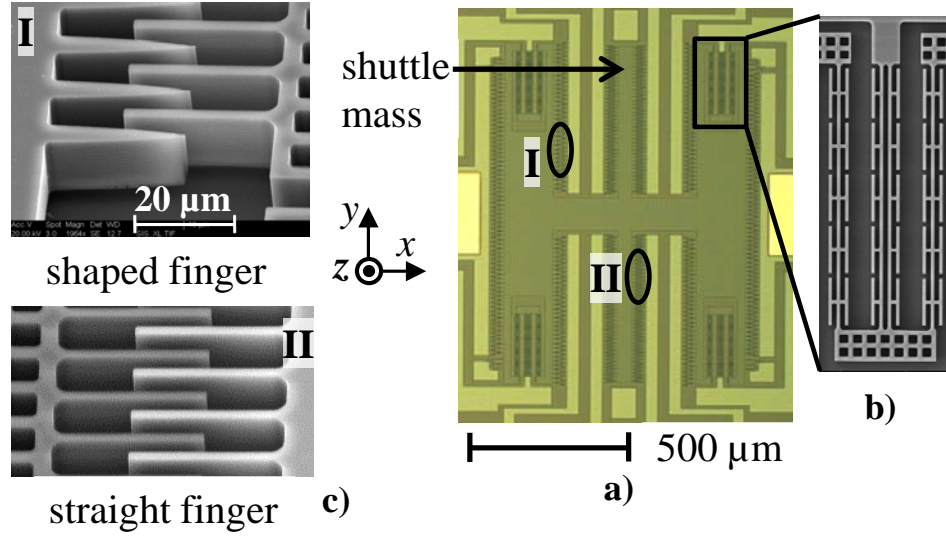
Figure 3-2: Optical image of an SOI quadratic-shaped-finger comb parametric resonator that moves in the x-direction with a folded flexure suspension in (b). Shown in (c) are the close-ups of I) shaped-finger comb and II) straight-finger comb.

As schematically shown in Figure 3-3, applying a suitable common-mode AC voltage $V_{p,ac} \cos(2\omega_r t)$ at twice the resonance frequency to the shaped fingers and a fixed DC potential $V_{p,dc}$ on the rotor fingers excites the parametric resonance. Symmetrically placed straight-finger combs sense the response dynamics electrically through a pair of external transimpedance

amplifiers (TIA) built with LF356 op-amps (Texas Instruments; Dallas, Texas, USA). Differential sensing helps to reject the feedthrough from the drive voltage through the substrate coupling. The feedthrough capacitance is matched by symmetric wiring placement on the layout. An HF2LI lock-in amplifier (Zurich Instruments; Zurich, Switzerland) detects the sense signal component at the mechanical resonant frequency ω_r. Common-mode pump drive voltage $V_{p,ac}$ at frequency of $2\omega_r$ is provided through an off-chip multiplier shown in Figure 3-4 built with an AD633 analog multiplier (Analog Devices, Norwood, MA), an LF356 op-amp, and a unity gain differential amplifier INA105 (Texas Instruments; Dallas, Texas, USA).
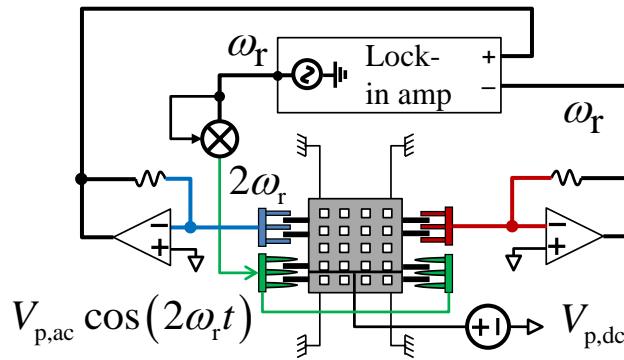
Figure 3-3: Schematic view of the shaped-finger comb resonator testbed using two off-chip transimpedance amplifiers.
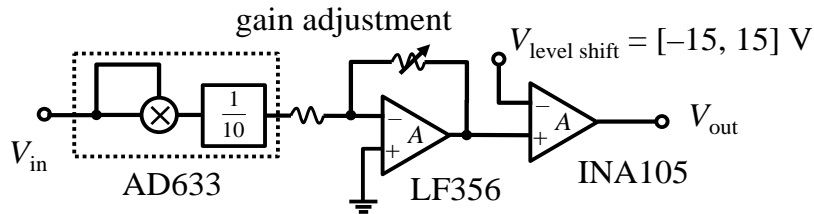
Figure 3-4: Schematic view of the analog multiplier circuit.

3.1.1. QUADRATIC-SHAPED-FINGER COMB ANALYTIC MODEL

The large-stroke electrostatic drive is a shaped-finger comb, with a nonlinearly varying gap Analytic
models
between the electrodes. The shaped-finger comb design is schematically shown in Figure 3-5.

The gap profile, g, varies with the position x_1 along the finger overlapped region:

$$g(x_1) = \frac{g_o}{1 + x_1/x_{o1}}$$ (3.1)

where the dimensional constant, x_{01}, is

$$x_{o1} = \frac{x_{ov}}{g_o/g_{ov} - 1}$$ (3.2)

The x_1 frame of reference moves with the rotor finger and always has its origin located at the tip
of the stator finger.
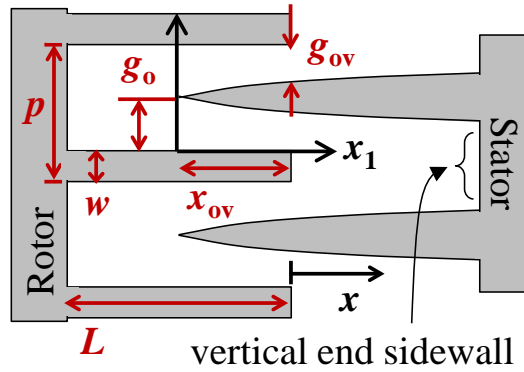
Figure 3-5: A schematic view of the quadratic-shaped-finger comb geometry.

Ignoring fringing field, integration of the gap along the overlapped region leads to the
capacitance for one side of the shaped-finger comb,

$$C_r(x) = \frac{2N\varepsilon_o h}{g_o} \int_0^{x_{ov}+x} \left(1 + \frac{x_1}{x_{o1}}\right) dx_1 \tag{3.3}$$

where x is the displacement of the rotor electrode, ε_0 is the permittivity of free space, h is the thickness of the Si device layer, and N is the number of straight rotor fingers. Taking the derivative of $C_r(x)$ with respect to x yields the electrostatic force applied to one side of the comb,

$$F_r(x) = \frac{V^2}{2}\frac{\partial C_r(x)}{\partial x} = \frac{N\varepsilon_o h}{g_o}\left(1 + \frac{x_{ov}+x}{x_{o1}}\right)V^2 \tag{3.4}$$

where $V = V_{p,dc} - V_{p,ac}\cos(2\omega_r t)$ is the voltage applied across the shaped-finger comb. Note that (3.4) is not symmetric about the origin. Thus, a non-zero force exerts on one side of the drive. In order to generate a parametric excitation force in the form of (1.1), symmetric placement of the shaped-finger comb is required and described next.

3.1.2. SYMMETRIC SHAPED-FINGER COMB DESIGN

Placing shaped-finger combs symmetrically on either side of the resonator results in comb finger location schematically shown in Figure 3-3, where combs are located on the outer banks of the resonator cantilever-like shuttle mass. The total capacitance is the sum of the capacitances of both sets of shaped fingers on left-hand-side and right-hand-side banks of the shuttle mass.

Force and capacitance models

$$C_{total}(x) = C_r(x) + C_r(-x) = \frac{2N\varepsilon_o h}{g_o}\left[2x_{ov} + \frac{x_{ov}^2}{x_{o1}} + \frac{x^2}{x_{o1}}\right] \tag{3.5}$$

The capacitance is a quadratic function of the displacement (*i.e.*, finger engagement), yielding the name "quadratic-shaped-finger" comb. Taking the derivative of $C_{\text{total}}(x)$ with respect to x and multiplying by $V^2/2$ yield the total electrostatic force,

$$F_{\text{total}}\left(x\right)=\frac{V^2}{2}\frac{\partial C_{\text{total}}\left(x\right)}{\partial x}=\frac{2N\varepsilon_o h}{g_o}\left(\frac{x}{x_{o1}}\right)V^2=-\gamma_1 x V^2 \tag{3.6}$$

where γ_1 is the linear electrostatic stiffness. $F_{\text{total}}(x)$ is a linear displacement-dependent force source when a voltage V is applied across the shaped-finger comb. The expression of the electrostatic force with only the linear displacement term implies that the net force exerted by the nonlinear drive is zero for zero displacement and the force is an odd function with respect to the resonator shuttle mass displacement.

One key feature of this shaped-finger comb is that the denominator of the gap profile Recap of $(1 + x/x_{o1})$ in (3.1) corresponds to the displacement-related term (x/x_{o1}) in the parenthesis of the models force-engagement relationship (3.6). A desired electrostatic spring constant is set by specifying the comb geometry parameters in the denominator of the gap profile in (3.1). The comb gap profile may be designed in a variety of shapes to generate custom nonlinear force-engagement responses [22] [25].

Linear electrostatic spring constant

From (3.2) and (3.6), the linear electrostatic spring constant is

$$\gamma_1 = -\frac{2N\varepsilon_o h}{g_o x_{o1}} = -\frac{2N\varepsilon_o h}{g_o \cdot \dfrac{x_{ov}}{\dfrac{g_o}{g_{ov}} - 1}} = -\frac{2N\varepsilon_o h}{x_{ov}}\left(\frac{1}{g_{ov}} - \frac{1}{g_o}\right) \tag{3.7}$$

The designed spring constant is a function of the number of rotor fingers per side, N, the gap at the curved finger tip, g_0, the overlap length, x_{ov}, and the gap at the straight finger tip, g_{ov}. Exploring the design space involving these design parameters, one can optimize the electrostatic force given a fixed design area and fabrication constraints.

3.1.3. DESIGN SPACE AND SCALING

The geometric parameters, along with their layout and measured values, are summarized in Table 3-1. The gap at the straight finger tip, g_{ov}, is set to a minimum value (3 µm), constrained by the SOI-MEMS process design rules.

Design parameters

Table 3-1: Shaped-finger comb geometric parameters

Symbol	Parameter	Layout	Measured
g_o	gap at the curved finger tip	5.0 µm	5.2 µm
g_{ov}	gap at the straight finger tip	3.0 µm	3.5 µm
x_{ov}	finger overlap	16.0 µm	13.6 µm
L	straight finger length	31.0 µm	31.4 µm
w	straight finger width	3.0 µm	2.6 µm
p	comb pitch	13.0 µm	13.0 µm
N	number of rotor fingers per side	139	139

Interaction effect of gap and overlap

By the scaling in (3.7), reducing the initial finger overlap, x_{ov}, increases the magnitude of the linear electrostatic spring constant magnitude, $|\gamma_1|$, whereas increasing the gap at the curved finger tip, g_o, while keeping N constant gives rise to a larger finger curvature and enhances the electrostatic spring constant magnitude. This interaction effect is illustrated in Figure 3-6.
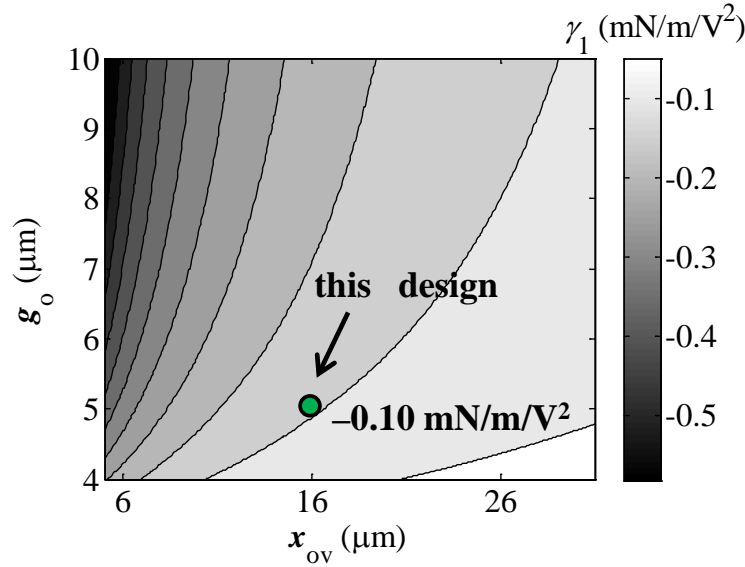
Figure 3-6: Scaling of the electrostatic spring constant with the overlapped finger length, x_{ov}, and the gap at the shaped finger tip, g_o.

The initial finger overlap (x_{ov}) needs to be a few microns larger than the 8 μm stroke to ensure ample overlap so the fringing-field remains a second-order effect. Meanwhile, x_{ov} must be small enough (less than 20 μm) to keep a reasonably big spring constant. The optimization between maximizing the electrostatic spring constant and keeping the first-order comb capacitance model assumption involves computation through a series of fringing electric field

simulations. To this end, x_{ov} is set to 16 µm to accommodate a 8 µm stroke with ample overlap remaining to ensure the first-order comb capacitance model holds.

Optimization of gap g_o

Predicted by the scaling in (3.7), smaller g_o lowers $|\gamma_1|$. Larger g_o widens the finger pitch and reduces N hence the spring constant, $|\gamma_1|$, for a fixed comb area. To illustrate this design trade-off, the electrostatic spring constant normalized to the area occupied by the comb, A_{comb}, is plotted against gap at the curved finger tip (g_0) in Figure 3-7, while keeping overlap (x_{ov} = 16 µm), gap at the straight finger tip (g_{ov} = 3 µm), and number of rotor fingers (N = 139) constant. The maximum linear electrostatic spring constant for a fixed comb area occurs for a $g_{o,m}$ = 6.67 µm gap at the curved finger tip (g_o). Below $g_{o,m}$, the decrease in g_0 leads to more rapid decrease in the electrostatic spring constant compared to the decrease in total comb area; beyond $g_{o,m}$, the comb area increase dominates, lowering the normalized electrostatic spring constant.
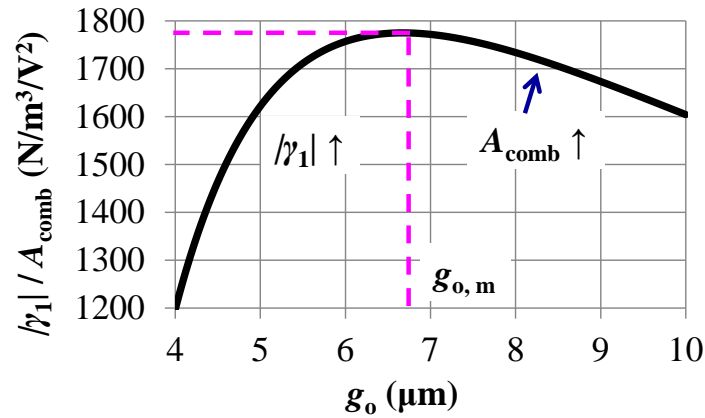
Figure 3-7: Normalized electrostatic spring constant magnitude versus the gap at the curved finger tip (g_0).

The optimum g_o can also be solved analytically using (3.7) and the comb area, A_{comb},

$$A_{comb} = 2N(2g_o + w)L_{comb} \tag{3.8}$$

where L_{comb} is the length of the comb in x. The electrostatic spring constant magnitude normalized to the area occupied by the comb is

$$\bar{\gamma}_1 = \frac{|\gamma_1|}{A_{comb}} = \frac{\dfrac{2N\varepsilon_o h}{x_{ov}}\left(\dfrac{1}{g_{ov}} - \dfrac{1}{g_o}\right)}{2N(2g_o + w)L_{comb}} \propto \frac{\dfrac{1}{g_{ov}} - \dfrac{1}{g_o}}{2g_o + w} \tag{3.9}$$

Taking the derivative of $\bar{\gamma}_1$ with respect to g_o yields

$$\frac{\partial \bar{\gamma}_1}{\partial g_o} \propto \frac{\dfrac{1}{g_o^2}(2g_o + w) - 2\left(\dfrac{1}{g_{ov}} - \dfrac{1}{g_o}\right)}{(2g_o + w)^2} = \frac{\dfrac{4}{g_o} + \dfrac{w}{g_o^2} - \dfrac{2}{g_{ov}}}{(2g_o + w)^2} \tag{3.10}$$

Optimum g_o, namely $g_{o,m}$, can be found by setting $\left.\dfrac{\partial \bar{\gamma}_1}{\partial g_o}\right|_{g_o = g_{o,m}} = 0$, thus

$$\frac{2}{g_{ov}} g_{o,m}^2 - 4g_{o,m} - w = 0 \tag{3.11}$$

Dropping the negative gap solution yields

$$g_{o,m} = \left(2 + \sqrt{4 + \frac{2w}{g_{ov}}}\right) \cdot \frac{g_{ov}}{2} \tag{3.12}$$

Since the ratio of w and g_{ov} is approximately 1:1 to 1.5:1 because they are set to the minimum value limited by the lithography, the optimum $g_{o,m}$ is determined predominantly by g_{ov}. For $g_{ov} = w = 3$ μm, the maximum linear electrostatic spring constant for a fixed comb area occurs for $g_{o,m} = 6.67$ μm. For $g_{ov} = 2$ μm and $w = 3$ μm, the maximum linear electrostatic spring constant for a

fixed comb area occurs for $g_{o,m}$ = 4.65 µm. The designed gap is rounded to 5 µm for these two design scenarios. This rounding also accounts for possible over-etch during the silicon DRIE (Deep Reactive-Ion Etching) and the linewidth decrease during lithography.

3.1.4. FINITE ELEMENT SIMULATION

Finite element analysis (FEA) is performed using geometric data from the fabricated device in Table 3-1. Figure 3-8 shows the workflow starting from an SEM image of the zoom-in view of the fabricated shaped-finger comb of the device under test (DUT). An edge detection technique using WinTopo (SoftSoft Ltd; Bedfordshire, UK) is performed on the SEM image followed by vectorization to create a profile that is imported into the FEA software COMSOL Multiphysics (COMSOL, Inc; Burlington, MA, USA). FEA workflow and software used

First, a 2D electrostatic FEA simulation is used to solve for the total capacitance using the technique developed in [17]. Integrating the total electric energy density $W_{e,s}$ over the area occupied by the surrounding air yields the total capacitance per unit thickness. Silicon DRIE attacks the bottom of the device layer, creating notches [45]. These notches on the finger consume 1.8 µm of silicon at the interface of the Si device layer and the BOX spacer layer. A second 2D FEA simulation of the cross-section uses a 45° tilted SEM view of the fingers to calculate the total thickness of the silicon after the DRIE notching and uses the correction factor by including the out-of-plane fringing fields in a separate simulation of a 3 µm gap straight finger cross section. These simulation outputs lead to an effective comb thickness and the total capacitance. Electro-static FEA

SEM **Edge detection**

Vectorization **Normal electric field distribution**
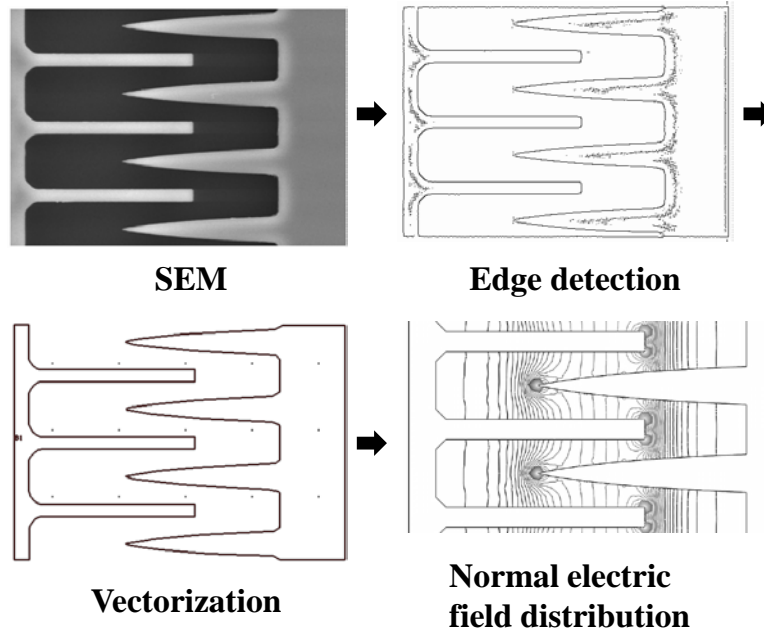
Figure 3-8: Finite element methodology for analysis of the fabricated shaped-finger comb.

An overlaid comparison of the analytic and FEA simulated $C_{total}(x)$ and $F_{total}(x)$ curves are shown in Figure 3-9. The simulated force reveals a cubic electrostatic nonlinearity with respect to x as the fingers are close to fully-engaged. This cubic stiffness is partly due to the finger profile change during the lithography, to the Si DRIE artifacts, and to the fact that the fully engaged fingers are close to the vertical end sidewalls (labeled in Figure 3-5), which yields larger electric field strength. This small nonlinearity is important in determining the overall system frequency response explained by the perturbation analysis developed in [17].

Overlaid analytic and FEA capacitance and force curves
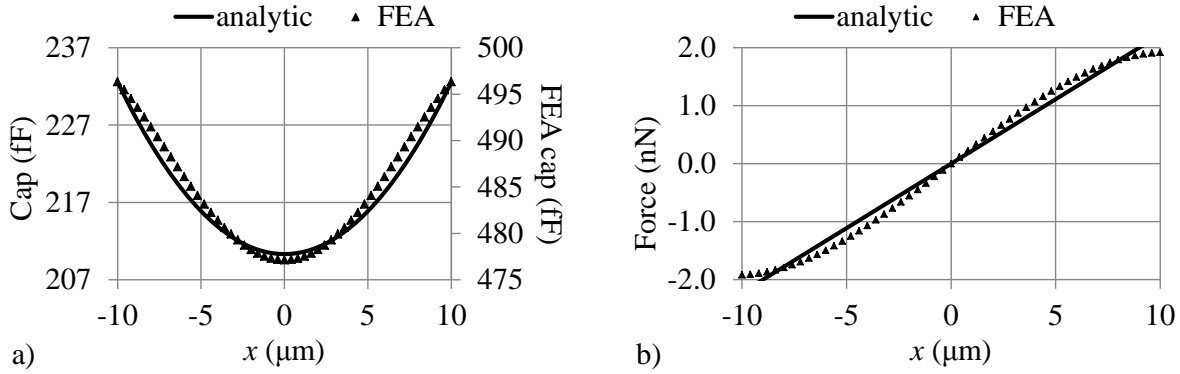
Figure 3-9: (a) Total capacitance and (b) electrostatic force versus the finger engagement x overlaid with FEA results for the symmetrically-placed quadratic-shaped-finger comb.

3.1.5. COMPARISON OF THE ELECTROSTATIC DRIVES

Like the interdigitated straight-finger capacitive comb, the shaped-finger comb moves laterally in the direction of the finger length perpendicular to the electric-field lines, allowing sufficient clearance for large displacement motion. A comparison of the quadratic-shaped-finger comb with the parallel-plate drive and other electrostatic excitation methods is listed in Table 3-2. Note in the table the direction of motion is indicated by the x axis.

Comparing electro-static drives

Parallel-plate drive

For the parallel-plate drive, the electrostatic force is

$$F_e = \frac{N\varepsilon_o hL_0}{2}V^2\left[\frac{1}{\left(g_o - x\right)^2} - \frac{1}{\left(g_o + x\right)^2}\right]$$

$$\approx \frac{2N\varepsilon_o hL_0}{g_o^3}V^2 x, \quad \text{for } x \ll g_o$$

(3.13)

Thus the electrostatic spring constant expression,

$$\gamma_1 = \frac{2N\varepsilon_o h L_0}{g_o^3} \tag{3.14}$$

is only valid for very small displacement x. Thus to accommodate a displacement stroke equal to $x_m = 15.0$ μm, the gap g_o has to be sufficiently larger than x_m. In this calculation, the gap is set to $g_o = 3 \, x_m$. To justify the choice of this gap value, a plot of electrostatic force, F_e, with respect to the displacement, x; together with the slope of the $F_e - x$ relationship at $x = 0$, are shown below:
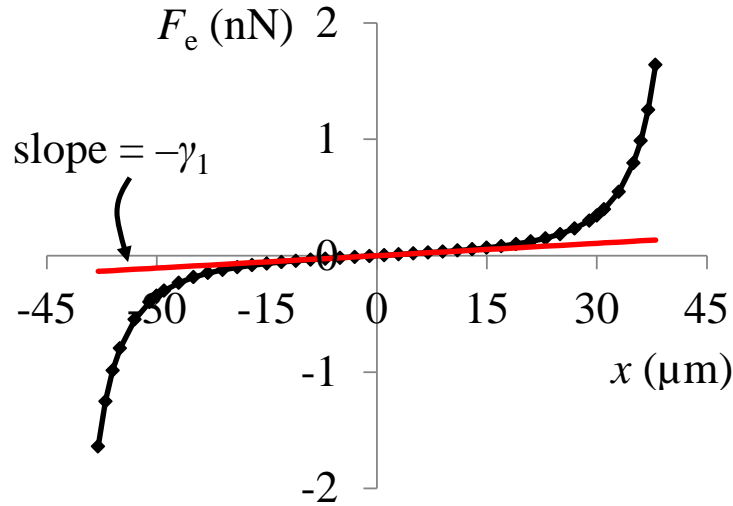
Figure 3-10: Electrostatic force, F_e, exerted by the parallel-plate drive is plotted with respect to the displacement, x.

The linear least-square fitting is evaluated by the coefficient of determination (a.k.a. R^2 value) in Figure 3-11. The fitting is accurate ($R^2 > 0.99$) when the maximum displacement is less than 15 μm.

Least-square fitting R^2 value
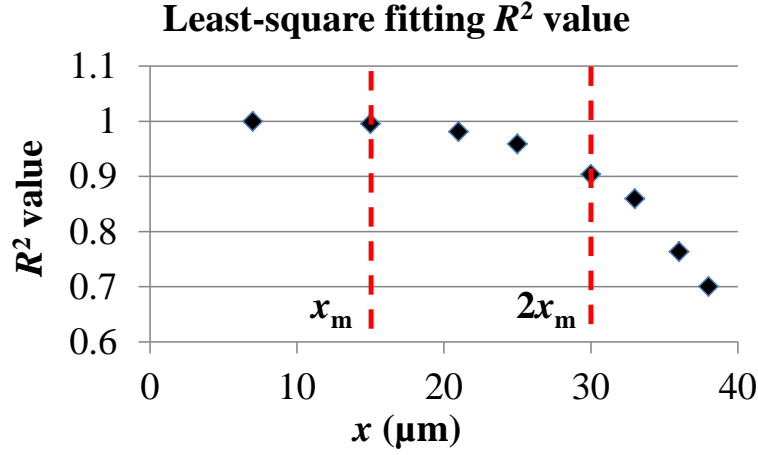
Figure 3-11: Coefficient of determination (R^2 value) of the least-square fitting for the electrostatic force of the parallel-plate drive evaluated at different displacement limits.

The area for the parallel-plate drive is

$$A_{\text{comb}} = 2NL_y \left(w + g_o \right) \tag{3.15}$$

Another assumption is imposed so that enough clearance is given in y

$$L_y = 2L_o \tag{3.16}$$

The normalized linear spring constant, $|\gamma_1| / A_{\text{comb}}$, of the parallel-plate capacitive comb is

$$\left(\gamma_1 / A_{\text{comb}} \right)_{\text{p-p}} = \frac{N \varepsilon_o h}{\left(3x_m \right)^3 2N \left(w + g_o \right)} \tag{3.17}$$

Quadratic-shaped-finger comb versus the parallel-plate drive

For the quadratic-shaped-finger comb, the analytical linear spring constant is given by (3.7) and the comb area, A_{comb}, is given by (3.8). The normalized linear spring constant is given by

(3.9). The ratio of the normalized linear spring constant, $|\gamma_1| / A_{\text{comb}}$, of the quadratic-shaped-finger comb to the parallel-plate capacitive comb is

$$
\begin{aligned}
\frac{(\gamma_1 / A_{\text{comb}})_{\text{shaped}}}{(\gamma_1 / A_{\text{comb}})_{\text{p-p}}} &= \frac{\dfrac{\varepsilon_o h}{x_{\text{ov}}}\left(\dfrac{1}{g_{\text{ov}}} - \dfrac{1}{g_o}\right)}{(2g_o + w)L_{\text{comb}}} \times \frac{2(3x_m)^3(w + g_o)}{\varepsilon_o h} \\
&= \frac{2(3x_m)^3}{L_{\text{comb}} x_{\text{ov}}}\left(\frac{1}{g_{\text{ov}}} - \frac{1}{g_o}\right)\frac{(w + g_o)}{(2g_o + w)}
\end{aligned}
\tag{3.18}
$$
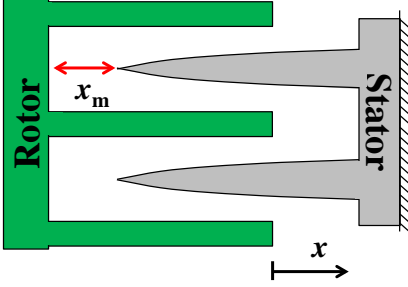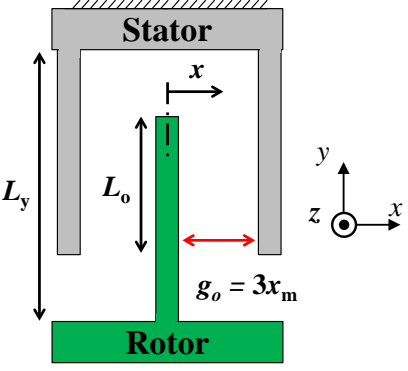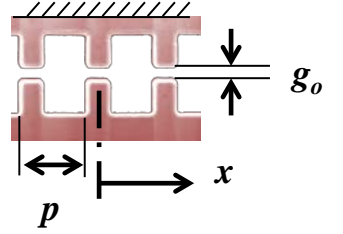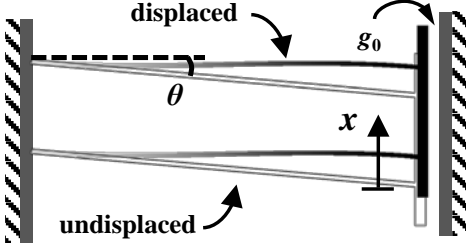
where L_{comb} is the length of the shaped-finger comb and is equal to

$$
L_{\text{comb}} = x_{\text{ov}} + 2x_m
\tag{3.19}
$$

Thus the ratio is roughly proportional to the square of the maximum stroke:

$$
\frac{(\gamma_1 / A_{\text{comb}})_{\text{shaped}}}{(\gamma_1 / A_{\text{comb}})_{\text{p-p}}} = \frac{2(3x_m)^3}{(x_{\text{ov}} + 2x_m)x_{\text{ov}}}\left(\frac{1}{g_{\text{ov}}} - \frac{1}{g_o}\right)\frac{(w + g_o)}{(2g_o + w)}.
\tag{3.20}
$$

Table 3-2: Comparison of the quadratic-shaped-finger comb with other electrostatic comb drives

	Comb shape		Max stroke x_m	$|\gamma_1| / A_{comb}$
			μm	N / m^3/ V^2
Quadratic-shaped-finger comb (Geometric parameters in Table 3-1)			15.0 (tested maximum stroke: 8 μm)	1621.8
Parallel-plate drive			1.25	163471.3
			15.0	13.3
Non-interdigitated comb			1.25	284679.9[†]
			15.0	142.9[††]
Tangential drive[†††]			15.0 (tested maximum stroke: 10 μm)	682.9

[†] Calculated using design parameters in [40]: $g_o = 0.8$ μm, $p = 5$ μm.

[††] Using literature value in [40] and scale to: $g_o = 3$ μm, $p = 60$ μm, such that the maximum stroke is $p/4 = 15$ μm.

[†††] Calculated using design parameters in Appendix B.3.

3.2.   PARAMETRIC RESONANCE SOLUTIONS

From (1.5), the nonlinear Mathieu equation that governs the behavioral of parametric $\overline{\text{Mathieu}}$ $\overline{\text{equation}}$ resonator is repeated here:

$$m\ddot{x} + b\dot{x} + k_1 x + k_3 x^3 = -\left(\gamma_1 x + \gamma_3 x^3\right)\left[V_{p,dc} + V_{p,ac}\cos\left(\omega t\right)\right]^2 \tag{3.21}$$

Definitions and values for the system parameters are given in Table 3-3 using the device described in Figure 3-2 as an example. The design parameters in the table are the measured values.

Table 3-3: Shaped-finger comb resonator design parameters

Symbol	Parameter	Value
m	total mass	9.0 μg
b	damping coefficient	2.4 μkg/s
k_1	linear mechanical spring constant	17.3 N/m
γ_1	linear electrostatic stiffness	-2.8×10^{-4} N/m/V^2
γ_3	cubic electrostatic stiffness	8.9×10^{5} N/m^3/V^2
$V_{p,dc}$	DC parametric drive voltage	60 V
$V_{p,ac}$	AC parametric drive voltage	3.3 V
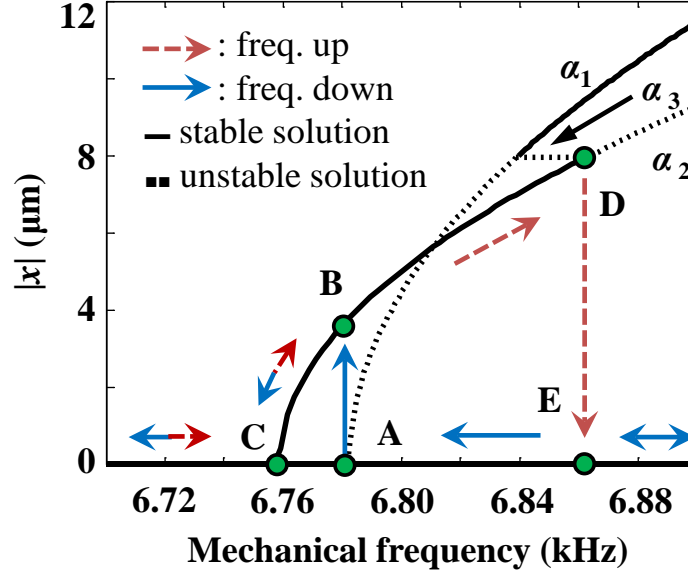
Figure 3-12: Steady-state frequency response of the folded-flexure shaped-finger comb parametric resonator revealing hardening nonlinearity.

The nonlinear Mathieu equation (3.21) is a second-order differential equation with a periodically time-varying electrostatic parametric excitation. Its estimated analytical solutions are provided by perturbation theory [15] in Chapter 1, Section 1.2. The steady-state solutions of (3.21) and their nonlinear stability analysis are included in Appendix A. Employing the method of averaging [30] to solve (3.21) yields three non-zero steady-state solutions of the form

$$x(t) = \alpha_i \cos\left[\omega t/2 + \beta_i(t)\right]. \tag{3.22}$$

Two of the solutions a_1 and a_2 bend to the right, indicative of stiffening nonlinearity. The third solution a_3 is a constant amplitude solution. Applying the techniques developed in [17] and [40]

to the quadratic-shaped-finger comb resonator, the analytic steady-state response is plotted in Figure 3-12 versus the mechanical frequency (the frequency of x).

The parametric frequency response is obtained by chirping (*i.e.*, sweeping) the excitation Frequency response frequency with time in the region of twice the system's resonant frequency. As previously described in Chapter 1, for most values of the drive frequency, the system is not stimulated and the solution is at $x = 0$. After passing the bifurcation frequency, the system establishes automatic parametric resonance, which builds oscillation amplitude that would grow without bound if not for damping in the system.

The bifurcation phenomenon demonstrated in Figure 3-12 exhibits the hysteresis effect. The Bifurcation and steady-state solutions a_1, a_2 and a_3 are separated by the bifurcation frequencies (*i.e.*, points A, C, hysteresis and D) into different regions with well-defined stability as shown on the figure. The physical steady-state amplitude of the system always lands on the stable branches, while the unstable branches are not physically realizable in steady-state. The zero displacement solution is always stable in steady-state, but it is not practical between points A and C, because noise will trigger a jump to a_2. For a decreasing frequency sweep, the resonator displacement remains zero until reaching the bifurcation point A, where a sharp jump from A to B happens. The amplitude gradually decreases to zero by following the solution a_2 from B to another "pitchfork bifurcation" point C. On the other hand, for an increasing frequency sweep, parametric resonance builds up after C and increases to a "saddle-node bifurcation" point D in steady-state, where the amplitude drops to zero (point D to E). The bifurcation frequency and the resonance

amplitude depend heavily on the system mechanical and electrostatic linear stiffness and the combined nonlinearity [17].

3.3. CHARACTERIZATION OF A SHAPED-COMB RESONATOR WITH CRAB-LEG SUSPENSION

The first validation vehicle of large-stroke parametric resonance excited by an in-plane $\boxed{\text{Motivation}}$ "shaped-finger" electrostatic comb drive is a crab-leg resonator. The custom-shaped comb drive electrode geometry used to produce a quadratic capacitance-engagement response was described in Section 3.1.

An SEM of a shaped-finger comb parametric resonator suspended by four crab-leg springs is $\boxed{\text{Device}}$ shown in Figure 3-13, with a close-up view of part of the crab-leg suspension. Also shown are the zoom-in perspective SEM views of the shaped-finger comb drive electrode and the straight-finger comb sense capacitor geometries. The resonator is fabricated in a 15 μm-thick silicon-on-insulator MEMS (SOI-MEMS) process [25] (Appendix C). The shuttle mass consists of six stiff cantilevered plates along y and a connecting backbone truss along x. Like the folded-flexure resonator in Figure 3-2, both the shaped and the straight fingers are symmetrically placed along the periphery of the plates and move in the x-direction. Parametric drive is realized by applying a common-mode voltage $V_{p,ac}$ to the shaped stator fingers while fixing the straight rotor fingers at a DC potential $V_{p,dc}$. The DC voltage across the shaped comb can also be adjusted for electromechanical frequency tuning. Differential sensing with symmetric wiring placement provides feedthrough rejection.
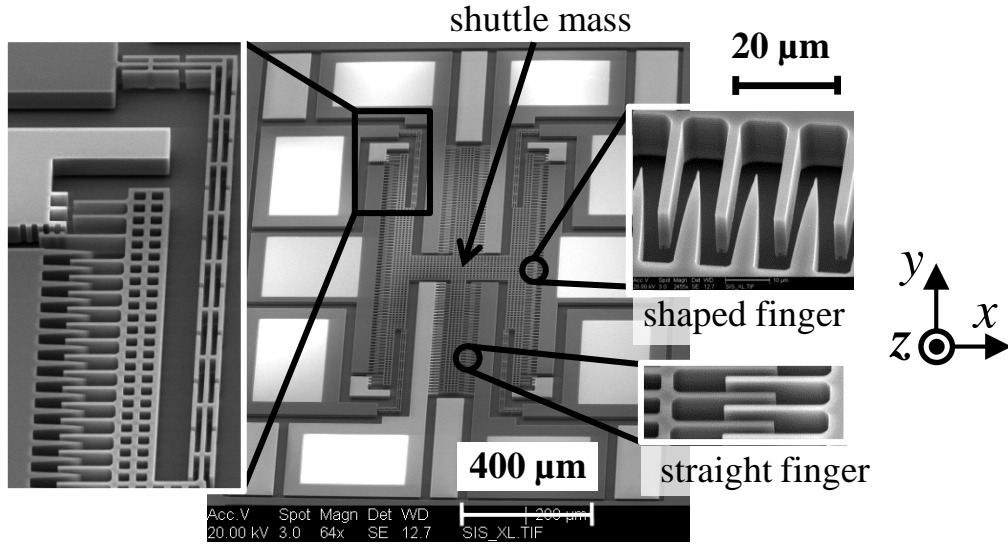
Figure 3-13: SEM of an SOI-MEMS quadratic-shaped-finger comb parametric resonator suspended by a crab-leg suspension.

3.3.1. HARMONIC RESPONSE AND TUNING DYNAMICS

The harmonic vibration test result is shown in Figure 3-14. In atmospheric pressure, the Measured harmonic response quality factor (Q) of the harmonic resonance is 26 due to significant Couette damping between the movable Si plate and the underlying Si substrate, which is 2 µm below the plate. The amplitude at the resonance is 1.5 µm and the designed maximum stroke is 15 µm, so that the resonator stays within the linear regime. Bi-directional frequency sweeps are performed to confirm no hysteresis effects happen at low amplitude.
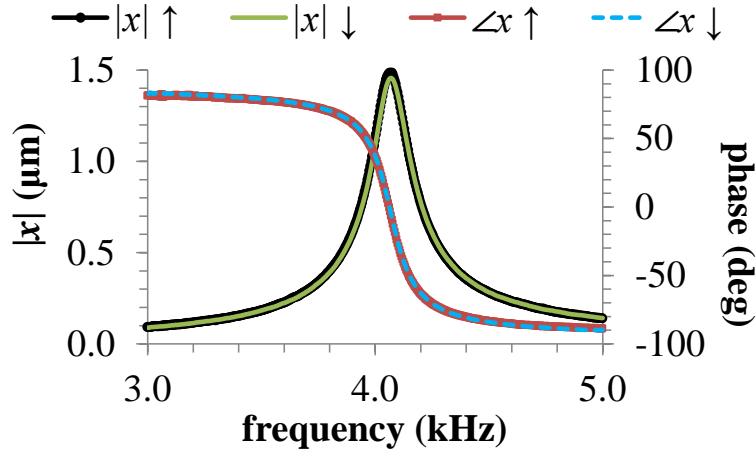
Figure 3-14: Crab-leg resonator tested harmonic response in air. Symbol ↑ is the frequency up-sweep; ↓ is the frequency down-sweep.
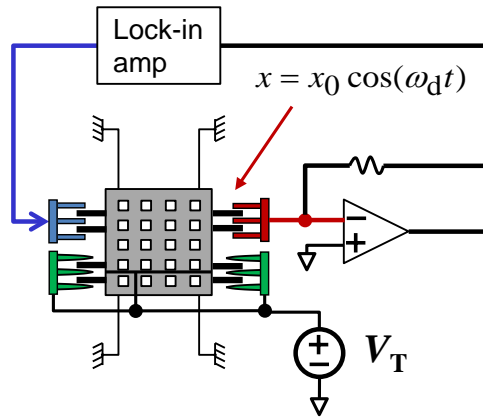
Figure 3-15: Harmonic response and frequency tuning measurement setup.

In Figure 3-15, the tuning dynamics of the quadratic-shaped comb are investigated by Tuning dynamics applying a DC tuning voltage, V_T, on the shaped comb and exciting the straight parallel-plate capacitive drive to obtain the shifted resonance frequency. Figure 3-16 shows a relatively large

tuning of 17.3% at 80 V DC tuning voltage without pull-in issues. The tuning from the experiment matches the analytic prediction within 3.9%.
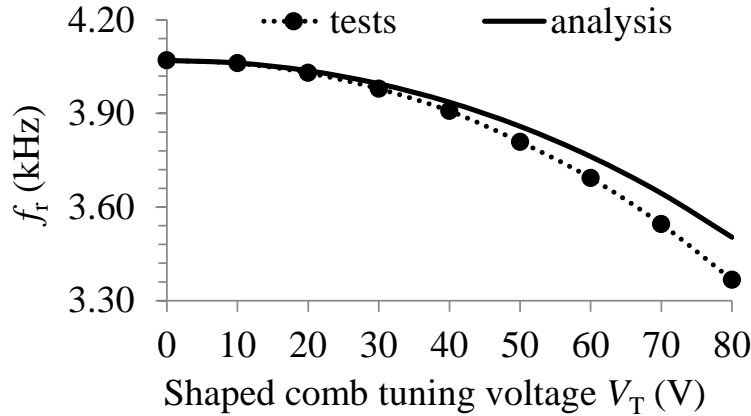
Figure 3-16: The tuned resonance frequency versus the shaped comb tuning voltage V_T.

The system is also operated at 28 mTorr inside a custom vacuum chamber and achieves a Q Low pressure harmonic test of 14250, as shown in Figure 3-17.
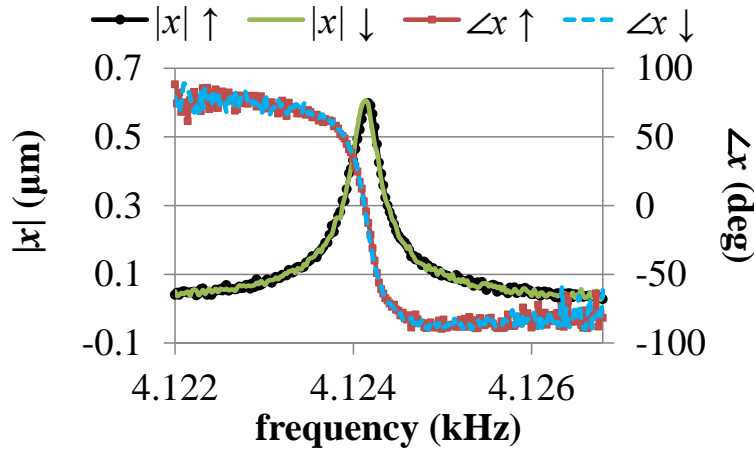
Figure 3-17: Crab-leg resonator measured harmonic response in a vacuum of 28 mTorr.

3.3.2. PARAMETRIC RESPONSE

The testbed schematic used to validate the parametric mode is shown in Figure 3-18. It is revised from the optical vibration test setup for detecting the bifurcation and its amplitude in [16] and Chapter 2. The drive voltages are $V_{p,dc} = 60$ V and $V_{p,ac} = 5$ V. The test was performed in air. The use of optical vibration test enables observability of spurious mode by imaging the motion.
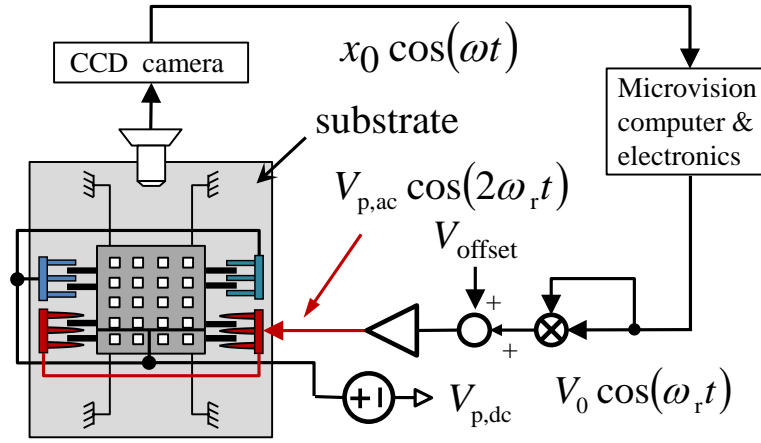
Figure 3-18: Optical vibration testbed for parametric response.

The large-displacement bifurcation response of the crab-leg parametric resonator is shown in Figure 3-19. The resonator driven parametrically by a quadratic-shaped comb reveals a 4.8 μm bifurcation step at 8.9 kHz, which is three times larger in displacement than the previously reported NIF resonators [16] and [17] . There are discrepancies in bifurcation frequency and the jump amplitude with respect to the analytic solution due to the finger profile change during the Si structure lithography and DRIE. An extra theta mode (*i.e.,* body rotation) is observed through the blur image taken by the Microvision system. Compared to the layout design, the additional lateral silicon etch in the SOI-MEMS process shifts the second resonance mode (the theta mode)

to lower than 20 kHz, which is sufficiently close to the second harmonic of the drive signal, creating a significant body rotation. This theta mode moves the comb fingers sideways in *y*, reducing the finger gap. The stator shaped fingers and the rotor straight fingers snap in, resulting in the second jump (the leftmost jump in Figure 3-19). This instability makes it impractical to extract the exact resonant frequency of the theta mode. Section 3.4 introduces a revised design that uses the folded-flexure suspension to eliminate this extra theta mode by providing a stiffer spring in the *y* and the rotational axes.
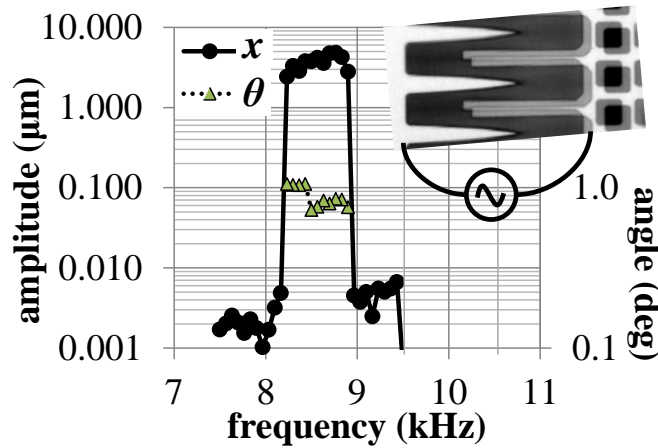
Figure 3-19: Tested quadratic-shaped-finger comb crab-leg resonator parametric response with a frequency down-sweep.

3.4. CHARACTERIZATION OF A SHAPED-COMB RESONATOR WITH FOLDED FLEXURE SUSPENSION

Extra body rotation that exists in the device described in Figure 3-13 is eliminated with a Motivation proper design of a spring suspension that predominantly moves in one axis and rejects motion in

77

the orthogonal axis. One example of this class of spring is a folded-flexure design, shown in Figure 3-2. Measurements are performed to measure large-stroke parametric resonance that is excited using the quadratic-shaped-finger comb design in Section 3.1. These measurements validate the analytic parametric resonance solution found in Section 3.2. Prior to characterizing the parametric resonance, the device is driven into harmonic resonance by the straight-finger comb capacitor to obtain the natural resonant frequency and the quality factor. Both the harmonic and parametric responses were measured using the capacitive sensing circuit from Figure 3-3.

3.4.1. HARMONIC RESPONSE

The harmonic vibration test results are shown in Figure 3-20(a) using a 60 V DC polarization voltage and a 1 V AC harmonic actuation voltage. The measured resonant frequency is 6.985 kHz. The quality factor (Q) of the resonator in atmosphere is 51 due to significant Couette damping between the movable Si plate and the underlying Si substrate, which is 2 µm below the plate. The low resonant amplitude ensures that the resonator stays within the linear regime under harmonic excitation. The designed maximum stroke is 15 µm. No hysteresis effects are observed in bi-directional frequency sweeps.

Quality factor was enhanced to 13030 by driving the resonator in a vacuum of 24 mTorr, at 60 V DC with a reduced 0.5 mV AC drive, as shown in Figure 3-20(b). A slight asymmetry is seen in the phase response of Figure 3-20(b). This is possibly due to the small but non-zero mechanical nonlinearity inherent in the folded-flexure suspension. This small nonlinearity

Measured harmonic response

becomes significant when driven at high amplitude or in a vacuum under which the device has a high Q.
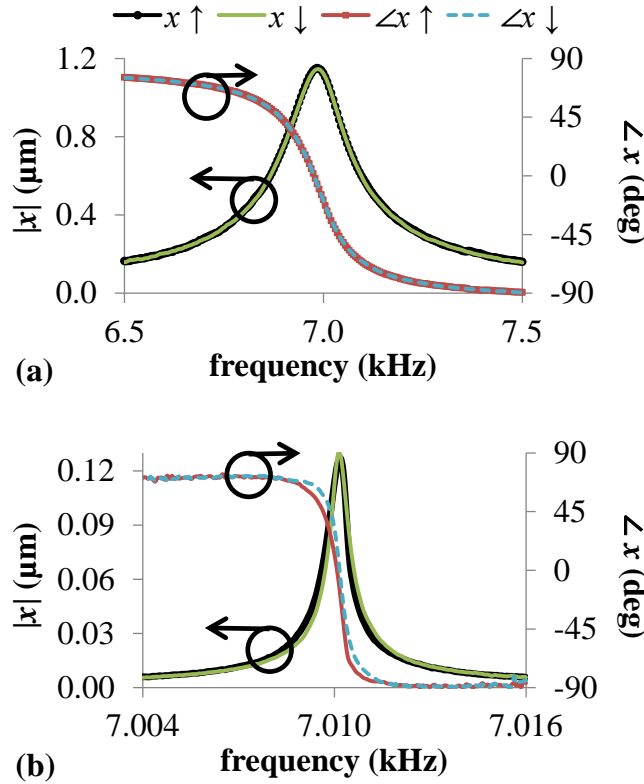
Figure 3-20: Measured harmonic frequency response driven by a straight-finger comb capacitor (a) in air, and (b) at 24 mTorr. ↑ and ↓ correspond to the frequency up-sweep and down-sweep, respectively.

3.4.2. LARGE-STROKE BIFURCATION – FREQUENCY DOMAIN RESPONSE

Given the natural resonant frequency from Section 3.4.1, a parametric excitation voltage is Drive voltage constructed whose frequency was set around twice the system's resonant frequency. The waveforms

analytic steady-state parametric response driven by a quadratic-shaped-finger comb is validated using the experimental testbench schematically shown in Figure 3-3. A frequency doubler located after the lock-in amplifier output provided the AC parametric drive voltage $V_{p,ac}$ of 3.3 V and 13.8 kHz to the shaped fingers. The 60 V DC parametric polarization voltage $V_{p,dc}$ is applied on the rotor fingers. The frequency of the parametric drive voltage is double that of the displacement $|x|$ signal at 6.88 kHz, as evidenced in Figure 3-21.
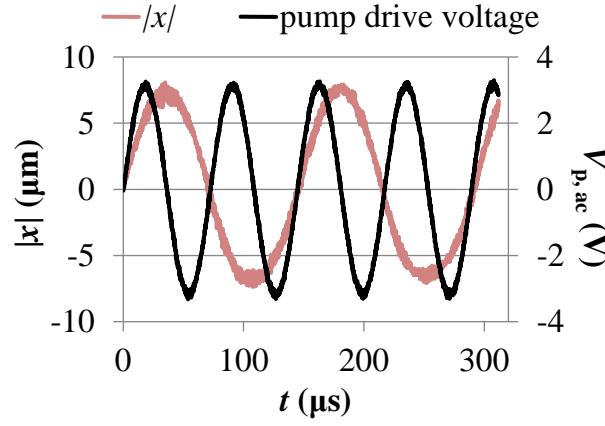
Figure 3-21: Electrical pump drive voltage $V_{p,ac}\cos(2\omega_r t)$ and displacement amplitude $|x|$ for parametric resonance at operating point D on Figure 3-12.

One benefit of the parametric sensing testbed is its ability to reject the electrical feedthrough [6] signal at the parametric drive frequency. The parametric resonance occurs at an electrical drive frequency of $2\omega_r$, while the mechanical response is intrinsically around the system's resonance frequency ω_r. By demodulating the response signal at the resonant frequency ω_r, a narrow bandwidth low-pass filter with high-order roll-off rejects the electrical

Discussion of the drive frequency

80

drive feedthrough signal that is shifted by demodulation from $2\omega_r$ to ω_r. Higher-order demodulation components at $2\omega_r$ and $3\omega_r$ are also rejected.
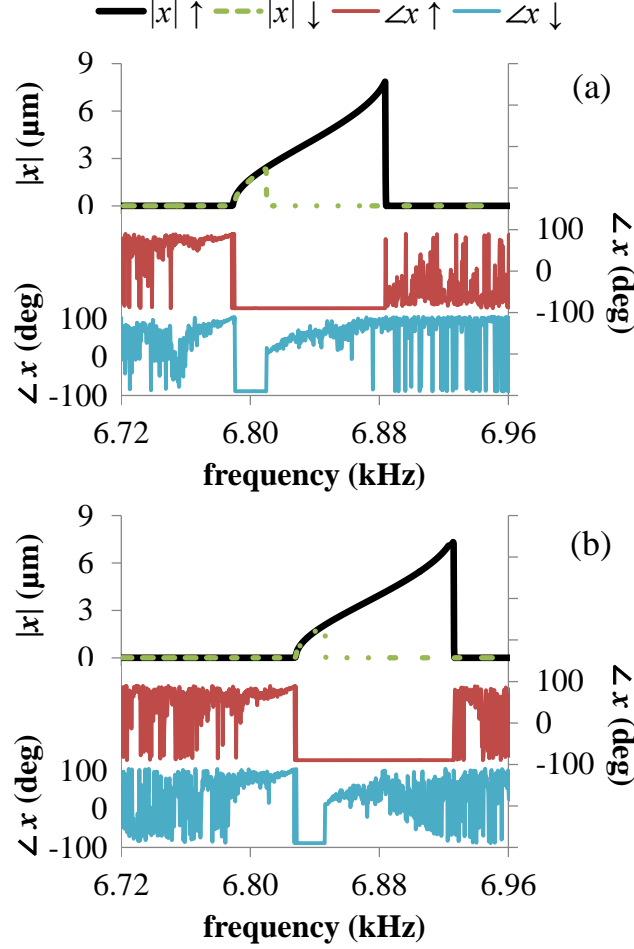
Figure 3-22: Measured large-stroke parametric response with bi-directional frequency sweeps for (a) 60 V DC and 3.3 V AC, and (b) 55 V DC and 3.3 V AC.

Chirping the frequency bi-directionally yields the large-displacement bifurcation response of the resonator, as shown in Figure 3-22(a). An 8.0 μm step in displacement amplitude at the

Measured bifurcation

6.884 kHz bifurcation point is observed for the frequency up-sweep for the drive voltage of 60 V DC and 3.3 V AC under a vacuum of 26 mTorr. This is five times larger in displacement than previously reported NIF resonators [16] [17] (Chapter 2). Figure 3-22(b) shows a higher bifurcation frequency for the drive voltage of 55 V DC and 3.3 V AC, indicative of the presence of a softening nonlinearity.

A typical parametric resonator has a minimum detectable signal on the order of 5 pm with a 225 Hz bandwidth in open-loop operation [28]. The frequency down sweep reveals a relatively low-amplitude bifurcation jump of 2.3 µm at 6.810 kHz. The measured bifurcation frequencies match the analytic solution plotted in Figure 3-12 within 1%. The slope increase of the $|x| - f$ curve at large amplitude is not predicted analytically by Figure 3-12 and was observed by Requa *et al.* [27]. This phenomenon needs further simulation verification.

Discussion

3.4.3. TIME-DOMAIN RESPONSE

The transient response near the bifurcation point D in Figure 3-12 for the frequency up-sweep is plotted in Figure 3-23. The frequency is swept with a time step of 1.9 s with an increment of 0.6 Hz. The transient starts at a frequency tripping point X, which is at the saddle-node bifurcation frequency of 6.884 kHz (near the theoretical saddle-node point D in Figure 3-12 with a frequency of 6.86 kHz). The phase is given enough time to settle before a second step change in the swept frequency at point Y. The phase reverts continuously to a stable steady-state of 50.4° after a transient which lasts approximately 0.7 s. The coherency in phase after the jump is due to the signal feedthrough at frequency ω_r from the printed-circuit-board which houses the

Time-domain transient of the bifurcation

frequency doubler. The amplitude drops from 8.0 µm to zero as the phase settles. The long resettling time gives crucial information regarding the stabilization of the bifurcation phenomenon at the jump point. The 0.7 s duration of the resettling transient is evidence of the complex dynamics in the plant on the edge of the bifurcation point [34]. Measures would have to be taken to ensure this long resettling time is avoided to stabilize a closed-loop controller [35] to be discussed in Chapter 4 and Chapter 5.
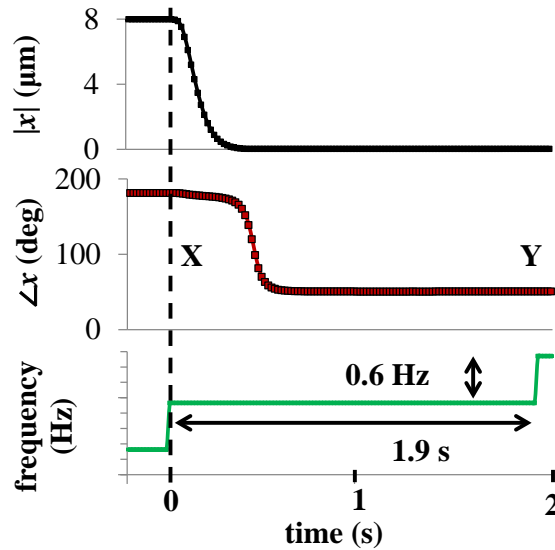
Figure 3-23: The transient near the frequency up-sweep saddle-node bifurcation point.

The transients at the bifurcation point due to a step turn-on followed by a step turn-off in the AC voltage are shown in Figure 3-24. The AC parametric drive voltage of 3.3 V is stepped on at 9.8 s. When AC voltage is turned on, the frequency of the drive is fixed at 6810.2 Hz, which is the down-sweep bifurcation point. The DC parametric drive voltage of 60 V remains unchanged throughout the measurement. The step response amplitude $|x|$ and phase $\angle x$ are recorded at the

Turn-on and turn-off dynamics

rate of 225 samples per second. As seen in Figure 3-24(b), immediately following the step turn-on of the AC voltage, after a dead time of 0.2 s, the displacement amplitude increases from zero to 2.3 µm. This transient is partially explained theoretically by a time-domain solution of an undamped linear Mathieu equation derived using the method of multiple time scales [15]. At the onset of the parametric bifurcation jump, the displacement x as a function of time t is

$$
\begin{aligned}
x = x_o & \left[e^{\frac{1}{2}\varepsilon\omega_r t} \left(\cos\omega_r t - \sin\omega_r t \right) + e^{-\frac{1}{2}\varepsilon\omega_r t} \left(\cos\omega_r t + \sin\omega_r t \right) + \text{H.O.T.} \right] \\
& = x_o \left[2\cos\omega_r t \times \cosh\left(\frac{1}{2}\varepsilon\,\omega_r t \right) - 2\sin\omega_r t \times \sinh\left(\frac{1}{2}\varepsilon\,\omega_r t \right) + \text{H.O.T.} \right]
\end{aligned}
\tag{3.23}
$$

where x_0 is a characteristic dimension that is proportional to the comb length, and H.O.T. stands for the higher-order terms. From (1.16), ε is the dimensionless parametric linear electrical stiffness equal to $\gamma_1 V^2_{\text{ac}} / (2k_1) = -0.0035$. The theoretical value of the exponential time constant, $|4\pi/\varepsilon\omega_r|$, is 0.1 s, which is strongly affected by the nonlinearities. The measured time constant is 0.4 s for the turn-off transient. Improving the analytical model by considering the damping effect would improve the match. Figure 3-24(c) shows the step turn-off in the AC voltage amplitude $V_{\text{p,ac}}$. The transition between zero and non-zero (2.3 µm) states defines the time-domain transition of the jump and affects the design of a bifurcation-based controller [34] to be discussed in Chapter 4 and Chapter 5.
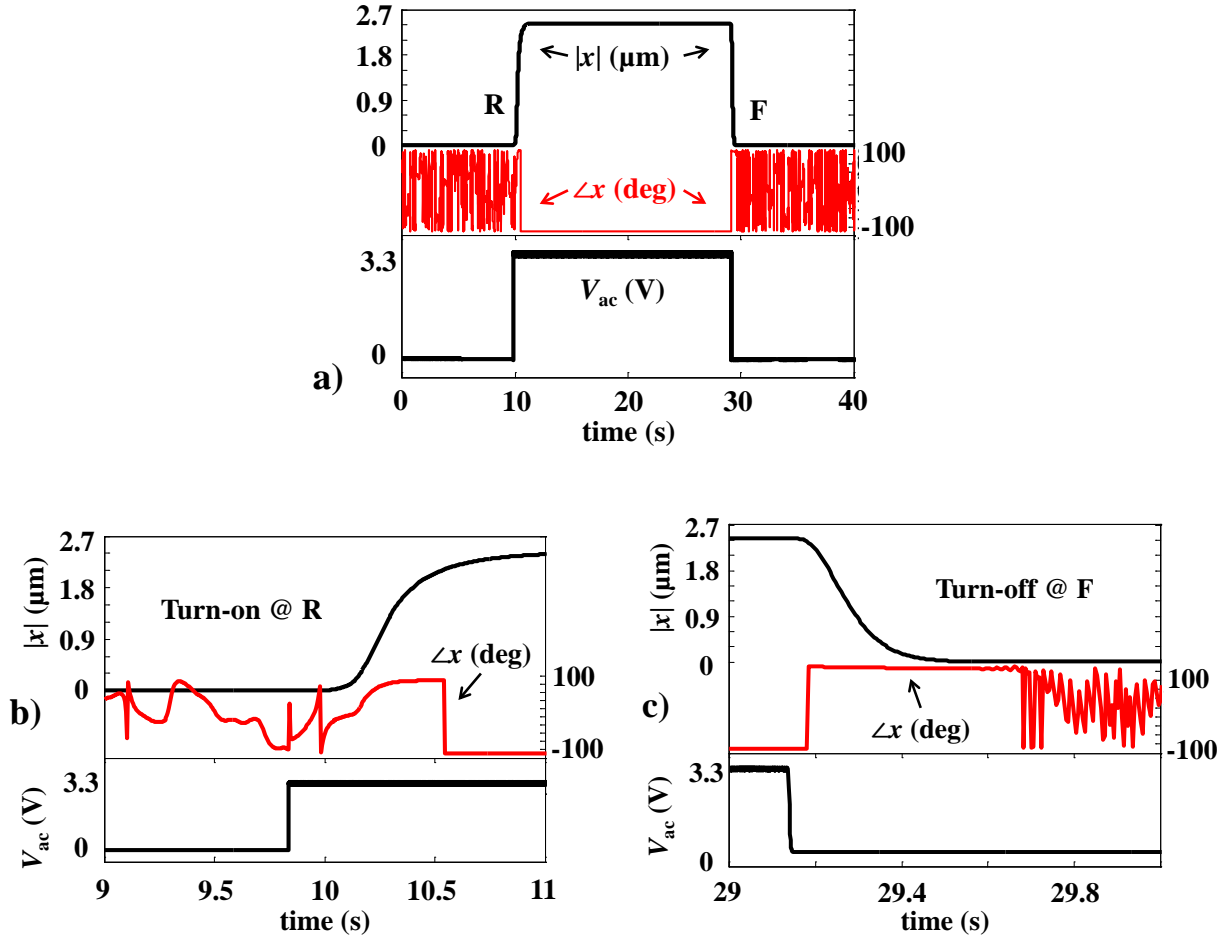
Figure 3-24: (a) The step turn-on, (R), and turn-off, (F), transients at the down-sweep bifurcation 6.810 kHz. (b) Zoom-in of step turn-on transient, R. (c) Zoom-in of step turn-off transient, F.

3.5. SUMMARY

The use of quadratic-shaped-finger combs to customize the linear electrostatic spring Shaped-finger design stiffness coefficient gives rise to a large-displacement (8 μm) parametric response, as validated by experimental results. The design of the comb-finger shape dictates the dependency of the

electrostatic force on the rotor finger displacement. The specific design of a quadratic capacitive engagement response (*i.e.*, $C \propto x^2$) for the shaped-finger comb leads to a linear voltage-controlled spring constant such that the large displacement parametric drive is achievable. Electrostatic spring nonlinearities, added to the linear spring term, can be designed purposefully or may arise as an artifact from incomplete modeling of the three-dimensional nature of the electrostatic fields between fingers. Presence of such nonlinearities generally sets the limits on the parametric resonance amplitude.

The quadratic-shaped-finger comb successfully provides the necessary nonlinearity to demonstrate large-stroke nonlinear parametric resonance. The ability of providing large displacement response for relatively small pump excitation voltages could be applied to future low power automatic electrostatic parametric excitation schemes. The linear electrostatic tuning dynamics and the scaling law of the same quadratic-shaped-finger comb drive are essential in synthesizing a comb profile that delivers large oscillation amplitude and a high tuning range.

Tuning and large stroke capability

Characterization of the quadratic-shaped-finger comb parametric resonators with different suspensions show that the crab-leg spring gives rise to a parasitic theta rotation mode when exciting parametric resonance whereas the folded-flexure suspension eliminates the unwanted theta mode.

Effect of spring

Observations of transients on the edge of the bifurcation are useful in experimentally investigating the dynamics of the bifurcation behavior, which may provide information on future design of a pump drive with optimal system dynamics. The step turn-on dynamics investigate the transitions in the displacement amplitude and the phase on the edge of the parametric jump.

Time-domain transients

These transient responses provides the time necessary for the bifurcation to change between a zero displacement state and a non-zero state. These time-domain transitions, together with the hysteresis, are critical in determining parametric controller dynamics as discussed in Chapter 4.

(end)

CHAPTER 4   BIFURCATION-POINT CLOSED-LOOP
CONTROL TECHNIQUES

The study of nonlinear dynamics and parametric resonance effects in resonant micro- and nanomechanical systems has extended over two decades. Mass [1], chemical absorption [2], and stress all contribute to the resonant frequency shift, which links to the parametric bifurcation frequency shift. Since the bifurcation is instantaneous, to the first order, the amplitude noise does not affect the bifurcation frequency. Tracking of the bifurcation frequency shifts enables sensitive detection of attogram mass [3] or spring constant change, even with the presence of the injected amplitude noise [2].

Exploring ultrasensitive detection of mass or stress had led to many detection schemes. Early implementations use the open-loop frequency sweep method [1], [13] to measure the change in the bifurcation frequency point, where the frequency of the drive is swept through the parametric resonance region until a jump is identified and its frequency is recorded. However, the open-loop method is slow due to the long time (generally a few minutes) it takes to complete one measurement that exploits quasistatic operation points. This drawback makes the open-loop sweep method impractical for automatic sensor applications.

Continuous automated detection of bifurcation frequency shifts with sub-Hz precision is only possible if a control approach can be designed to servo on the bifurcation frequency edge. Compared with the harmonic resonator, on which the linear feedback control approach generally

suffices, classical linear control approaches applied to the parametric resonator fail due to the hysteresis and the latch-up instability on the edge of the bifurcation [35]. The buildup and ring-down time that are associated with the high-Q mechanical system and the parametric instability also destroy the controller stability.

One bifurcation-based analog control scheme [4] is implemented by observing the coherency of the signal phase. It is designed such that the resonant amplitude is kept very small (140 pm) in order to lock into the phase coherency to avoid the slow time bifurcation jump event that is required to travel from the zero state to the non-zero state.

Analog parametric control

A frequency-state controller that varies the frequency of the parametric drive was first attempted in order to servo on the bifurcation edge. The description of this approach is in Section 4.2.3. The parametric drive voltage is fixed while the drive frequency is varied. The frequency is set by the loop to have only two states. At one state the frequency is set so the resonance amplitude is non-zero; at a second state the frequency is changed so the amplitude is zero. Switching between zero and non-zero effectively places the servo setpoint at the bifurcation. However, this approach fails due to the hysteresis that creates a limit cycle comprising alternating amplitude response patterns with non-zero and zero amplitude.

Frequency state control

The balance of this chapter describes a amplitude-state parametric controller to successfully control at the bifurcation with large drive amplitude while avoiding latch-up instabilities. The large displacement operation enhances its robustness in the presence of detection noise. The servo uses fine-grained control of the DC drive voltage, $V_{p,dc}$, while fixing the drive frequency. This DC drive gain is set by the feedback control loop. The controller tracks on the edge of the

Amplitude-state control

bifurcation, and thus on the shifts in nonlinear resonance characteristics. The servo operates in two states: the "on" state enters the rising edge along the amplitude jump manifold; the "off" state backs off into the zero solution region so the resonance is about to turn off. The control loop has an adjustable threshold, thus capable of servoing on different preset oscillation amplitude levels. An exemplary system is demonstrated at 1.9 μm amplitude with an equivalent 4.5 Å resolution. The states are cycled by 200 kHz pulse width modulation that circumvents the slow latch-off and turn-on as would happen in quasistatic operation with analog feedback.

Secondary effects of the parametric resonance such as instability and hysteresis render the Controller simulation controller design for such a system intractable analytically. Accurate system-level modeling of the complex nonlinearity of the parametric resonator facilitates the rapid exploration and design of the control loop topologies and parameters. Simulation testbeds built from an interoperable hierarchical circuit model library [40] are used for the control topology exploration and component selection as well as optimization of the loop parameters. For example, the control plant is modeled with lumped models of explicit governing ordinary differential equations and macro models with characteristics extracted from finite element analysis (FEA). Electrical models are incorporated together with the mechanical subsystems to form a complete top-level electromechanical system. The co-simulation of microelectromechanical dynamics with the analog circuitry enables the simulation of the complete control loop and the investigation of the stability and limit cycle. The simulated loop parameters assist in building an off-chip parametric controller to be used in validation experiments.

4.1.   BIFURCATION DIAGRAM

4.1.1. BIFURCATION LOCUS

Using the non-interdigitated comb resonator in Chapter 2 as an example[1], the frequency Loci of bifurcation response in Figure 1-4 is re-plotted in Figure 4-1(b) zooming in to the up-sweep bifurcation frequency region. The bifurcation points f_{11} (point A) and f_{21} (point F) are graphically represented in Figure 4-1(a), which defines the "tongue" (or "wedge") as the two loci of the pitchfork bifurcation points. The right curve is the pitchfork bifurcation f_{21} where the trivial solution α_4 intersects with the non-zero stable region of α_2 [point F in Figure 4-1(b)]; the left curve is the pitchfork bifurcation f_{11} where α_4 intersects with the non-zero unstable region of α_1 [up-sweep jump frequency at point A in Figure 4-1(b)]. Figure 4-1(a) is called the "bifurcation diagram" that draws the boundaries between the non-zero solution ("on" region) and zero solution regions ("off" regions) for the frequency up-sweep tests in this system with a softening nonlinearity. The amplitude in the non-zero region is limited by the cubic stiffness nonlinearity. In Figure 4-1(a), the DC polarization voltage, V_{dc}, is fixed to 40 V, consistent with Figure 4-1(b). The design parameters are summarized in Table 2-1 in Chapter 2.

---

[1] Although the controller plant to be discussed in this chapter is the quadratic-shaped-finger-comb resonator from Chapter 3, the NIF resonator is chosen to introduce the bifurcation diagram concept. This is due to NIF resonator's relatively wide separation between two pitch-fork bifurcation points. Using NIF as a numerical example helps to better illustrate the "on" and "off" regions.

Figure 4-1: Bifurcation diagram showing the boundaries between the non-zero solution and zero solution regions in the DC bias voltage – frequency parameter space.

The changes in the drive voltages modify the system's effective spring constant, which affects the bending of the resonance curve and the regions where the system enter the non-zero solution region. In a typical nonlinear resonator, the drive voltage shapes the tongue. The

Bifurcation
frequency
v.s. V_{ac}

tongue width measured in frequency depends on the AC drive amplitude V_{ac}. On the boundary of the "wedge", the denormalized transition frequency as functions of DC polarization voltage, V_{dc}, and the AC parametric excitation voltage, V_{ac}, is

$$f_{tran}\left(V_{dc}, V_{ac}\right) = 2f_{r0}\sqrt{1 + \frac{\gamma_1 V_{dc}^2}{k_1}\left(1 \pm \frac{\gamma_1 V_{ac}^2}{4k_1}\right)}, \qquad (4.1)$$

where the "−" and "+" terms inside the parenthesis correspond to the left and right wedges, respectively. Figure 4-1(a) quantifies the effect of V_{ac} on the two pitchfork bifurcation points. Increasing V_{ac} moves the bifurcation frequency f_{21} to the right in a quadratic manner. Similarly, f_{11} decreases with the increasing V_{ac}.

4.1.2. LINEAR ELECTROSTATIC TUNING

Adjusting the DC polarization voltage, V_{dc}, shifts the entire frequency response curve in Effects of V_{dc} Figure 4-1(b), resulting in changes in the locations of points A and F. The position of the bifurcation diagram tongue along the frequency axis is a strong function of V_{dc}. Allowing V_{ac} to simultaneously change with V_{dc} (here, $V_{ac} = 0.5V_{dc}$), the bifurcation frequencies are

$$f_{tran}\left(V_{dc}\right) = 2f_{r0}\sqrt{1 + \frac{\gamma_1 V_{dc}^2}{k_1}\left(1 \pm \frac{\gamma_1 V_{dc}^2}{16k_1}\right)}. \qquad (4.2)$$

Varying V_{dc}, the curves in Figure 4-1(a) bend and are shown in Figure 4-2. For a softening comb, where linear electrostatic spring constant $\gamma_1 < 0$, the curves bend to the left, indicative of electrostatic softening phenomenon. For a stiffening comb, where $\gamma_1 > 0$, the curves bend to the right, indicative of electrostatic hardening phenomenon.
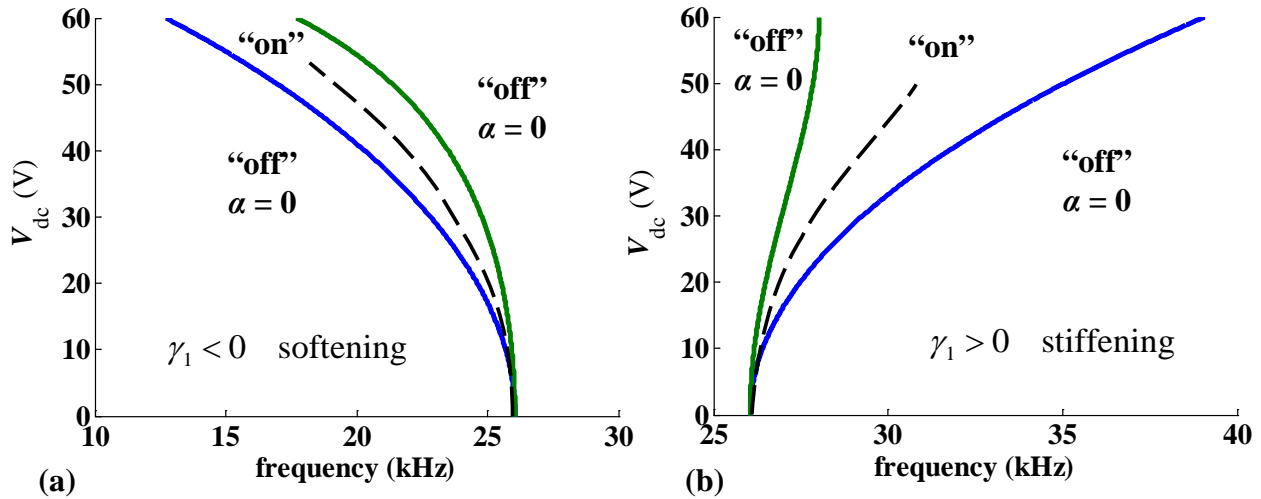
Figure 4-2: Effect of DC polarization voltage on the bifurcation diagram. The wedge could bend towards (a) left for a softening comb, or (b) right for a stiffening comb.

Figure 4-2(b) uses the design parameters from Table 2-1 and the applied voltages (V_{ac} = 0.5V_{dc}) are consistent with Figure 4-1(b), where V_{dc} = 40 V and V_{ac} = 20 V. It provides the combination of excitation frequency and the DC polarization voltage that define the boundary between "on" and "off" regions for an example NIF resonator. The bifurcation diagram impacts the servo topology exploration as well as the choice of its steady-state operation points on the edge of the bifurcation [4], [34], and [35]. Details on this can be found in Sections 4.2.3 and 4.3.

4.1.3. EFFECT OF AIR DAMPING

The transition curves Figure 4-3 are overlaid with the simulated pitchfork bifurcation points Effects of damping in air with shear and squeeze-film damping effects. The air damping shrinks the non-zero region by lifting the boundary curves from the frequency axis and narrowing them in the V_{dc}–frequency plane, which is explained theoretically in [33]. The excitation of the automatic parametric resonance (*i.e.*, excitation only through the parametric drive force) requires more energy in air than in vacuum. However, the transition dynamics of the parametric resonance remains sharp and the jump boundaries can still be accurately defined [1]. The behavioral modeling testbed incorporating air damping in the simulation of bifurcation frequencies and the simulation methodology are included in Chapter 2.
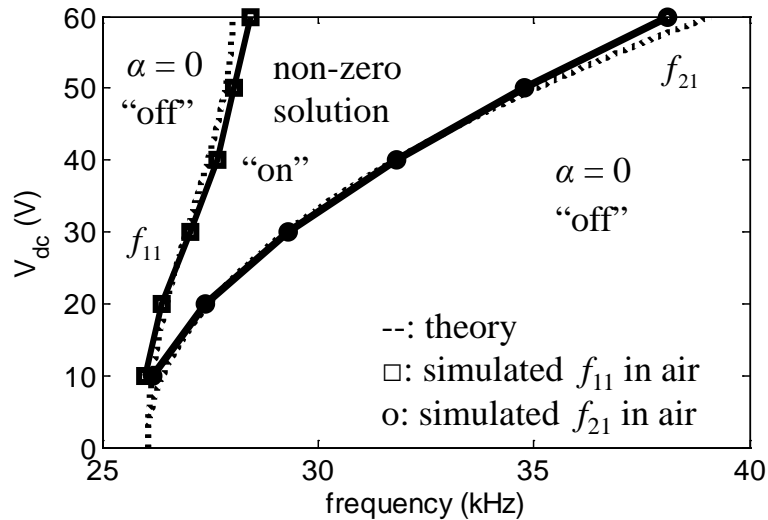
Figure 4-3: Analytic bifurcation diagram overlaid with simulated frequency boundaries considering atmospheric air damping.

4.2.   BIFURCATION CONTROLLERS – A REVIEW

4.2.1. LINEAR ANALOG CONTROLLER

A linear analog parametric controller is used to investigate the possibility of servoing on the Controller description

edge of the instability utilizing linear controllers. The servo point is chosen at the onset of the

pitchfork bifurcation point. The oscillation amplitude is kept small enough to avoid the slow

buildup time from the zero to the non-zero amplitude. The parametric drive frequency and the

corresponding AC excitation voltage amplitude are fixed to 29 kHz and 5 V, respectively. The

system is driven near the parametric resonance point. The DC drive gain is set through the

control loop and can take continuous values whose range covers the steady-state bifurcation

point, shown schematically in Figure 4-4.

Figure 4-4: Controlled states of the linear analog servo with the range of the DC drive gain

labeled in red.

The controller schematic is shown in Figure 4-5. The displacement amplitude is compared with a preset threshold value to yield error signal that is fed into a proportional-integral-derivative (PID) controller. Its output is used to set the required DC polarization amplitude through series connected gain and level shifting stages. The hypothesis is that the feedback enables continuous adjustment of the operation point to servo on the edge of the bifurcation.
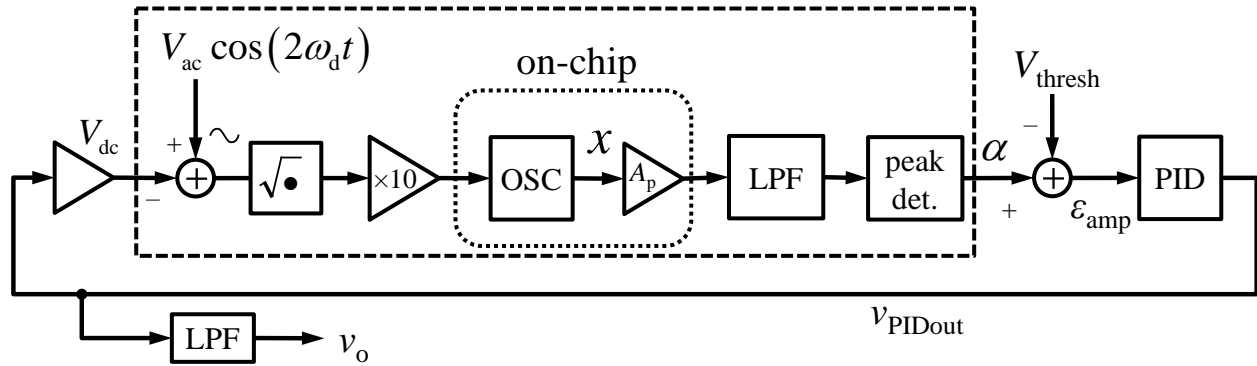
Figure 4-5: Block diagram of the linear analog parametric controller.

The first 20 ms of simulation is shown in Figure 4-6. x is the displacement, x_{LPF} is the Failure displacement signal after passing the low-pass filter (LPF), v_{Pout} is the output of the peak detector, ε_{amp} represents the resulting waveform after the threshold subtraction, v_{PIDout} is the output after the PID controller with the proportional controller coefficient $k_p = 0.2$ and integrator coefficient $k_i = 20$. The failure mode is evidenced by the buildup of the amplitude. The resonance stays within 2 nm before it starts building up at roughly 7.2 ms and then rings afterwards. The buildup of the resonance disables the loop from tracking the parametric

resonance point. Thus, to author's knowledge, special control schemes are required to stabilize the controller.

x (nm)

x_{LPF} (nm)

v_{Pout} (V)

$\varepsilon_{\mathrm{amp}}$ (arb)

v_{PIDout} (V)
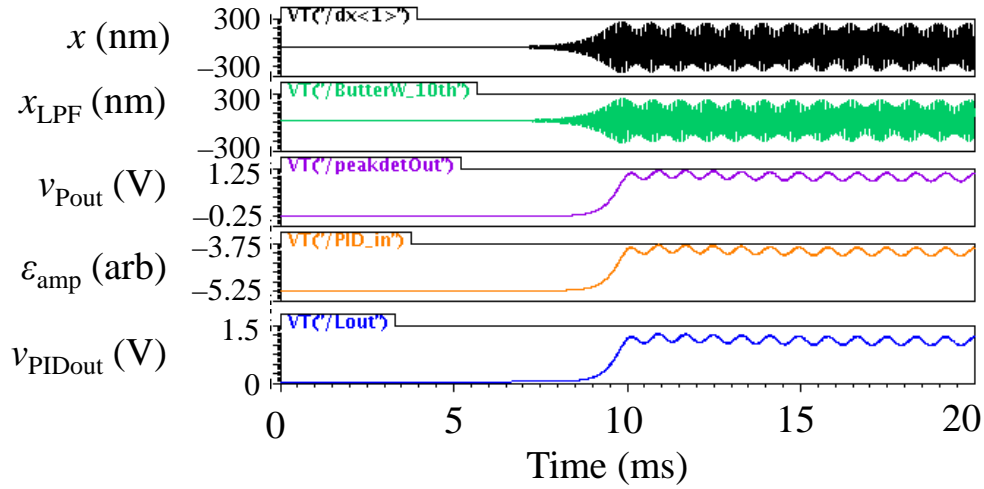
Figure 4-6: Simulation output of the linear analog bifurcation point controller. Buildup of oscillation amplitude occurs at 7.2 ms.

4.2.2. ANALOG PARAMETRIC CONTROLLER

Analog parametric controller observes the statistics of the phase in order to servo at the onset of parametric resonance. At the bifurcation, the state of the system changes according to an escape trajectory. Along this trajectory, the zero-state stability is destroyed and the operation point moves along a slow-time manifold to a stable focus (*i.e.*, an ultimately stable steady-state operation point) of large amplitude. This trajectory is characterized as having three time scales. The fastest time scale is associated with the natural period of the vibration. The second slower time scale is inversely proportional to the damping and represents the collapse onto the slow

Long reset time

98

manifold. The slowest time scale is the time it takes to get to the large-displacement steady-state operation point. This slowest time is required to reset the system from zero displacement "off" state to the non-zero displacement "on" state. The long reset time (on the order of a few seconds) that is required to travel from the zero state to the non-zero state, together with the hysteresis, leads to instability in the controller and must be avoided.

Burgner *et al.* [4] implemented an analog control scheme by observing the variance of the signal phase. The proposed controller is designed such that the resonant amplitude is kept very small (140 pm) in order to lock into the onset of phase coherency to avoid the slow time bifurcation jump event. The separation of the time scales is accomplished by adjusting the parametric drive amplitude to maintain a near-zero state. The controller is impractical for on-chip integration, at least in current technology, since it is implemented in a field-programmable gate array and takes as the input the statistics of the phase. The loop relies on a small stroke, thus low signal-to-noise ratio.

Analog parametric controller

4.2.3. FREQUENCY STATE PARAMETRIC CONTROLLER

The first exploration of an alternative closed-loop bifurcation control scheme is a frequency-state controller, which is schematically shown in Figure 4-7. This topology borrows from a sigma-delta control loop and uses a voltage-to-frequency convertor to convert the voltage control signal into a frequency control signal. The DFF (D-type flip-flop) converts the comparator output into latched digital signal at clock frequency of 80 MHz. The use of the sigma-delta

Controller description

topology takes advantage of its noise shaping capability [41] that contributes to a better signal-to-noise-ratio at the controller output v_0.

Figure 4-7: Schematic view of the sigma-delta frequency-state controller.

The parametric drive voltage amplitude V_{dc} and V_{ac} are fixed. The AC drive frequency, $\omega(t)$, is changed according to the states indicated in Figure 4-8. Two frequency states are chosen such that one of the states (left blue circle) is within the "off" region, having zero steady-state displacement; another state (right blue circle) is in the "on" region, having non-zero steady-state displacement. The switching of the two steady-state frequency states is fast enough in the hope of keeping the servo displacement small and avoiding the buildup of parametric resonance.

Bi-state description

Figure 4-8: Control states of the frequency-state control scheme for an example NIF parametric resonator. The two states are shown as large blue dots.

However, the loop exhibits limit cycling (Figure 4-9) due to the slow time dynamics that are required for the zero state to collapse and move along the bifurcation manifold. This time scale (~0.2 s) is inversely proportional to the quality factor (75.8 in air) of the system. The loop fails due to the limit cycle that destabilizes the servo point. The control parameter is the frequency that is switched between the "on" and "off" regions. However, stepping the frequency from the "off" to the "on" region immediately builds up the displacement amplitude, similar to a quasi-static frequency sweep but with a relatively big frequency step. Thus the amplitude builds up each time when the state is switched to the "on" region.

Loop fails due to limit cycle
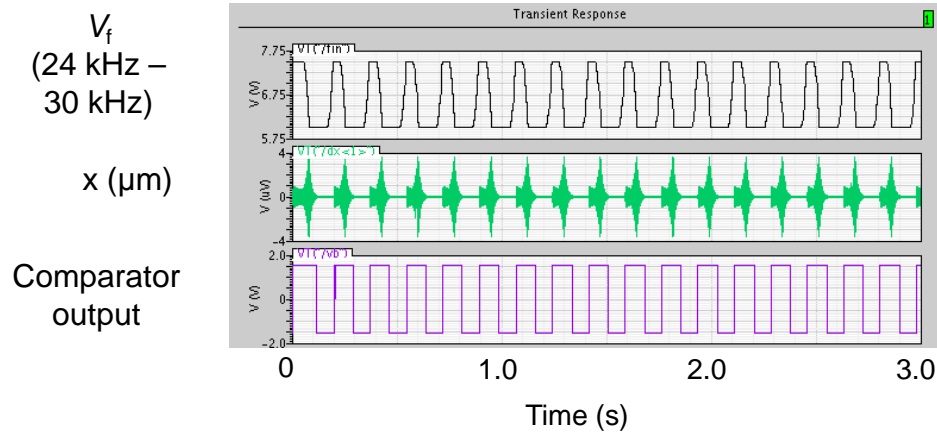
Figure 4-9: Simulation output of a frequency-state controller exhibiting a limit cycle due to the time required to build up oscillation.

4.3.   AMPLITUDE-STATE PARAMETRIC CONTROLLER

Three practical challenges hinder successful control at the parametric bifurcation point. One Challenges challenge is the instability along the bifurcation edge that is demonstrated by the linear analog controller. The second one is the issue of limit cycling caused by the long settling and ring-down time, as shown by the frequency-state controller. Hysteretic behavior inherent in the nonlinear resonators could lead to latch-up instabilities if the operation point travels bi-directionally in quasi-static operation [39].

An amplitude-state controller is proposed to successfully control at the bifurcation jump Drive-state controller general description point. The bi-state controller is capable of servoing along the microelectromechanical parametric resonant bifurcation point at large displacement amplitudes. The feedback states are

102

two levels of the electrostatic-drive polarization voltage that shift the nonlinear resonance characteristics. The system is driven at a fixed frequency and a fixed AC parametric drive. The feedback states correspond to two steady-state conditions: the "on" state experiencing parametric resonance where the amplitude response builds up over time, which is limited to steady-state amplitude by the system nonlinearity; and the "off" state at zero amplitude. The two states correspond to two DC polarization voltage values that are set by the feedback. The states are cycled by 200 kHz pulse width modulation that circumvents the slow hysteretic latch-on that would occur in quasistatic steady-state operation. The exemplary system demonstrated has 1.9 µm servo amplitude with 4.5 Å minimum Allan deviation. The current loop is capable of operating at displacement values of 1.57 µm to 1.95 µm using an adjustable velocity amplitude threshold. Servoing at large displacement amplitude could enhance robustness in the presence of detection noise.

4.3.1. CONTROLLER DESCRIPTION

The block diagram of the control scheme is schematically shown in Figure 4-10. The control plant is the quadratic-shaped-finger comb parametric resonator shown in Figure 3-2 in Chapter 3. The device is made in an in-house SOI-MEMS fabrication process [25] with a 15 µm-thick structural silicon device layer. The electrostatic drive comb finger [Figure 3-2 (c) I] is shaped to create a necessary voltage-controlled linear spring constant γ_1 to excite the parametric resonance. A DC bias voltage V_{dc} is applied to a total of 278 moving straight fingers that are attached to a mass of 9 µg. A variable DC drive voltage, v_{PWM}, in series with an AC excitation voltage, $v_{p,ac}$, is

Controller block diagram

applied on the anchored shaped fingers. Velocity is sensed with a set of 78 linear capacitive comb fingers [Figure 3-2 (c) II] and a pair of transimpedance amplifiers (TIA, labeled A in Figure 4-10) made using an operational amplifier LF356 op-amp (Texas Instruments; Dallas, Texas, USA). Multiplier in Figure 3-4 provides the $2\omega_d$ AC parametric drive.
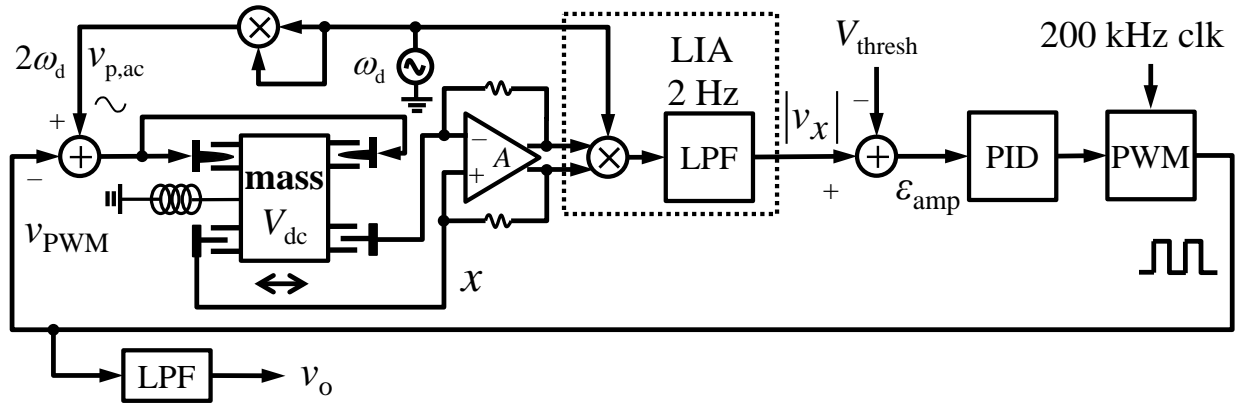
Figure 4-10: Block diagram of the amplitude-state parametric controller.

Using harmonic resonance testbed in Figure 3-15, an ω_r value of 6910.7 Hz was obtained by <u>Detailed loop description</u> a harmonic resonance test immediately before closing the loop. A 3.3 V parametric AC drive voltage is generated by a frequency doubler. With an appropriate $v_{p,dc}$, and a near-twice resonance frequency component $\omega_e = 2\omega_d \approx 2\omega_r$, the resonator operating point is in the proximity of the parametric resonance jump point. The amplitude of the velocity signal, $|v_x|$, is measured by a lock-in amplifier (LIA) that utilizes the drive frequency, ω_d, to demodulate the mechanical resonance signal. The low-pass filter (LPF) attenuates high frequency noise beyond a bandwidth of 3.9 Hz centered on the mechanical resonance at 6910.7 Hz. The velocity amplitude output is compared with a preset threshold $V_{thresh} = 25$ mV, corresponding to 0.076 m/s, to get the error

signal ε_{amp}. This error signal is fed into a proportional-integral-derivative (PID) controller implemented with the HF2LI lock-in amplifier (Zurich Instruments; Zurich, Switzerland) that provides the duty-cycle information to the pulse-width-modulation (PWM) module TL5001 (Texas Instruments; Dallas, Texas, USA). The PWM generates a square waveform with a fixed frequency at 200 kHz. The value of the DC drive voltage is set through the feedback to take two values, constrained by the high and low voltages of the PWM module. These values correspond to two states of operation for the resonator. The DC drive gain switching is set to a speed much faster than the amplitude response dynamics. The PID coefficients are chosen to scale the duty cycle of the "on" state to maintain the desired servo point. The duty-cycle signal (ranging theoretically between 0% to 100%, experimentally ~10% to ~95% with dead zones towards the theoretical maximum and minimum) is an ultra-sensitive indicator of the servo setpoint, therefore it is chosen as the controller output v_o after passing v_{PWM} through another LPF. The parametric DC polarization voltage,

$$v_{p,dc} = V_{dc} + v_{PWM},\hspace{2cm}(4.3)$$

is set by the PWM output, $v_{PWM} = [-1.3, 1.6]$ V, and the DC bias voltage, $V_{dc} = 50$ V, on the mass. The parametric AC drive voltage amplitude, $v_{p,ac}$, is 3.3 V.

4.3.2. PLANT DESCRIPTION

Steady-state frequency response

Sweeping frequency downwards in the open loop, an instantaneous bifurcation "jump" is

seen from a near-zero "off" state (point A) to a non-zero high amplitude (2.2 µm) "on" state

(point B) in Figure 4-11. The bifurcation is caused by multi-valued solutions for one particular frequency, which leads to "bi-stability" in frequency response. Sweeping the frequency upwards, the bifurcation jump happens from a non-zero high amplitude of 8.3 μm (point E) to a near-zero "off" state (point F). The jumps occur at two different bifurcation frequencies depending on the direction of the frequency sweep. This well-known hysteretic behavior [40] is caused by the nonlinearity inherent in the parametric resonator. The applied DC polarization voltage is 50 V and the AC parametric drive voltage is 3.3 V. The tests were carried out in a vacuum of 18 mTorr.
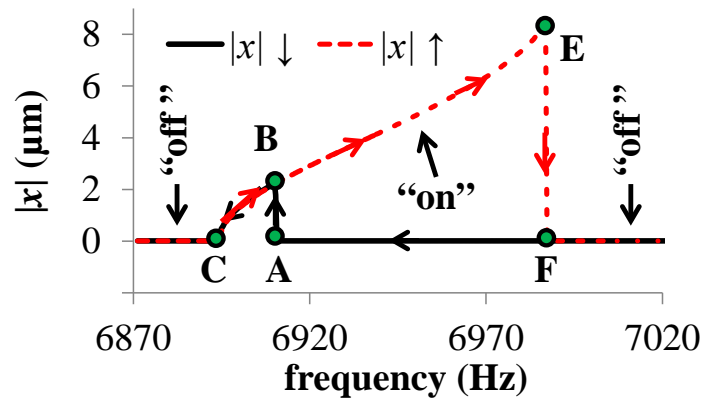
Figure 4-11: Measured steady-state $|x|$ amplitude vs. frequency. The symbols ↑ and ↓ denote the frequency up and down sweeps, respectively. Bifurcations in the response occur at 6987.3 Hz for the up sweep and 6910.7 Hz for the down sweep.

Transient dynamics on the bifurcation edge

The bifurcation jump, though sharp in the steady-state frequency spectrum, is slow in its Time-domain dynamic response [49] compared to the period of the natural oscillation. The time it takes for the transient

bi-stable jump transition also relates to the speed at which a bifurcation parameter changes [49], for example, a mass absorption rate or a parametric frequency sweep rate.
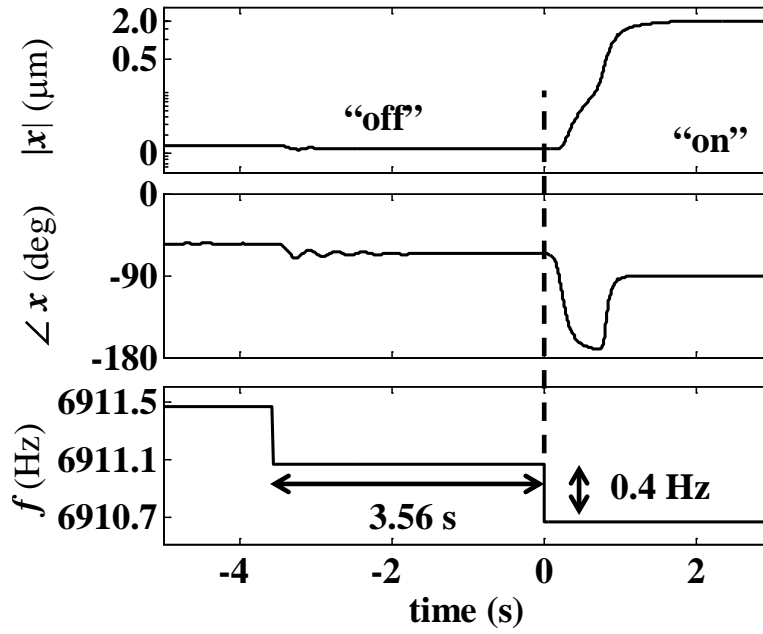
Figure 4-12: Performing frequency down sweep in the time domain, the system experiences instability from the "off" state to reach the "on" state.

Figure 4-12 experimentally shows that the jump experiences a delay after a down-sweep step in the electrical drive frequency. This delay is followed by a monotonic increase in the displacement that lasts for 1.8 s (amplitude increasing region between "off" and "on"). The jump corresponds to the transition from A to B in Figure 4-11. The time it takes for the buildup of the resonance is roughly equal to $Q/f_r = 1.88$ s, where the quality factor $Q = 13000$ and the resonant frequency $f_r = 6910.7$ Hz. This slow time manifold along the system trajectory exhibits "latch-up" instability and sweeping the frequency back up to 6911.1 Hz would increase the amplitude

towards the higher branch (red dotted line to the right of point B in Figure 4-11). This complicates the design of an appropriate nonlinear feedback controller.

4.3.3. PRINCIPLE OF BI-STATE CONTROL
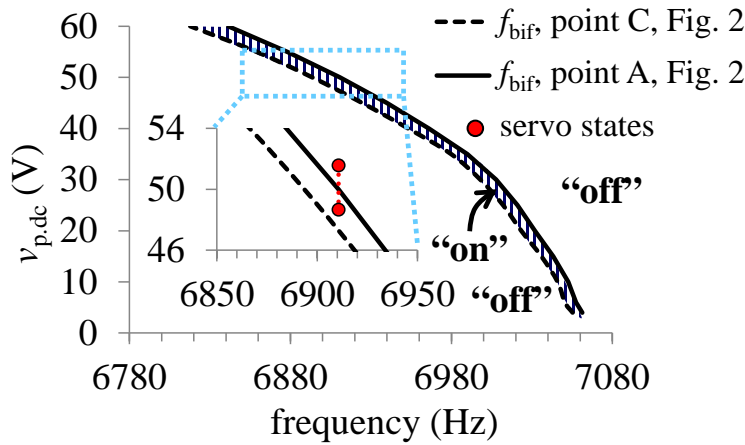
Figure 4-13: Measured bifurcation diagram of the steady-state "on" (shaded) and "off" regions for down-sweep operation. Callout shows two servo states that are marked as circles.

Adjusting the total DC parametric drive voltage, $v_{p,dc}$, that is applied to the resonator comb shifts the entire steady-state frequency response curve (Figure 4-11) in frequency, and as a result, shifts the bifurcation frequency. This effect is quantified in Figure 4-13, which records the loci of the bifurcation frequencies as a function of $v_{p,dc}$ for down-sweep operation. Solid and dashed lines correspond to the bifurcation frequencies at point A and point C in Figure 4-11, respectively. Increasing $v_{p,dc}$ shifts the frequency response curves (Figure 4-11) to the left and decreases the bifurcation jump frequencies. Bifurcation below $v_{p,dc}$ of 3 V is not shown since the

sense signal, which is also proportional to $v_{p,dc}$, is too small. The bifurcation frequency loci plot is used to guide the design of the feedback control loop that aims at servoing on the boundary of pitch-fork bifurcation instability. The "on" state wedge region bends to the left, revealing softening nonlinearity, which is different from Figure 4-3, where stiffening NIF comb is used.

The working principle of the bi-state control is to fix the parametric drive frequency at 6910.7 Hz and the AC drive amplitude $v_{p,ac}$ at 3.3 V, such that the system can be readily moved between states with appropriate values of the DC parametric polarization voltage $v_{p,dc}$. The DC voltage is the feedback signal and constrained to take one of the two values: 48.7 V for the "on" state and 51.6 V for the "off" state. The filled circles in Figure 4-13 indicate these two states.
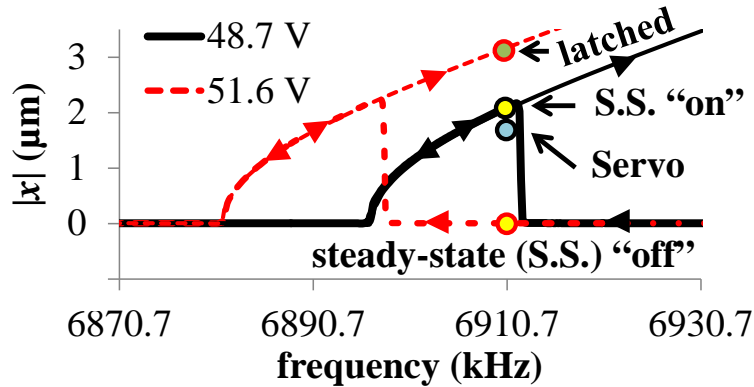
Figure 4-14: Measured steady-state frequency responses for "on" state at 48.7 V and "off" state at 51.6 V. Both states are operated at the same frequency of 6910.7 Hz.

Figure 4-14 provides a view of the servo operating point shown in relation to the steady-state operating curves. Operation at $v_{p,dc} = 48.7$ V has one steady-state operating point indicated as a yellow-filled circle labeled "S.S. "on"". Operation at $v_{p,dc} = 51.6$ V has two viable steady-state

operating points, one indicated as a yellow-filled circle labeled "S.S. "off"" and the other indicated as a green-filled circle labeled "latched". In proper loop operation, the oscillation amplitude never approaches the "latched" state, leading to the labeling of $v_{p,dc} = 51.6$ V operation as the "off" state.

At turn-on, the steady-state operation for $v_{p,dc} = 48.7$ V lands inside the "on" region, thus the displacement builds up towards the steady-state "on" amplitude. However, before the state completely settles to the "on" operating point, a revised value of $v_{p,dc} = 51.6$ V is applied, with steady-state operation residing in the "off" region, moving the state back from "on" towards "off". Immediately at the second cycle of the PWM signal, $v_{p,dc} = 48.7$ V is applied to move the state from steady-state "off" to "on".

State cycling

Due to cycling between states, the frequency of the drive is always operating on the edge of the bifurcation. The servo point, shown as the blue circle, labeled "Servo", in Figure 4-14, is chosen to take a non-zero displacement amplitude of 1.9 µm that is slightly smaller than the maximum "on" steady-state amplitude of 2.2 µm.

Servo point

The choices of the polarization voltage levels, of the servo setpoint and of the timing of the feedback cycling are critical to avoid latch-up conditions. Assume, for example, that the $v_{p,dc} = 48.7$ V state of operation is allowed to settle at the steady-state "on" state before a revised value of $v_{p,dc} = 51.6$ V is applied. Due to inherent hysteresis (demonstrated in experimental observations in the next section), once the feedback voltage switched to 51.6 V the system state would slide to the "latched" state shown as the green-filled circle in Figure 4-14. Since the servo loop then indicates that the system should be turned "off", the feedback would pin to the $v_{p,dc} =$

Latched mode

51.6 V state. This is a failure mode of the servo and can be circumvented by sufficiently fast switching between the "on" and "off" states to avoid settling to a steady-state operating point. The minimum speed of the switching that avoids the latched modes will be determined by characterizing the "recapture" dynamics in the following section.

4.4. CHARACTERIZATION OF THE BI-STATE PARAMETRIC CONTROLLER

4.4.1. OPEN-LOOP RECAPTURE DYNAMICS

In open-loop operation, "recapture" dynamics are illustrated in Figure 4-15. Prior to 0 s, the ‾Description‾ resonator is operated at the steady-state "off" state. A step change of $v_{p,dc}$ from 51.6 V to 48.7 V occurs at $t = 0$ s, starting to drive the displacement towards the steady-state "on". The time
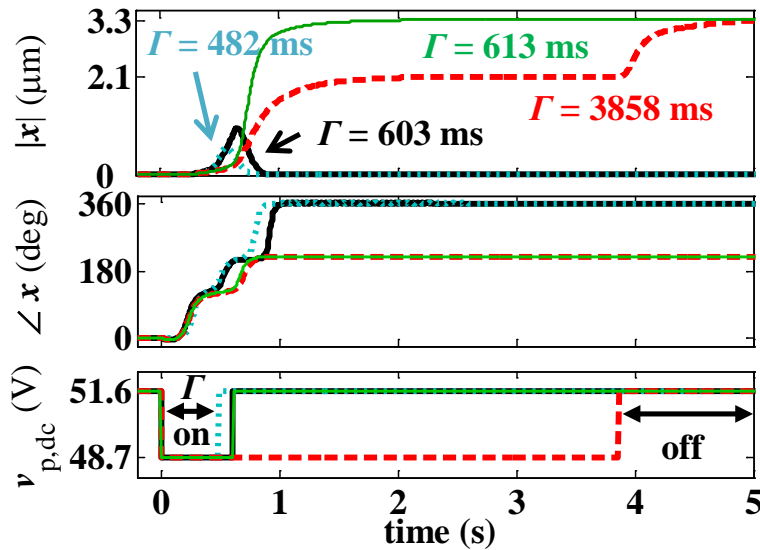
Figure 4-15: Measured step response dynamics by varying the "on" state time.

period during which $v_{p,dc} = 48.7$ V is applied is called the "on-state" time, Γ. After the duration of the "on-state" time, $v_{p,dc}$ is turned back to the 51.6 V, returning to the steady-state "off".

Successful recapturing of the resonator state by switching back to the "off" state is guaranteed provided that Γ is kept shorter than 603 ms. Shorter Γ does not allow the system to reach the steady-state "on" amplitude. The system hysteresis creates a latch-up condition if the on-state time is set beyond this critical time, as evidenced by the $\Gamma = 3858$ ms case. During the long "on-state" time, the displacement settles to a steady-state value of 2.1 μm. At $t = 3.86$ s, a subsequent step change in $v_{p,dc}$ back to the "off" state moves the resonator operation to the high amplitude region in Figure 4-14, on which the "latched" state resides. Thus, in quasi-static operation, it is impossible to fix the servo operation point due to the inherent hysteresis.

In a practical control loop that servos on large amplitude, when backing off from steady-state "on" to "off", before settling at "off", $v_{p,dc}$ is switched back to the "on" state again. The imposition of the bi-state parametric drive voltages with a switching speed (*i.e.*, 200 kHz) that is much faster than the slow amplitude dynamics (on the order of 1 s) sets the servo point. The maximum pulse width that allows the amplitude to back to the "off" state is 603 ms. This sets the minimum bound to the PWM frequency (1.7 Hz). However, at this low PWM frequency, the ripple would be very large.

4.4.2. CLOSED-LOOP DYNAMICS

Turn-on dynamics of this bi-state control loop in a vacuum of 18 mTorr is shown in
Figure 4-16. Prior to enabling the servo, the resonator is turned to the maximum "on" steady-state operating point. The PID controller and PWM are enabled at 23.3 s. The proportional and derivative controller coefficients are $k_p = -141$ and $k_d = -7.1$ s, respectively. The PID coefficients are obtained using the open-loop step response in Figure 4-15 that finds the system's root-locus. The "on" and "off" states are switched back and forth with pulse widths below 5 µs, which is at a much higher speed than the recapture pulses in Figure 4-15. The controlled displacement amplitude backs off from the maximum "on" value and settles at 1.9 µm along the slow time manifold, with only a very small maximum cyclical amplitude variation of 80 pm. The duty cycle "rings" as the servo turns on, and then settles from 0.69 to 0.34.

To demonstrate that a bi-state feedback is needed and a continuous-time linear feedback controller would fail under the same loop condition, turn-on dynamics of the bi-state feedback loop (labeled as "PWM" in black) are overlaid with that of the continuous-time feedback (labeled as "No PWM" in red). The continuous-time linear analog controller is formed with the same schematic in Figure 4-10 except removing the PWM module. The absence of the PWM module requires the PID coefficients to be scaled by the PWM gain to emulate the exact loop condition as that of the bi-state controller. The PWM output is $v_{PWM} = [-1.3, 1.6]$ V and its input is $[-0.7, 1.3]$ V, thus the PWM gain is 4.8. As a result, the PID coefficients for an equivalent continuous-time controller are $k_p = -679$ and $k_d = -34$ s. The PID output voltage v_{PID} is revised to $[-1.3, 1.6]$ V to match the bi-state controller PWM output. All other loop parameters remain

unchanged. The hypothesis is that the slow time amplitude build up is so fast that a continuous-time $v_{p,dc}$ control will not servo and instead the latch-up phenomenon in Figure 4-14 occurs. The use of the bi-state switching is one approach to reset the amplitude build-up. This is implemented by stepping the voltage to drive the system state to the steady-state "off" region when a latch-up scenario would otherwise occur.
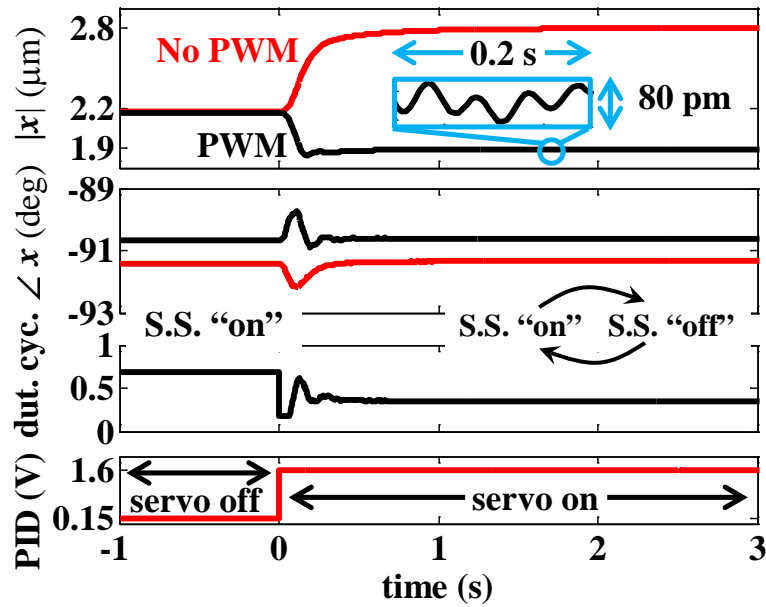
Figure 4-16: Measured turn-on transients of the PWM bi-state controller (black) overlaid with those of an equivalent continuous-time linear analog controller (red).

Successful operation of the bi-state controller is demonstrated by the variation of the loop parameters such as but not limited to the threshold voltage, the mass change, and the PID coefficients. A closed-loop step response is shown in Figure 4-17 illustrating the effect of the

Shifts in servo setpoint

derivative controller coefficient. The symbol $|x|$ in the plot refers to the output voltage from the lock-in amplifier low-pass filter. The servo is active throughout the duration of the measurement. The servo threshold, V_{thresh}, is changed at 0 s from 25 mV to 28 mV. With $k_p = -141$ and $k_d = 0$ s, the displacement amplitude changes from 1.89 µm (equivalent to 27 mV)
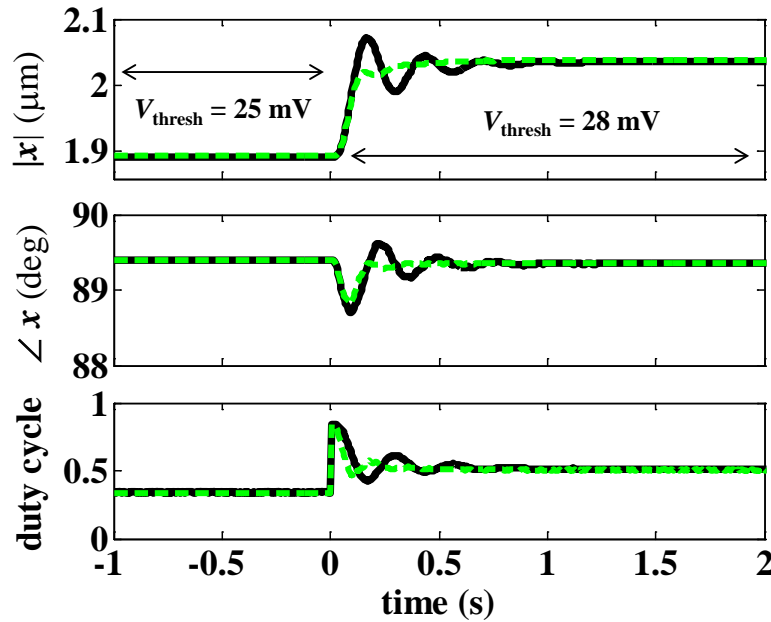
Figure 4-17: Shifts in the servo setpoint illustrating closed-loop dynamics. Solid curves are obtained with only proportional control and the dashed curves are obtained using proportional-derivative control.

to 2.04 µm (29 mV) with a significant amount of ringing (solid line). This ringing is alleviated by introducing a derivative control coefficient, $k_d = -7.1$ s, which results in a near critically damped amplitude response (dashed line).

4.4.3. ALLAN DEVIATION AND SYSTEM SENSITIVITY

Allan standard deviation of the controller duty-cycle output, shown in Figure 4-18, represents Measurement condition and Allan deviation

the servo-point variation versus the integration time. The test was initiated after the pressure had

reached a constant value of 18 mTorr and continuously ran for 18 hr. The signal is sampled at

14.1 samples per second. The duty-cycle signal is compensated to eliminate the effect of

temperature on the bifurcation frequency variation and hence the servo setpoint. The average

temperature throughout the duration of the measurement is 26.2 °C.

Figure 4-18: Allan deviation plot of the controller duty cycle output quantifying the stability.

The loop operates at a large displacement value of 1.9 µm. The minimum detectable duty Minimum Allan deviation

cycle is 2.36×10^{-4} at an integration time of 4.3 s. The calculation of the system sensitivity is

obtained by varying the DC polarization voltage, V_{dc}, from 50.4 V to 47.8 V while keeping all

other loop parameters (*e.g.*, PID coefficients and PWM levels) the same. The values of the duty

cycle and the servo displacement are recorded. The two $v_{p,dc}$ voltage values corresponding to the "on" and "off" states change from 49.1 V and 52.0 V for V_{dc} = 50.4 V, to 46.5 V and 49.4 V for V_{dc} = 47.8 V. The loop breaks down outside this range. Varying the DC polarization voltage V_{dc} requires the feedback control loop to change the PWM duty cycle so as to keep the servo stable. As a result, duty cycle variation also changes the servo displacement amplitude. The measured servo displacement amplitude is plotted against the duty cycle in Figure 4-19. The minimum Allan deviation of the duty cycle corresponds to 1.9 μm × 2.36×10^{-4} × 0.441 = 2 Å resolution in the displacement amplitude |x| for the bandwidth of 0.2 Hz.
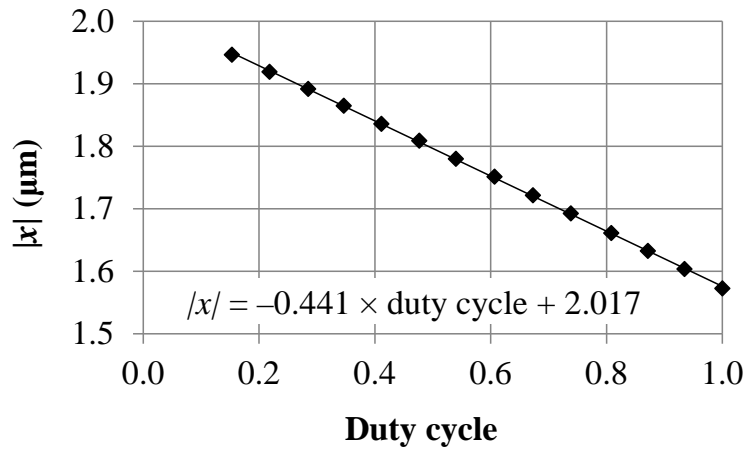
Figure 4-19: Measured displacement amplitude, |x|, versus the duty cycle variation.

The negative slope of –1/2 prior to τ = 4.3 s is caused by thermal amplitude noise that may be Sources of noise dominated by the electronics noise from the TIA gain impedance, PWM pull-up resistor, and the frequency doubler circuit. The current noise from the TIA is

$$\sqrt{\frac{i_{\text{n,motional}}^2}{\Delta f}} = \sqrt{\frac{4k_B T}{R_{\text{TIA}}}} , \qquad (4.4)$$

where k_B is the Boltzmann's constant, $T = 299.2$ K is the temperature, and R_{TIA} is the resistance value of the TIA, which is 1 MΩ in this design. To relate the TIA current noise to the input-referred displacement noise, the motional current is

$$i_{\text{motional}} = V_{\text{dc}} \left| \frac{dC}{dt} \right| = V_{\text{dc}} \frac{C_0 \omega}{L_{\text{sense}}} |x| , \qquad (4.5)$$

where $C_0 = 8.1 \times 10^{-14}$ F is the total capacitance of the 78 straight finger sense comb capacitor, and $L_{\text{sense}} = 15.7$ μm is the overlapped length of the sense combs. The input-referred displacement noise is

$$\sqrt{\frac{|x|_{\text{n}}^2}{\Delta f}} = \sqrt{\frac{4k_B T}{R_{\text{TIA}}}} \frac{L_{\text{sense}}}{V_{\text{dc}} C_0 \omega} , \qquad (4.6)$$

which evaluates to 11.5 pm/rtHz. The differential readout is implemented with a pair of TIAs, thus giving rise to a combined noise displacement of 16.3 pm/rtHz. TL5001 PWM module (Texas Instruments; Dallas, Texas, USA) uses an external pull-up resistor [47] of 3.4 kΩ to set the output voltage levels due to the open-collector output design. The pull-up resistor gives rise to the noise in the $v_{\text{p,dc}}$ DC voltage levels. The frequency doubler circuit in Figure 3-4 also contributes voltage noise to the parametric AC drive. Aside from the circuit noise, the Brownian noise of the mechanical resonator in the vacuum of 18 mTorr is 1.4 fm/rtHz, which is much smaller than the TIA input-referred noise. Figure 4-20 shows the overlaid plot of the thermal noise (blue line) corresponding to the 16.3 pm/rtHz TIA noise by converting from the noise displacement to the equivalent noise duty cycle of 1.9×10^{-5} (rtHz)$^{-1}$. The green line is the

thermal noise fit of the Allan deviation plot. The measured thermal noise corresponds to a noise duty cycle of 3.6×10^{-4} at 1 Hz bandwidth. The discrepancy shows the possibility of other dominating noise sources that will need to be identified.
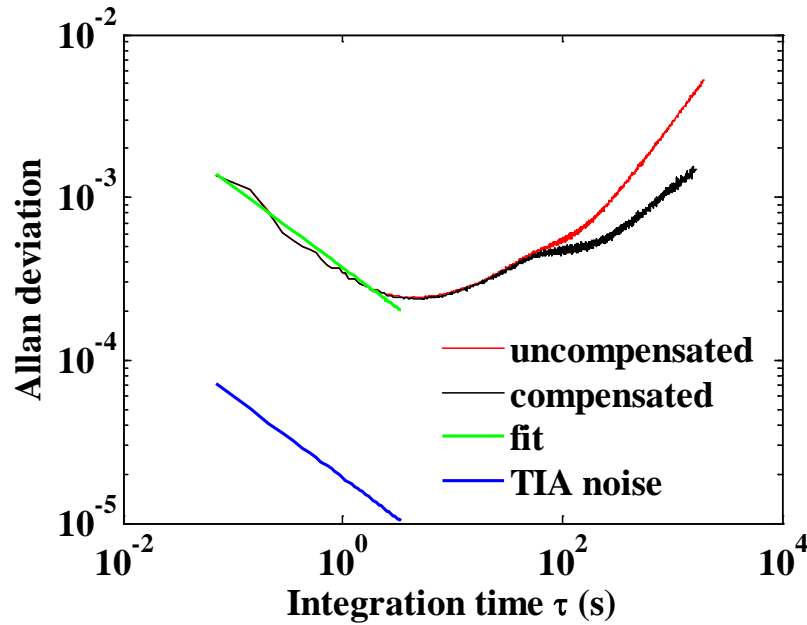
Figure 4-20: Allan deviation plot overlaid with the TIA noise. The green line is the fit of the thermal amplitude noise to the measured Allan deviation.

High frequency noise is attenuated by the 4th-order 3.9 Hz bandwidth low-pass filter of the lock-in amplifier. Random-walk frequency noise dominates beyond $\tau = 4.3$ s. Drift in the servo point limits the minimum detectable signal.

Equivalent minimum detectable frequency shift and the equivalent mass sensitivity are calculated based on the measured system sensitivity values. Frequency variation is linked to the duty cycle by computing the sensitivity

Calculation of minimum detectable frequency

$$S \equiv \frac{\delta D}{\delta f_{11}} = \frac{\delta D / \delta V_{dc}}{\delta f_{11} / \delta V_{dc}} , \tag{4.7}$$

where D is short for the duty cycle and f_{11} is the corresponding mechanical "pitch-fork" bifurcation frequency. The numerator is obtained by the slope ($-0.32\ \mathrm{V}^{-1}$) of the duty cycle versus the DC polarization voltage shown in Figure 4-21. The denominator is obtained using the bifurcation frequency expression in (1.25):

$$\frac{\delta f_{11}}{\delta V_{dc}} = f_{r0}\left(1 - \frac{\gamma_1 V_{ac}^2}{4k_1}\right)\left[1 + \frac{\gamma_1 (V_{dc} + v_{PWM})^2}{k_1}\right]^{-\frac{1}{2}} \times \frac{\gamma_1 (V_{dc} + v_{PWM})}{k_1} , \tag{4.8}$$
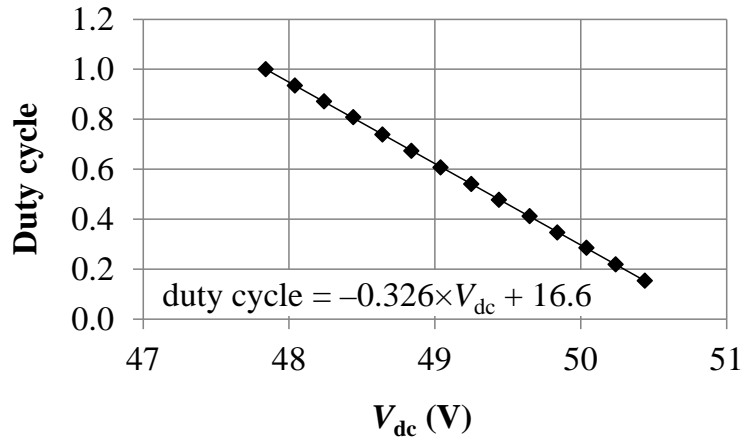
Figure 4-21: Measured duty cycle variation versus the DC polarization voltage, V_{dc}.

which evaluates to $-6.17\ \mathrm{Hz/V}$. Thus the sensitivity value is $S = 0.053\ \mathrm{Hz}^{-1}$. The minimum detectable frequency corresponding to the minimum duty cycle Allan deviation of 2.36×10^{-4} is $\sigma_{f_{11},\min} = 4.5\ \mathrm{mHz}$.

The normalized equivalent minimum detectable mass variation is calculated using the [Equivalent minimum mass variation]

minimum equivalent frequency Allan deviation $\sigma_{f_{11},\min}$

$$\frac{\mathrm{d}m_{\min}}{m} = \frac{\sigma_{m,\min}}{m} = 2\frac{\sigma_{f_{11},\min}}{f_r}, \tag{4.9}$$

which evaluates to –1.3ppm. The total mass of the parametric resonator is 9 µg, leading to an equivalent absolute mass variation of 12 pg.

4.4.4. DRIVE AMPLITUDE TO NOISE RATIO

Calculated in the above section, the example bi-state parametric controller has an equivalent [Definition]

2 Å Allan deviation in the displacement amplitude $|x|$ for the bandwidth of 0.2 Hz, which relates

to the signal resolution. Defining the ratio of steady-state drive amplitude to the system noise

(the "ratio") as the figure of merit, we yield a figure of merit that is used to compare with other

devices. The large servo displacement of 1.9 µm yields a ratio of drive amplitude to the system

noise of $20 \times \log(1.9 \times 10^{-6} / 2 \times 10^{-10}) = 80$ dB, a value that is much larger compared with the

analog bifurcation control scheme [4] where the steady-state amplitude is 140 pm and the noise

floor is 0.6 pm, leading to a "ratio" of 47 dB.

In open-loop operation, the control plant – a shaped-finger comb parametric resonator has a ["Ratio" of the shaped-finger comb]

steady-state amplitude of 8 µm and a minimum detectable displacement on the order of 5 pm.

The use of the shaped comb to excite parametric resonance boosts the "ratio" to 124 dB.

Whereas for a non-intergiditated finger comb parametric resonator discussed by DeMartini

in [12] and by Guo in [16], the amplitude is constrained to a stroke of 1.0 ~ 1.25 μm. The "ratio" for such comb designs is limited to 106 dB.

The ratio of steady-state drive amplitude to the system noise could be used to evaluate Conclusion parametric resonant systems and are linked to the signal-to-noise ratio (SNR) of a sensor that uses parametric resonator as the sensing element. Higher steady-state drive amplitude yields a more robust signal in the presence of injected detection noise. Smaller systematic noise contributes to better sensor resolution. The ratio of the steady-state drive amplitude to the system noise could be used as a comparable metric to evaluate mechanical systems that are potentially useful in the sensing applications.

(end)

CHAPTER 5   BI-STATE CONTROL OF A DUFFING RESONATOR ON THE FALLING EDGE OF THE INSTABILITY

A s another validation example towards the investigation of a control technique capable of servoing on the bifurcation setpoint, an electrostatically-driven Duffing microresonator, fabricated in the SOI-MEMS process, was chosen as the control plant. Mechanical nonlinearity inherent in the Duffing resonator gives rise to a sharp jump in oscillation amplitude at the bifurcation and is, therefore, ideal for further validation of the bi-state amplitude control approach. Without substantial contribution from electrical nonlinearity, the presence of only one mechanical nonlinearity component from the spring suspension underlines its reduced complexity.

Bifurcation-based detectors provide an ultrasensitive approach to reveal parametric small changes in bifurcation frequency if a control approach is designed to servo at the bifurcation point. However, a system exhibiting bifurcation behavior is difficult to control due to the long settling and ring-down time [49], hysteresis [16]-[17], and the instability [39] as described in Section 4.3 of Chapter 4. This chapter describes a bi-state servo of a MEMS Duffing resonator that lands on the maximum amplitude "on" point prior to the bifurcation jump event, which leads to a significantly higher controlled amplitude (*e.g.*, 4.8 µm) compared to prior works [4] and [26]. Open-loop and classic linear control approaches fail near the maximum amplitude "on"

point due to the hysteretic behavior of the resonance. An alternative approach to the closed-loop control of Duffing resonance is realized through tracking the phase [50], which is beyond the scope of this thesis.

5.1.   DUFFING RESONANCE

5.1.1.   CRAB-LEG RESONATOR DESIGN
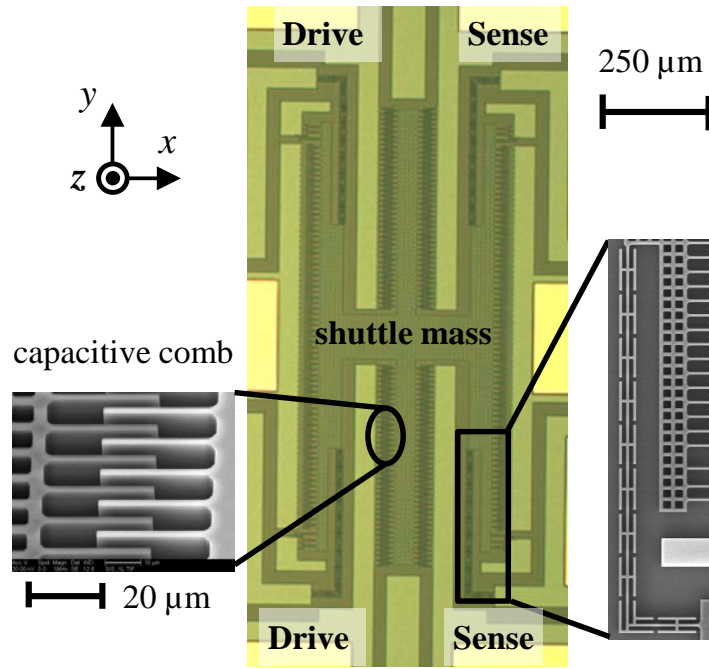
Figure 5-1: Optical microscope image of the Duffing microresonator with zoomed-in SEM views of the drive comb and the crab-leg spring.

Shown in Figure 5-1 is the 15 µm-thick SOI-MEMS Duffing resonator reported in [25] as the Device control plant, with a perspective view of the lateral capacitive comb electrode geometry. The H-

shaped perforated shuttle mass is symmetrically suspended by four crab-leg springs. The nonlinearity inherent in the system is dominated by the mechanical crab-leg suspension nonlinearity because of the absence of electrostatic spring constants from the constant-force straight-finger capacitive comb drive.

The capacitive combs are symmetrically placed on both sides of the shuttle mass; the left set Testbed serves as the electrostatic drive and the right set serves as the capacitive sense electrode, as shown in Figure 5-2. The use of laterally-moving linear displacement sensing comb promotes large-displacement Duffing response. The design parameters and geometric constants are summarized in Table 5-1.
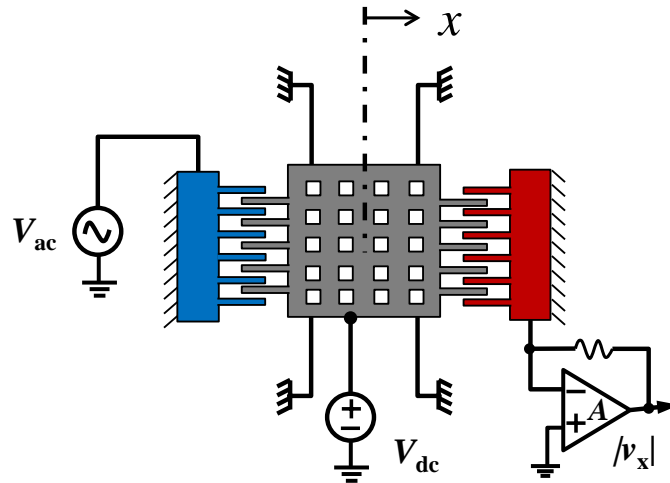
Figure 5-2: Duffing resonance testbed schematic.

Table 5-1: Crab-leg resonator design parameters

Symbol	Parameter	Value
m	total mass	5.8 μg
b	damping coefficient	1.3×10^{-6} kg/s
k_1	linear mechanical spring constant	3.8 N/m
k_3	cubic mechanical spring constant	4.3×10^{9} N/m^3
L_{ov}	overlapped comb finger gap	15.7 μm
N	number of rotor fingers	78
g	comb finger gap	3.5 μm
t	device thickness	13.2 μm
f_{res}	natural frequency	4124 Hz
V_{dc}	DC polarization voltage	10 V
V_{ac}	AC drive voltage	25 mV

5.1.2. DUFFING EQUATION

The governing equation for the crab-leg resonator is

$$ m\ddot{x} + b\dot{x} + k_1 x + k_3 x^3 = F\cos(\omega t), \tag{5.1} $$

where x is the displacement of the resonator, m is the mass, b is the damping coefficient, k_1 and k_3 are the linear and cubic mechanical spring constants, F is the magnitude of the electrostatic force, ω is the frequency of the applied force which is around the natural resonance of the system. The crab-leg spring provides the k_3 nonlinearity that leads to the Duffing effect [15]. The electrostatic force $F\cos(\omega t)$ is exerted through the straight finger comb, where the AC force magnitude F is

$$ F = \frac{C}{L_{ov}} V_{dc} V_{ac}, \tag{5.2} $$

126

and where L_{ov} is the overlapped length of the capacitive comb, and V_{dc} and V_{ac} are the DC and AC voltage magnitudes applied on the comb (Figure 5-2). Total capacitance of the straight finger drive comb is

$$C = \frac{2N\varepsilon_0 L_{ov} t}{g}, \qquad (5.3)$$

where N is the number of rotor fingers, t is the thickness of the device, and g is the comb finger gap. In contrast with the parametric drive force in (1.1), the harmonic force $F\cos(\omega t)$ is a function of time t but not a function of x. F equals 0.26 nN using (5.2) and the design values in Table 5-1.

The nonlinearity inherent in the resonator gives rise to the analytic Duffing response curves shown in Figure 5-3. For a linear harmonic resonator, the resonance peak centers at its natural resonant frequency (dashed line). However, using the same resonator topology, adding mechanical nonlinearity k_3 bends the resonance peak (solid line). The amount of bending is determined by the value of the k_3 nonlinearity. Larger k_3 results in more bending. This bending leads to multi-valued solutions for one frequency value around the resonance and thus the bifurcation phenomenon (dotted line). The inherent nonlinearity also leads to a hysteresis effect: the loci of the bifurcation depend on the direction of the frequency sweep.

Analytic Duffing response
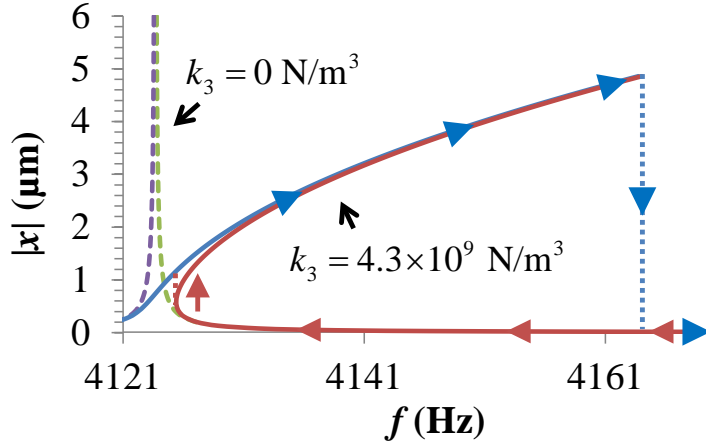
Figure 5-3: Analytic Duffing response, overlaid with linear harmonic response, using the design parameters in Table 5-1. Arrows indicate the direction of the frequency sweep.

5.1.3. STEADY-STATE FREQUENCY RESPONSE

Typical measured frequency response of the Duffing resonator is plotted in Figure 5-4. The $\overline{\text{Measured}}$ Duffing crab-leg resonator is driven harmonically around its natural resonance at $f_{\text{res}} = 4124$ Hz. The $\overline{\text{response}}$

quality factor of the system is 14250 at 28 mTorr when tested inside a custom vacuum chamber, as shown in Figure 3-17. The polarization voltage on the moving shuttle mass is $V_{\text{dc}} = 10$ V and the AC sinusoidal drive on the lateral capacitive comb rotor is $V_{\text{ac}} = 25$ mV. The test is performed in a vacuum of 25 mTorr. The frequency response bends towards right, indicative of hardening nonlinearity. On the edge of the bent peak (point B), a jump in the resonance amplitude from 4.8 µm to 0 µm occurs. The frequency at which the instantaneous jump occurs is called the "bifurcation frequency" f_{B}, which equals 4167 Hz for the setpoint B in Figure 5-4. For a reverse frequency sweep, the jump happens at a lower frequency of 4125 Hz from 0 µm to

1.0 μm (point A), evidencing the hysteresis effect. To the right of point B, the resonance amplitude reduces to a small but non-zero value.
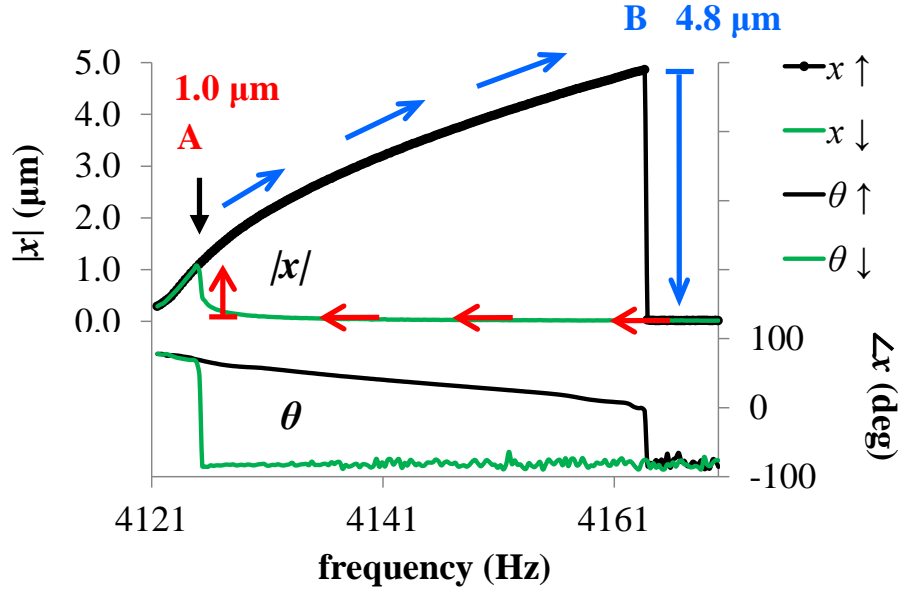
Figure 5-4: Frequency response of the Duffing resonator at V_{dc} = 10 V and V_{ac} = 25 mV. ↑ symbolizes the frequency up-sweep; ↓ is the frequency down-sweep.

Shown in Figure 5-5, decreasing the AC drive voltage, V_{ac}, decreases the up-sweep bifurcation frequency. The frequency bi-directional sweep tests are performed in vacuum of 26 mTorr. The drive voltage magnitudes are 10 V DC and 6 mV AC for both sweep directions. Bifurcation jumps are observed at 4126 Hz and 4124 Hz for up- and down- frequency sweeps, respectively.
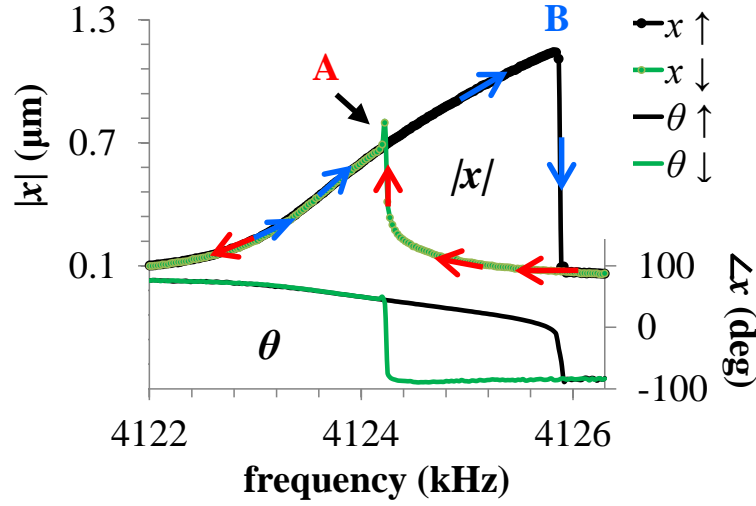
Figure 5-5: Frequency response of the Duffing resonator at $V_{dc} = 10$ V and $V_{ac} = 6$ mV.

5.1.4. FREQUENCY SWEEP TRANSIENT

A time-domain frequency chirp test is performed to explore the transient on the edge of the instability. The frequency is swept up through the bifurcation frequency ($f_B = 4167$ Hz). The initial swept frequency is backed off from the bifurcation frequency f_B so the jump can be observed. As the frequency approaches f_B, the oscillation amplitude drops from 4.8 µm to a very small displacement. The displacement of 1.8 µm seen in the "off" state of Figure 5-6 corresponds to a small voltage output (3.0 mV) from the capacitive pick-off circuit (*A* in Figure 5-2), which is due to the feedthrough from the V_{ac} drive to the capacitive sense comb. The feedthrough mainly couples through the low resistive silicon substrate. The single-ended capacitive readout in Figure 5-2 lacks the ability in matching and cancelling out the feedthrough.

Time-domain turn-off transient
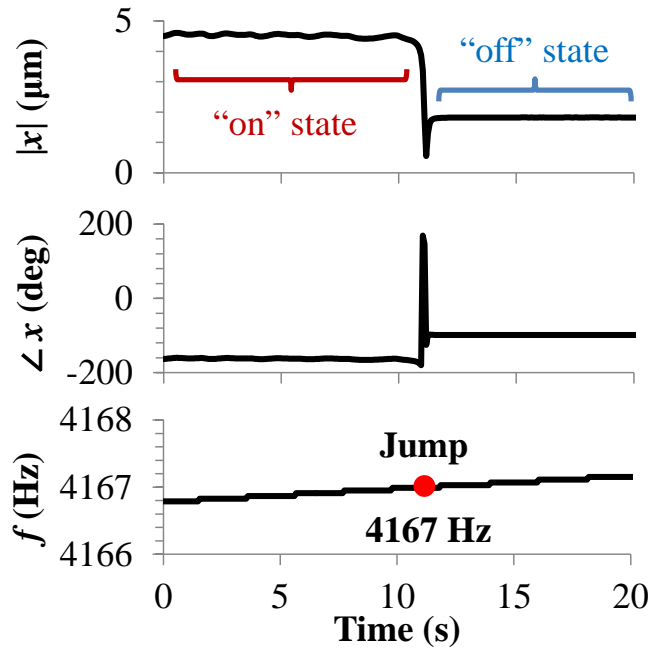
Figure 5-6: Turn-off transient of the Duffing resonator. The resonator is turned off when the frequency is swept beyond the bifurcation frequency at 4167 Hz.

5.2. CONTROLLER DESIGN

Duffing resonance featuring bifurcation behavior is capable of gauging small resonance Motivation changes. These variations in the resonator characteristics are generally modified by the resonant mass or suspension spring stiffness. By probing the shifts in the bifurcation point through the use of a feedback control loop, sensitive gravimetric and stress detectors can be built.

5.2.1. LOCI OF BIFURCATION FREQUENCIES

Adjusting the AC drive voltage V_{ac} shifts the entire frequency response curve in Figure 5-4, Loci of bifurcation

thus resulting in changes in the bifurcation points A and B, as evidenced by Figure 5-7. The

shifts in up-sweep bifurcation frequency (analogous to point B in Figure 5-4) are graphically

represented in Figure 5-8, which records the loci of the amplitude jump points as a function of

V_{ac}. The upper plot is the up-sweep steady-state frequency response for a particular voltage drive

gain $V_{ac1} = 25$ mV, and the green dot on the lower plot records the bifurcation frequency point

for V_{ac1}. The process of varying V_{ac} and recording the corresponding bifurcation frequency

values builds the bifurcation diagram ($V_{ac} - f$ curve) of the location of the falling edge of the

instability. The DC voltage is fixed at 10 V.
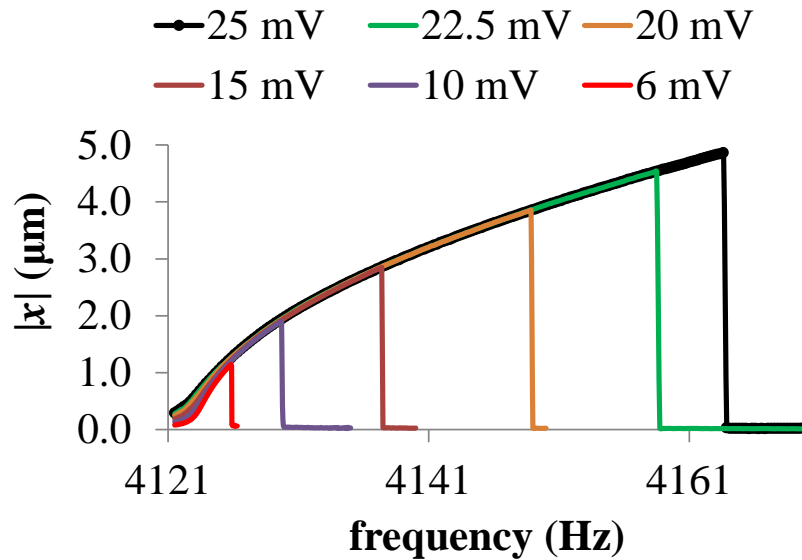
Figure 5-7: Measured up frequency sweep responses for different V_{ac} values. The 25 mV and

6 mV cases correspond to Figure 5-4 and Figure 5-5, respectively.
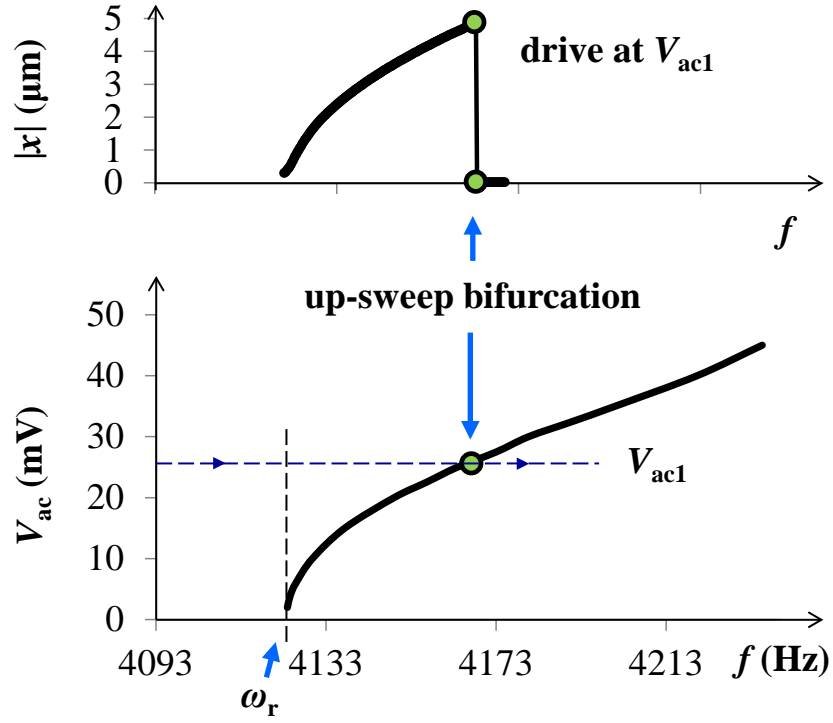
Figure 5-8: Measured loci of the up-sweep bifurcation frequency. ω_r is the linear resonance frequency. The DC voltage is fixed at 10 V.

Changes in the DC and AC drive voltage magnitudes modify the system's effective spring constant, which affects the bending of the resonance curve, the amplitude of the resonance, and the frequency regions where the system experiences Duffing resonance. In a typical nonlinear resonator, the AC drive voltage, V_{ac}, and the DC polarization voltage, V_{dc}, shape the bifurcation diagram. Varying V_{ac} shifts the frequency response ($|x| - f$) curve, which leads to the bending of the $V_{ac} - f$ curve. The up-sweep bifurcation frequency as a function of drive voltage is

Analytic bifurcation frequency

$$\omega_{\text{bifurcation}} = \omega_r \left(1 + 0.86 \frac{\sqrt[3]{k_3}}{k_1} \left(\frac{C}{L_{\text{ov}}} V_{\text{dc}} V_{\text{ac}} \right)^{2/3} \right),$$ (5.4)

where ω_r is the resonant frequency. Higher V_{ac} increases the frequency of the bifurcation.

5.2.2. CONTROLLER PRINCIPLE

The filled circles in Figure 5-9 identify the states for a bi-state control loop. Two states – the Principle of operation high and low displacement states are associated with high and low V_{ac}, respectively. The high displacement state ("on" state) driven by 25.6 mV is to the left of the $V_{\text{ac}} - f$ curve which has a 5 µm steady-state amplitude response; the low displacement state ("off" state) driven by 24.1 mV is to the right of the $V_{\text{ac}} - f$ curve, representing a low but non-zero steady-state amplitude response (on the order of 20 nm). The two states center around $V_{\text{ac}} = 25$ mV and have the same fixed frequency at the bifurcation frequency $f_{\text{B}} = 4167$ Hz for the $V_{\text{ac}} = 25$ mV setpoint. The DC polarization voltage is kept at 10 V. The two states are set through design of the AC drive gain and land on opposite sides of the bifurcation point. The measured frequency response on the upper plot shows a large bifurcation frequency shift for a relatively small V_{ac} shift. Due to the small difference in V_{ac}, the two frequency response curves prior to the jump seem overlapped but the red curve corresponding to the high V_{ac} is slightly higher in displacement than that of the low V_{ac} (black curve).

Figure 5-9: Controller principle of the bi-state Duffing servo. The high and low displacement states are associated with high and low V_{ac}, respectively.

5.2.3. CONTROLLER DESCRIPTION

The control loop is schematically shown in Figure 5-10. The control setpoint of the loop is 0.2 μm below point B in Figure 5-4. The AC drive frequency (f_B = 4167 Hz) and the DC polarization voltage (V_{dc} = 10 V) are fixed to values such that the system can be moved between large-displacement "on" and low-displacement "off" states in Figure 5-9 with appropriate bi-state values of AC amplitude V_{ac}. The Duffing resonator is driven by V_{ac} whose amplitude and frequency are set by the pulse-width-modulator (PWM) output and the lock-in amplifier (LIA),

Controller schematic

135

respectively. A transimpedance amplifier (labeled A) followed by the LIA picks off the resonator velocity amplitude $|v_x|$. The loop tracks $|v_x|$ to a fixed setpoint, $V_{thresh} = 8.1$ mV, corresponding to 0.132 m/s and to 5 μm displacement amplitude. The error output is fed into a proportional-integral-derivative (PID) controller to generate the input signal to the PWM representing the pulse-train duty cycle. Through a gain stage, the output of the PWM provides the two voltage levels [9.92, 9.34] V for an intermediate voltage $V_{ac,m}$, which, multiplied by $V_{ac,i}$ = 25.8 mV and divided by 10 (set by the multiplier module shown in Figure 3-4), sets the AC drive amplitude V_{ac} of [25.6, 24.1] mV through an analog multiplier AD633 (Analog Devices; Norwood, MA).

The voltage V_{ac} is controlled by the feedback and rapidly switches between the "on" and PWM two states "off" states at 300 kHz to achieve the servo at the maximum "on" point without turning off the resonator. This switching is graphically represented by alternating the "on" state (green circle) and the "off" state (red circle) in Figure 5-9. The fast switching avoids the long ring-down transient needed to settle from the maximum displacement to the zero displacement. This resettling time is inversely proportional to the air damping and is on the order of 1 s for the resonator operated under a vacuum of 22 mTorr. The speed of switching is determined by characterizing the "recapture" dynamics in the following section.
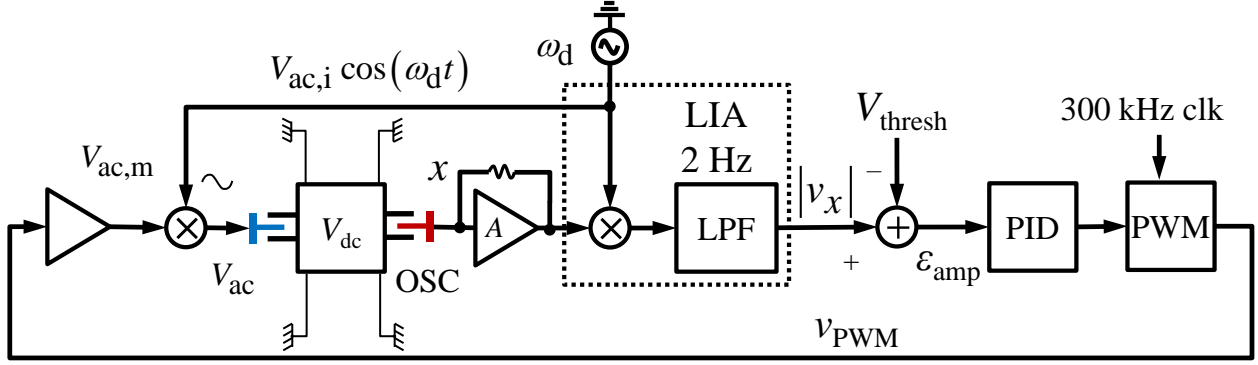
Figure 5-10: Block diagram of the bi-state Duffing controller with a crab-leg resonator in Figure 5-1 as the plant.

5.3. CONTROLLER CHARACETERIZATION

5.3.1. OPEN-LOOP RECAPTURE DYNAMICS

A time-domain open-loop analysis of the dynamics on the edge of the bifurcation jump provides information on how fast the controller should switch between two states to guarantee successful recapturing of the steady-state "on" state. These "on" state recapture dynamics are characterized in Figure 5-11. In the open-loop operation, prior to 0 s, the resonator is operated at the steady-state maximum displacement "on" state. At 0 s, a step change in V_{ac} is introduced from 25.6 mV to 24.1 mV, at which voltage the resonator is not fully in the steady-state low displacement "off" state but rather just starting to turn off. V_{ac} is then turned to 25.6 mV, driving back to the steady-state "on", after a prescribed amount of time Γ, called the "off" state time, Γ.

137

When Γ is less than 394.6 ms, the Duffing resonance is successfully recaptured as presented
by the red curves in Figure 5-11. When Γ is larger than 395.0 ms, the resonance degenerates to
the "off" state, even though V_{ac} drives the system back to the steady-state "on" at $t = \Gamma$. This is
shown as the black curves in Figure 5-11, where the Duffing resonance is turned-off by
increasing the off-state time to $\Gamma = 550.6$ ms. The critical off-state time Γ at which the
resonance is on the edge of being recaptured is 394.6 ms. A shorter Γ of 340 ms (thin blue
curves) is overlaid with the 394.6 ms case to show a faster recovery and less ringing.
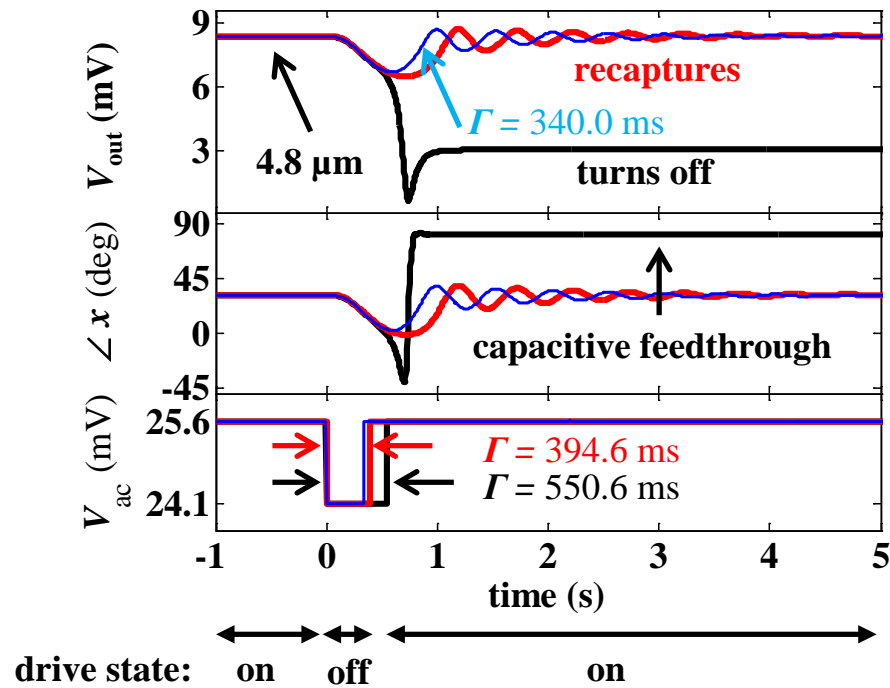
Figure 5-11: Measured step response dynamics by varying the "off" state time Γ. Successful
recapture (red curves) of the Duffing resonance is guaranteed by rapidly switching back to the
"on" state.

After $t = 0$, the resonator starts to turn off and provides the initial condition for later step turn-on at $t = \Gamma$, when the system exhibits a step response due to the step turn-on in the drive amplitude V_{ac}. The black and red curves are the same prior to $t = 394.6$ ms and starts to deviate afterwards. For the black curve, between 394.6 ms and 550.6 ms, the displacement experiences a steep decrease in the displacement amplitude. The recapture is impossible after the "collapse" of the "on" state. Beyond $t = 550.6$ ms, capacitive feedthrough from the drive voltage dominates, as evidenced by the phase value of almost 90°.

The recapture dynamics in Figure 5-11 gauge the "slow time" (*i.e.,* time scale that is much longer than the resonance period) behavior of the plant and provides information on the speed of switching for a practical controller. Depending on the length of Γ, the system can either recover from the decreased amplitude (red curves in Figure 5-11) for a small Γ or completely turns off (black curves in Figure 5-11) for a large Γ. The closed-loop bi-state signal in Figure 5-10 has an "off" state pulse width of less than 3.3 µs, which is much shorter than the critical Γ of 394.6 ms to avoid the latch-off scenario.

5.3.2. CLOSED-LOOP TURN-ON TRANSIENTS

Figure 5-12 is the turn-on transient of the closed-loop controller with an initial approaching phase. During region (1), the resonator is off, and the phase is incoherent. In region (2), an AC voltage $V_{ac} = 25$ mV is applied to the resonator drive fingers at 15 s, with a frequency of 4123 Hz. Due to the capacitive feedthrough, the turn-on in V_{ac} results in a step response in the displacement signal output to a non-zero value of 3 mV (equivalent to a displacement of

1.8 µm). The choice of the initial frequency ensures the resonator is within its "off" region and to the left of bifurcation point A in Figure 5-4 so as to build up resonance from a zero displacement. Region (3) is the necessary "approach" process when the resonator is turned on to the steady-state maximum displacement operation point (point B in Figure 5-4) by increasing the drive frequency from 4123 Hz to 4167 Hz, just before the bifurcation jump. The PID controller
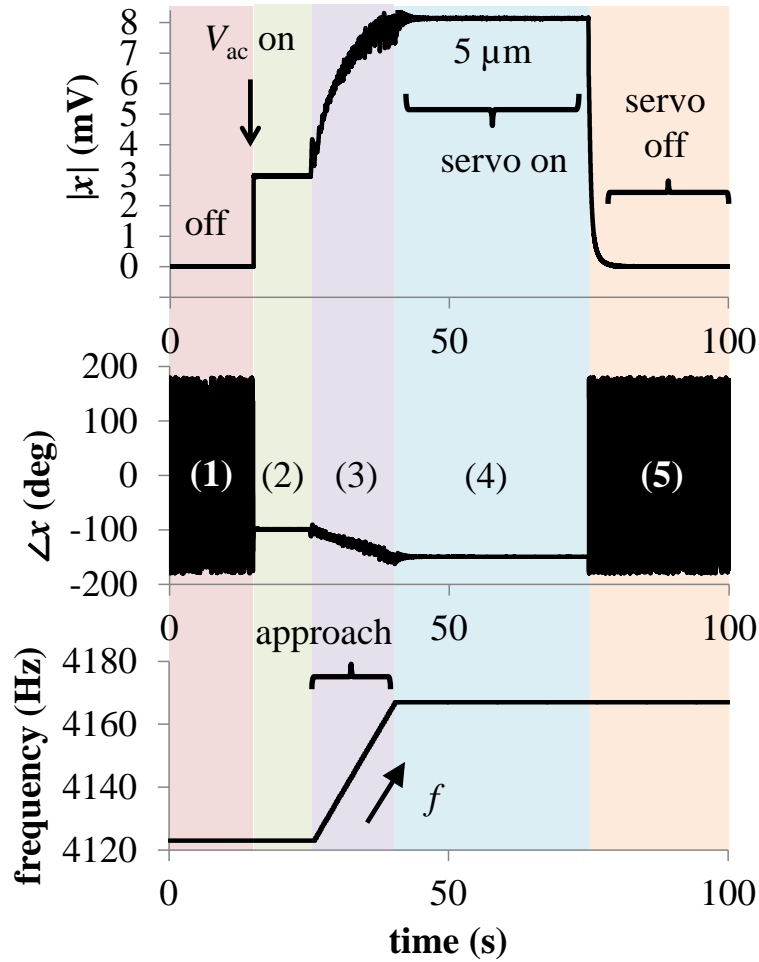
Figure 5-12: Turn-on transient of the bi-state Duffing controller.

threshold V_{thresh} is set in (4) after reaching this maximum operation point, turning on the servo. The PWM output voltage, v_{PWM}, switches at 300 kHz, with its duty cycle centered on 0.5. The amplitude during the servo is maintained at 5 µm. At 75 s in region (5), the servo is disabled by turning off V_{ac}. The phase is well-defined during the time the controller is on and loses track of the input V_{ac} when the controller is turned off.

5.3.3. ALLAN DEVIATION
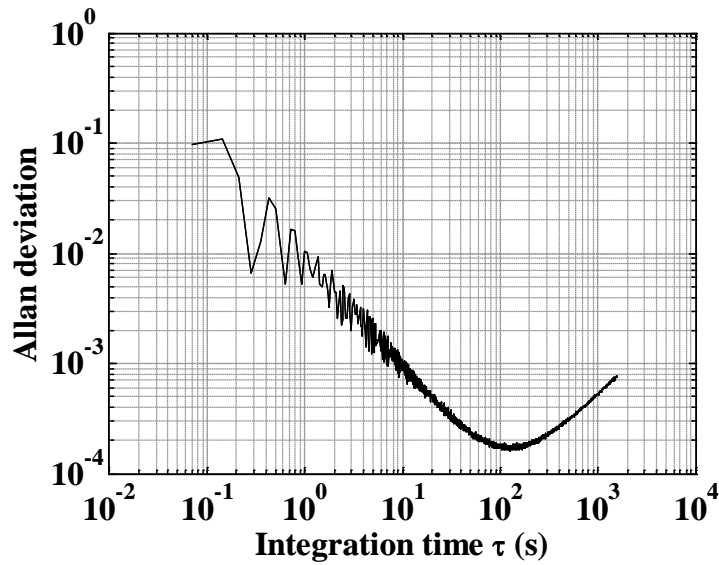
Figure 5-13: Allan deviation plot of the normalized velocity amplitude quantifying the stability.

The Allan deviation of the normalized velocity amplitude $|v_x|$ is plotted in Figure 5-13 quantifying the stability of the loop. The control system output is sampled at 14.1 Hz for 13.5 hr. The test was initiated after the vacuum level had reached 19 mTorr and was maintained at

Measured
Allan
deviation

19 mTorr throughout the test. The output is normalized to the steady-state amplitude of 4.8 μm. The minimum Allan deviation is 1.59×10^{-4}, corresponding to a minimum detectable displacement of 5 μm $\times$ 1.59×10^{-4} = 0.76 nm at the integration time of 127 s. As a comparison, for the parametric controller, the minimum detectable duty cycle is 2.36×10^{-4} at an integration time of 4.3 s, leading to 0.2 nm resolution in $|x|$ for the bandwidth of 0.2 Hz.

The Allan deviation at small integration time shows a $1/\tau$ dependence, which is related to the white phase noise. The Allan deviation in Figure 5-13 measures the duty cycle stability, which varies with the oscillation amplitude. The $1/\tau$ dependence suggests a direct relationship between the amplitude and frequency fluctuation in the Duffing resonator. This may be partially explained by the frequency response of the Duffing equation. The amplitude, x, and the frequency, $\omega_{\text{bifurcation}}$, at the Duffing bifurcation are related by (derived from [15]) $\boxed{\text{Discussion}}$

$$\omega_{\text{bifurcation}} = \omega_r \left(1 + \frac{3}{8} \frac{k_3 x_0^2}{m \omega_r^2} x^2 \right), \tag{5.5}$$

where ω_r is the resonance frequency and x_0 is the spatial period of the comb. Further investigation is slated to investigate the nature of noise for small integration time.

(end)

CHAPTER 6   CONCLUSIONS AND FUTURE WORK

6.1.   CONCLUSIONS

A resonator is said to be excited parametrically when the state of the system is modified by time-varying parameters.   In an electrostatically-driven resonant micromechanical system, the main design parameters are the supporting flexure stiffness and the equivalent electrostatic stiffness.   The electrostatic stiffness is set by nonlinear capacitive geometry and excitation voltage amplitude. By selecting appropriate nonlinear parametric settings, the principal parametric resonance mode is excited around twice of the system's natural resonance frequency.   The nonlinear parametric resonance features a sharp transition at the bifurcation point on the boundary of instability, making it a good candidate for highly sensitive mass (*i.e.*, gravimetric) and stress sensing.

Parametric resonance

MEMS parametric resonance provides significant advantages over its simple harmonic resonance (SHR) alternatives, but these advantages come with a complex analytic model.   The governing nonlinear Mathieu equation of the class of resonator under investigation is a second-order differential equation with an oscillating external excitation, whose closed-form solution including all nonlinear effects and damping is not possible to solve analytically.   Perturbation theory [15] provides a mathematical approach to an estimated solution.   In particular, the method of averaging was employed in [17] and [18] with normalized dimensionless parameters to arrive

Perturbation analysis

at the steady-state frequency response and the nonlinear stability analysis around parametric resonance. For most values of parametric drive frequency, the system is not stimulated and the solution is a very small bounded oscillation that is close to $x = 0$. With a parametric drive frequency at or near twice the resonant frequency, parametric resonance is established, which builds oscillation amplitude that would grow without bound if not for the damping and the inherent nonlinearity in the system. The exact combinations of the parametric drive frequency, the parametric drive amplitude, and the DC polarization voltage that cause this parametric amplification effect depend on the values of the system parameters.

The accurate design of nonlinear systems including simultaneous effects from nonlinearities, Behavioral modeling damping, and parametric stimulus is of particular interest. One of many design approaches is through behavioral modeling and simulation, as previously demonstrated by [16], [17], and [40]. To enable modeling of complex nonlinearity inherent in the system, behavioral modeling is employed with lumped models of explicit governing ordinary differential equations and macro models with characteristics extracted from finite element analysis (FEA). The nonlinear parametric micromechanical resonators discussed in this work are modeled using primitives from a MEMS behavioral model library [32]. The behavioral models are coded in Verilog-A and the composable MEMS schematic [17] is simulated in Cadence Spectre. The enabling capability of this methodology in modeling electromechanical actuators [46] and sensors facilitate the modeling in environments that emulate end applications. The behavioral modeling of the control possibilities helped in exploring the system design space and obtaining a high-stroke robust controller setting.

Nonlinearity inherent in electrostatically-actuated MEMS arises from several different **Parametric excitation** electromechanical drive topologies. One simple example is a laterally-moving parallel-plate capacitor able to provide large softening nonlinearity for a sufficiently small gap. To deliver a well-designed nonlinearity, past research made use of the symmetric fringing field generated between the non-interdigitated comb fingers (NIF) [16], [17], and [18]. In this case, the fingers do not overlap. Both the linear and nonlinear electrostatic stiffness can be independently tuned by alignment and percentage of finger width to the pitch [19].

Exciting parametric resonance through a NIF comb exhibits a small stroke due to the **Shaped comb** necessary parametric nonlinearity from the fringing fields that only extends to a displacement equal to $\pm 1/2$ of the comb pitch. However, resonant sensors such as gravimetric sensors, stress sensors and gyroscopes that have superior sensitivity require actuation schemes capable of a large motional stroke. For a laterally-moving comb, nonlinearly varying the comb gap profile generates a custom-shaped force-engagement response [22]. A tailored custom profile "shaped-finger comb" utilizes a nonlinearly varying electrode gap to provide the required effective spring stiffness for parametric resonance. The shaped-finger comb moves along the direction of the fingers (*i.e.*, lateral movement), allowing sufficient clearance for large resonant displacement. The possibility of using a large-stroke shaped-finger comb in exciting the parametric mode was briefly mentioned in a prior paper [22] but no further work was done. This work examines the large-stroke parametric resonance using this class of shaped-finger comb and explores the design parameter space of the shaped-finger comb to obtain the optimum finger shape considering the fabrication constraints. The quadratic-shaped-finger comb resonator, when used as the controller

plant, provides the capability for large amplitude servo operation. Linear displacement sense-comb capacitors were included to electronically measure the parametric resonance in these large-stroke systems to experimentally study the time-domain transients of the bifurcation and the dynamics when the polarization or AC parametric voltages change. These transient studies enable rapid verification of the analytical parametric response regions and the study of system root locus for later optimization of controller parameters.

Three practical challenges hinder successful control at the parametric or Duffing bifurcation point. One challenge is the jump along the bifurcation edge that destroys the servo of a linear analog controller. The second one is the issue of limit cycling, as shown by the failure of a frequency state controller. Another known challenge is the hysteretic behavior inherent in the nonlinear resonators, which leads to a latch-up scenario if the operation point travels bi-directionally in quasi-static operation. The design and implementation of a bi-state drive-amplitude bifurcation-point closed-loop control scheme is our first step in developing an understanding of control of the oscillation amplitude that tracks the bifurcation setpoint.

This work validates control at the bifurcation instability point for a MEMS quadratic-shaped-finger comb parametric resonator using a bi-state amplitude switching methodology. Through pulse-width-modulation (PWM) fine-grained control, the DC polarization voltage amplitude is only allowed to take one of the two possible steady-state values (one non-zero "on" state, and the other zero "off" state). The bi-state amplitude servo interplays with the system dynamics that enables the control at the bifurcation without the limit cycling and the latch-up failures. The "on" and "off" states are pulsed at 200 kHz that is much faster than the slow amplitude response and

circumvents the latch-on condition that would happen in quasistatic operation. The minimum PWM frequency is set by the open-loop recapture dynamics that explore the system's transients when experiencing a step change in the DC polarization voltage. Lower PWM frequency results in longer pulse width and larger ringing, which lead to less stable duty cycle output. The control scheme is a building block for ultra-sensitive platforms for detecting parameter changes that give rise to resonance frequency (and thus bifurcation frequency) shifts. The potential of the controller in achieving high ratio of steady-state drive amplitude to the system noise could eventually link to a high signal-to-noise ratio parametric sensor with an excellent precision.

Another validation example builds a bi-state servo that operates on the falling edge of the <u>Bi-state Duffing control</u> microelectromechanical Duffing resonant bifurcation setpoint. The loci of the Duffing bifurcation are recorded as a function of AC drive gain. Two control states are set through the AC drive gain near the locus of the bifurcation while operating at a fixed drive frequency and a fixed DC polarization voltage. One of the system states experiences resonance at the maximum amplitude whereas the second state has a small but non-zero amplitude motion. The amplitude servo point is chosen at the maximum "on" amplitude prior to the jump event. The states are cycled by the PWM that is set much faster than the amplitude response dynamics and inhibits the system from latching off as would happen in static operation. The bi-state amplitude control for the Duffing resonator is done through switching the AC parametric drive voltage values. This is different than the DC polarization voltage switching in the parametric controller. It is possible to employ the bi-state control scheme to vary other system parameters to control the amplitude

gain. This exploration may lead to other parametric gain control mechanisms and inspire new parametric excitation schemes.

6.2. FUTURE WORK

The bifurcation jump setpoint is inherently a sensitive indicator of the mass and spring constant of micromechanical devices. The detection of this sharp bifurcation jump promises a robust sensing mechanism. The capability to servo on the edge of the instability promotes future implementation of an ultrasensitive bifurcation-based mass (*i.e.*, gravimetric) or stress (strain) detector.

Future applications

The example bi-state parametric controller in this work is experimentally validated to achieve sensitive detection of resonant frequency shifts down to millihertz range, limited by the electronics noise of the sense circuitry and the feedback control loop. The equivalent normalized minimum detectable mass change is –1.3ppm if the controller were to form the core of a future mass sensor. Redesigning the device to a smaller mass would further reduce the current minimum detectable mass variation of 12 pg toward creating an ultrasensitive gravimetric sensor. Making the moving plate mass smaller would reduce the available layout area for placing the drive comb fingers. Increasing the drive comb fingers would also reduce the number of sense comb fingers given a fixed layout area. One would need to explore the design space to find the optimum combination of the mass area and comb finger number to maximize the normalized mass sensitivity.

Equivalent mass sensing capability

The current SOI-MEMS shaped-finger comb parametric resonator has a relatively large finger gap limited by lithography, lowering obtainable linear electrostatic spring constant. In current designs, the effect of air damping is large enough to require a significantly large actuation voltage. The minimum drive voltage to excite the onset of the parametric amplitude buildup is a function of the air damping. With current technology and characterization environment, significant air damping requires a high parametric excitation voltage. To avoid possible electric breakdown, the devices were tested in the vacuum environment. However, the operation in air is necessary for making a useful gravimetric sensor. Future work is slated to run the device in atmosphere pressure with a necessary larger voltage drive to excite parametric resonance. Such tests in air would be used to compare the minimum detectable mass variation with the current results in the vacuum. The parametric drive is ideally zero with zero displacement. Thus larger air damping would give rise to more noise displacement that perturbs the operation point sufficiently away from zero. With a correct drive voltage setting, the automatic parametric resonance may be excited with a low voltage in air. Alternative approaches towards a gravimetric sensor include but are not limited to the implementation of the shaped-finger comb resonator in the CMOS-MEMS [36] fabrication technology. Benefiting from finer line-width and the flexibility of electrical routing, by designing smaller electrode gaps to obtain larger drive ability, one can reduce the maximum voltage required to excite parametric resonance in air. The bi-state control scheme serves as the foundation for the future monolithic-chip implementation of the control electronics with the on-chip MEMS nonlinear resonators to make a robust single-chip bifurcation-based gravimetric or chemical sensor suite.

The potential stress sensing capability of the bi-state control technique is exemplified by the use of a parametric resonator with fixed-fixed beam suspensions, as shown in Figure 6-1. The fixed-fixed beam provides mechanical stiffening nonlinearity that modifies the linear spring constant of the system in x when its anchors experience an applied stress in y. The modified spring constant shifts the location of the parametric bifurcation, which can be tracked precisely by the bi-state control technology developed in this work. The device had been implemented in the latest SOI-MEMS run, and will be used as the plant of the bi-state control loop that forms the core of a future parametric stress sensor.
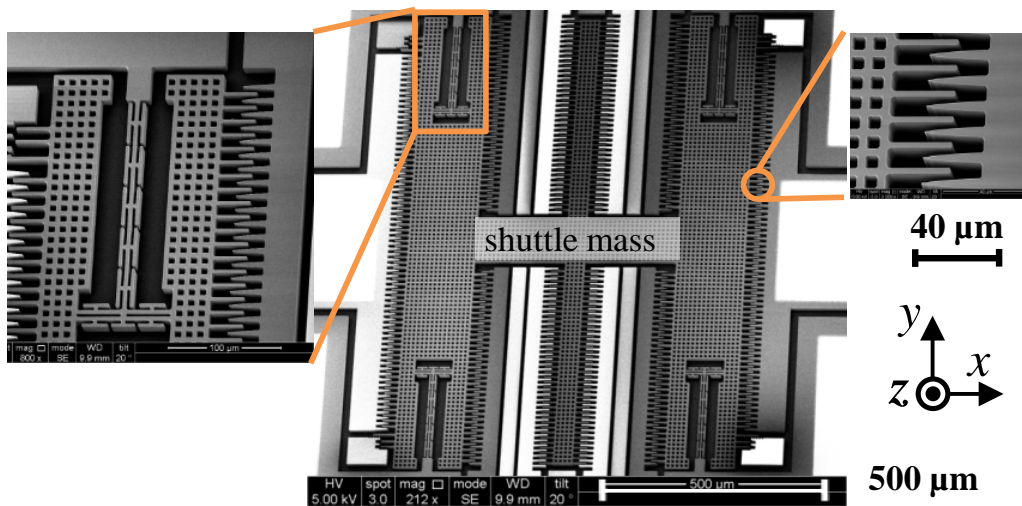
Figure 6-1: SEM of a parametric resonator suspended by four sets of fixed-fixed flexures to be used in the bi-state control loop that makes a stress sensor.

The use of the shaped-finger comb is our first demonstration of the large displacement parametric response for relatively small parametric excitation voltages. Further modification of

the finger shapes could potentially result in future low power automatic electrostatic parametric excitation schemes.

(end)

APPENDIX A   NONLINEAR MATHIEU EQUATION

T his chapter presents details on the perturbation solution of the nonlinear Mathieu equation. It explains the derivation of "slow" equations of amplitude and phase, followed by a coordinate transformation of the Jacobian matrix used to examine the stability of each solution branch. In deriving the "averaged" equation, a general procedure called "nondimensionalization" is used to evaluate the relative magnitude of multiple parameters in a system and discard the parameters that are of little importance. The choice of the normalized dimensionless parameters affects the final form of the estimated solution.

A.1.   NONDIMENSIONALIZATION

The relative order of magnitude of the parameters in an equation can be used to decide whether solutions are strongly affected by a certain group of parameters. Normalization is a technique which compares the dimensional system parameters with basic system characteristics to yield comparable dimensionless quantities. These dimensionless quantities allow measurements of relative importance when comparing their order of magnitude. The dimensional analysis is applied such that all variables are made dimensionless so the equation can be universally applied.

To apply the nondimensionalization technique, the nonlinear Mathieu equation (1.11) is rewritten in the form

Dimensional Mathieu equation

$$\tilde{m}\ddot{\tilde{x}} + \tilde{b}\dot{\tilde{x}} + \tilde{k}_1\tilde{x} + \tilde{k}_3\tilde{x}^3 + \left(\tilde{\gamma}_1\tilde{x} + \tilde{\gamma}_3\tilde{x}^3\right)\left[V_{dc}^2 + V_{ac}^2\cos(\tilde{\omega}_d\tilde{t})\right] = 0. \tag{A.1}$$

where dimensional constants, x, m, b, k_1, k_3, γ_1, γ_3, ω, and t, in (1.11) are replaced by the same variable with tilde in (A.1). Tildes are associated with dimensional variables (except voltage, capacitance, force, and device dimensions).

The dimensionless displacement is

$$x = \frac{\tilde{x}}{\tilde{x}_0} \tag{A.2a}$$

where $\tilde{x}_o$ is the characteristic displacement. For example, $\tilde{x}_o$ may be the electrostatic comb finger pitch (center-to-center distance between fingers) for a non-interdigitated finger resonator (Chapter 2), or the maximum stroke of a lateral comb resonator.

The dimensionless time is

$$t = \frac{\tilde{\omega}\tilde{t}}{2} \tag{A.2b}$$

where $\tilde{\omega}$ is the electric excitation frequency. Dividing (A.1) by mass $\tilde{m}$ and rearranging terms yields:

$$\ddot{\tilde{x}} + \frac{\tilde{b}}{\tilde{m}}\dot{\tilde{x}} + \tilde{x}\left[\frac{(\tilde{k}_1 + \tilde{\gamma}_1 V_{dc}^2)}{\tilde{m}} + \frac{\tilde{\gamma}_1 V_{ac}^2\cos(\tilde{\omega}\tilde{t})}{\tilde{m}}\right] + \tilde{x}^3\left[\frac{(\tilde{k}_3 + \tilde{\gamma}_3 V_{dc}^2)}{\tilde{m}} + \frac{\tilde{\gamma}_3 V_{ac}^2\cos(\tilde{\omega}\tilde{t})}{\tilde{m}}\right] = 0. \tag{A.3}$$

The first and second derivatives are found from the chain rule:

$$\dot{\tilde{x}} = \frac{d\tilde{x}}{d\tilde{t}} = \frac{d\tilde{x}}{dt}\frac{dt}{d\tilde{t}} = \frac{\tilde{\omega}}{2}\frac{d\tilde{x}}{dt} = \frac{\tilde{\omega}}{2}\frac{d\tilde{x}}{dx}\frac{dx}{dt} = \frac{\tilde{\omega}}{2}\tilde{x}_0\frac{dx}{dt} = \frac{\tilde{\omega}}{2}\tilde{x}_0\dot{x} \tag{A.4}$$

$$\ddot{\tilde{x}} = \frac{d^2\tilde{x}}{d\tilde{t}^2} = \frac{d}{d\tilde{t}}\left(\frac{d\tilde{x}}{dt}\frac{dt}{d\tilde{t}}\right) = \frac{\tilde{\omega}}{2}\frac{d}{d\tilde{t}}\left(\frac{dx}{dt}\frac{d\tilde{x}}{dx}\right) = \frac{\tilde{\omega}}{2}\tilde{x}_0\frac{d}{dt}\left(\frac{dx}{dt}\frac{dt}{d\tilde{t}}\right) = \frac{\tilde{\omega}^2}{4}\tilde{x}_0\frac{d^2x}{dt^2} = \frac{\tilde{\omega}^2}{4}\tilde{x}_0\ddot{x} \tag{A.5}$$

153

where

$$\dot{x} \triangleq \frac{dx}{dt} \qquad (A.6)$$

Combining (A.2), (A.4), and (A.5) into (A.3) produces the normalized equation,

$$\ddot{x} + \frac{2\tilde{b}}{\tilde{m}\tilde{\omega}}\dot{x} + x\left[\frac{4(\tilde{k}_1 + \tilde{\gamma}_1 V_{dc}^2)}{\tilde{m}\tilde{\omega}^2} + \frac{4\tilde{\gamma}_1 V_{ac}^2 \cos(2t)}{\tilde{m}\tilde{\omega}^2}\right] + x^3 \tilde{x}_o^2 \left[\frac{4(\tilde{k}_3 + \tilde{\gamma}_3 V_{dc}^2)}{\tilde{m}\tilde{\omega}^2} + \frac{4\tilde{\gamma}_3 V_{ac}^2 \cos(2t)}{\tilde{m}\tilde{\omega}^2}\right] = 0. \quad (A.7)$$

Written in a dimensionless form, the normalized version of (A.1) is

$$\ddot{x} + \varepsilon\, b\dot{x} + x(\delta + 2\varepsilon \cos 2t) + \varepsilon\, x^3 (\delta_3 + \gamma_3 \cos 2t) = 0 \qquad (A.8)$$

where the dimensionless parameters are defined in (A.9). The dimensionless damping, b, is

$$b = \frac{2\tilde{b}}{\varepsilon\, \tilde{m}\tilde{\omega}}. \qquad (A.9a)$$

The dimensionless linear mechanical stiffness, δ, is

$$\delta = \frac{4(\tilde{k}_1 + \tilde{\gamma}_1 V_{dc}^2)}{\tilde{m}\tilde{\omega}^2}. \qquad (A.9b)$$

The dimensionless parametric linear electromechanical stiffness, ε, is

$$\varepsilon = \frac{2\tilde{\gamma}_1 V_{ac}^2}{\tilde{m}\tilde{\omega}^2}. \qquad (A.9c)$$

The dimensionless cubic mechanical stiffness, δ_3, is

$$\delta_3 = \frac{2(\tilde{k}_3 + \tilde{\gamma}_3 V_{dc}^2)\tilde{x}_0^2}{\tilde{\gamma}_1 V_{ac}^2}. \qquad (A.9d)$$

The dimensionless parametric cubic electromechanical stiffness, γ_3, is

$$\gamma_3 = \frac{2\tilde{\gamma}_3 \tilde{x}_0^2}{\tilde{\gamma}_1}. \tag{A.9e}$$

The magnitude of these dimensionless parameters represents their relative importance.

In parametric resonance, the electrical drive frequency is around twice the resonant frequency $2\tilde{\omega}_r$. Substituting (1.12) and $\tilde{\omega} = 2\tilde{\omega}_r$ into (A.9d) gives $\delta = 1$. Similarly, Substituting (1.12) and $\tilde{\omega} = 2\tilde{\omega}_r$ into (A.9c) yields

$$\varepsilon = \frac{\tilde{\gamma}_1 V_{ac}^2}{2\left(\tilde{k}_1 + \tilde{\gamma}_1 V_{dc}^2\right)} \tag{A.10}$$

Assuming $\tilde{\gamma}_1 V_{ac}^2 \ll \tilde{k}_1$ and $\tilde{\gamma}_1 V_{dc}^2 \ll \tilde{k}_1$, the dimensionless perturbation parameter $\varepsilon \ll 1$. Perturbation theory is used to find solutions around this setpoint $\delta = 1$ and $\varepsilon = 0$. When ε approaches zero, (A.8) becomes

$$\ddot{x} + \delta\, x = 0. \tag{A.11}$$

The system is a harmonic oscillator with a normalized frequency, ω, given by

$$\omega^2 = \delta. \tag{A.12}$$

where $\delta = 1$. Thus,

$$\omega = \sqrt{\delta} = 1. \tag{A.13}$$

When $\varepsilon \neq 0$ but small, we assume that the frequency of (A.8) is still given by (A.12) but with a frequency that is perturbed away from 1. This method is called the variation of parameters [15].

The normalized frequency, ω, the dimensional electrical excitation frequency, $\tilde{\omega}$, and the Definition of ω resonant frequency, $\tilde{\omega}_r$, are related by

155

$$\omega \overset{\Delta}{=} \frac{\tilde{\omega}}{2\tilde{\omega}_r}. \qquad (A.14)$$

At parametric resonance frequency $\tilde{\omega} = 2\tilde{\omega}_r$, ω is in the neighborhood of 1. A detuning Detuning

parameter ω_1 [17] [18] is introduced, where

parameter

ω_1

$$\omega = 1 + \varepsilon\omega_1. \qquad (A.15)$$

The quantity $\varepsilon\omega_1$ measures the closeness of excitation frequency to the principal parametric

resonance (equal to twice of the resonance frequency). Using (A.15), the relationship between

the electrical excitation frequency and the normalized frequency is rewritten as

$$\tilde{\omega} = 2\tilde{\omega}_r\left(1 + \varepsilon\omega_1\right) \qquad (A.16)$$

A.2.   METHOD OF AVERAGING

The method of averaging [15] is used to solve the second-order differential equation (A.8) Assumed

solution

for steady-state amplitude and phase with a constant angular frequency. It is applicable when the

evolution of the system can be separated into two time scales, and one time scale changes much

more rapidly than the other time scale [30]. The assumed solution to the normalized equation

(A.8), written in the amplitude and phase parameter space, is

$$x(t) = \alpha(t)\cos(\omega t + \beta(t)) \qquad (A.17)$$

The normalized time-varying amplitude $\alpha(t)$ and phase $\beta(t)$ are assumed to be slowly varying

with respect to the normalized frequency, ω. Differentiating (A.17) with respect to time yields

$$\dot{x}(t) = -\alpha\omega\sin(\omega t + \beta) + \dot{\alpha}\cos(\omega t + \beta) - \alpha\dot{\beta}\sin(\omega t + \beta). \qquad (A.18)$$

Since we are only interested in the steady-state solutions of α and β, we can assume that they do not change in the region of parametric resonance. Thus $\dot{\alpha} = \dot{\beta} = 0$. This leads to an additional condition on velocity to derive the "slow" equations of the amplitude and phase:

$$\dot{x}(t) = -\alpha(t)\omega\sin(\omega t + \beta(t)) \tag{A.19}$$

Setting (A.18) and (A.19) equal yields

$$\dot{\alpha}\cos(\omega t + \beta) - \alpha\dot{\beta}\sin(\omega t + \beta) = 0 \tag{A.20}$$

Twice differentiating (A.19) gives

$$\ddot{x} = -\alpha\omega^2\cos(\omega t + \beta) - \dot{\alpha}\omega\sin(\omega t + \beta) - \alpha\dot{\beta}\omega\cos(\omega t + \beta) \tag{A.21}$$

Using (A.12), the assumed solution (A.17), $\dot{x}$ and $\ddot{x}$ are substituted into (A.8) to rewrite the time derivatives of the amplitude α into a linear combination of sinusoidal components:

$$\begin{aligned}
&\left(-\dot{\alpha} - \varepsilon b\alpha\right)\omega\sin(\omega t + \beta) - \alpha\dot{\beta}\omega\cos(\omega t + \beta) + 2\varepsilon\alpha\cos(\omega t + \beta)\cos(2t) \\
&+ \varepsilon\delta_3\alpha^3\cos^3(\omega t + \beta) + \varepsilon\gamma_3\alpha^3\cos^3(\omega t + \beta)\cos(2t) = 0
\end{aligned} \tag{A.22}$$

Equations (A.20) and (A.22) are solved to find independent equations in terms of $\dot{\alpha}$ and $\dot{\beta}$. First, (A.22) is multiplied by $-\sin(\omega t + \beta)$, (A.20) is multiplied by $\omega\cos(\omega t + \beta)$ and the resulting two equations are added to eliminate $\dot{\beta}$. Utilizing trig identities and simplifying as a sum of different frequency components,

$$\dot{\alpha}\omega = -\frac{1}{2}\varepsilon b\alpha\omega + \frac{1}{2}\varepsilon\alpha\big[\sin(2(\omega+1)t+2\beta)+\sin(2(\omega-1)t+2\beta)\big]$$

$$+\frac{1}{8}\varepsilon\delta_3\alpha^3\big[\sin(4\omega t+4\beta)+2\sin(2\omega t+2\beta)\big]+\frac{1}{2}\varepsilon b\alpha\omega\cos(2\omega t+2\beta)$$

$$+\frac{1}{16}\varepsilon\gamma_3\alpha^3\big[\sin(2(2\omega+1)t+4\beta)+\sin(2(2\omega-1)t+4\beta)\big]$$

$$+\frac{1}{8}\varepsilon\gamma_3\alpha^3\big[\sin(2(\omega+1)t+2\beta)+\sin(2(\omega-1)t+2\beta)\big]$$

(A.23)

Equation (A.23) is a linear combination of two kinds of terms depending on whether or not the term has a non-zero time average and can be generalized as:

$$\omega\dot{\alpha} = \varepsilon\left\{\sum_i A_i(\alpha)\sin\big[(\kappa_i\omega+\rho_i)t+\theta_i(\beta)\big]+g(\alpha,\omega)+c(\omega)\right\}$$

(A.24)

where $A_i(\alpha)$, $(\kappa_i\omega+\rho_i)$, and $\theta_i(\beta)$, are the amplitude, angular frequency, and phase of the ith component, respectively, $\kappa_i \in \{0,\,2,\,4\}$, $\rho_i \in \{0,\,\pm2\}$, and $g(\alpha,\,\omega)+c(\omega)$ is an offset. The derivative of phase, $\dot{\beta}$, has an analogous form. Since $-1\le\sin(\cdot)\le1$, $-1\le\cos(\cdot)\le1$, and ε is small, assume α is bounded, $\dot{\alpha}=O(\varepsilon)$ and $\dot{\beta}=O(\varepsilon)$. Thus α and β vary slowly in the time interval $[0,\,2\pi/(\kappa_i\omega+\rho_i)]$, i.e. major parts of α and β are slowly varying functions.

Upon integration of (A.24) from 0 to the greatest common factor of $2\pi/(\kappa_i\omega+\rho_i)$, the slow- Case: $\omega\approx1$ α solution

varying components have zero angular frequency ($\kappa_i\,\omega+\rho_i=0$), and evaluates to a non-zero value after the integration with respect to time t. In contrast, the fast-varying terms with non-zero angular frequency ($\kappa_i\,\omega+\rho_i\ne0$) evaluate to zero after the integration. Recall (A.13), at or near parametric resonance, $\omega\approx1$. Because $\dot{\alpha}=O(\varepsilon)$, upon performing integration on (A.23) over its full period, $\dot{\alpha}$ can be pulled out of the integral. Keeping slowly varying term that has $\kappa_i(\omega-1)\approx0$ and dropping out the fast-varying terms result in the averaged equation:

$$\dot{\alpha}\omega = \frac{1}{2}\varepsilon\alpha\left[\sin\left(2(\omega-1)t+2\beta\right)\right] - \frac{1}{2}\varepsilon b\alpha\omega + \frac{1}{8}\varepsilon\gamma_3\alpha^3\left[\sin\left(2(\omega-1)t+2\beta\right)\right] \qquad (A.25)$$

In the neighborhood of the parametric resonance, $\omega \approx 1$, thus

$$\dot{\alpha} = f_1(\alpha,\beta) = \frac{1}{8}\varepsilon\alpha\left[-4b+\left(4+\gamma_3\alpha^2\right)\sin(2\beta)\right]. \qquad (A.26)$$

Similarly, another state equation of the phase β can be derived by multiplying (A.22) by Case: $\omega \approx 1$ β solution $\cos(\omega t + \beta)$, multiplying (A.20) by $\omega\sin(\omega t + \beta)$, and adding the two resulting equations. The resulting equation is written in a linear combination of sinusoidal terms and averaged over its full period:

$$\dot{\beta}\omega = \frac{1}{2}\varepsilon\cos\left(2(\omega-1)t+2\beta\right) + \frac{1}{2}\left(\delta-\omega^2\right) + \frac{3}{8}\varepsilon\delta_3\alpha^2 + \frac{1}{4}\varepsilon\gamma_3\alpha^2\cos\left(2(\omega-1)t+2\beta\right). \qquad (A.27)$$

Applying the detuning parameter ω_1 in (A.15) to (A.27) requires the knowledge of relative magnitude of the two terms where ω appears: $\varepsilon\cos\left(2(\omega-1)t+2\beta\right)$ and $\delta - \omega^2$. Using a Taylor series expansion in the order of ε gives

$$\begin{aligned}
&\varepsilon\cos\left(2(\omega-1)t+2\beta\right)\\
&= \varepsilon\cos\left(2\varepsilon\omega_1 t+2\beta\right)\\
&= \varepsilon\left[\cos(2\varepsilon\omega_1 t)\cos(2\beta) - \sin(2\varepsilon\omega_1 t)\sin(2\beta)\right]\\
&= \varepsilon\left[1 - \frac{(2\varepsilon\omega_1 t)^2}{2!} + \frac{(2\varepsilon\omega_1 t)^4}{4!} - \cdots\right]\cos(2\beta) - \varepsilon\left[2\varepsilon\omega_1 t - \frac{(2\varepsilon\omega_1 t)^3}{3!} + \frac{(2\varepsilon\omega_1 t)^5}{5!} - \cdots\right]\sin(2\beta)\\
&= \varepsilon\cos(2\beta) + \text{H.O.T.}
\end{aligned} \qquad (A.28)$$

$$\delta - \omega^2 = \delta - \left(1+\varepsilon\omega_1\right)^2 = \left(\delta-1\right) - 2\varepsilon\omega_1 + \text{H.O.T.} \qquad (A.29)$$

where H.O.T. stands for higher-order terms. Dropping out higher order terms for ε in (A.27) yields

$$\dot{\beta}(1 + \varepsilon\omega_1) = \frac{1}{2}\varepsilon\cos(2\beta) + \frac{1}{2}(\delta - 1) - \varepsilon\omega_1 + \frac{3}{8}\varepsilon\delta_3\alpha^2 + \frac{1}{4}\varepsilon\gamma_3\alpha^2\cos(2\beta). \tag{A.30}$$

On the left-hand side, because $\dot{\beta} = O(\varepsilon)$, dropping out higher order terms of ε yields $\dot{\beta}$.

Applying $\delta \approx 1$ to the right-hand side of the equation yields,

$$\dot{\beta} = f_2(\alpha, \beta) = \frac{1}{8}\varepsilon[3\alpha^2\delta_3 - 8\omega_1 + (4 + 2\gamma_3\alpha^2)\cos(2\beta)]. \tag{A.31}$$

Equations (A.26) and (A.31) form a 2nd order nonlinear time invariant system, which can be written as a state-space model $\dot{X} = f(X)$, where $X(t) = [\alpha(t)\ \beta(t)]^T$, and $f = (f_1, f_2)^T$ is continuously differentiable.

When $\omega \approx 1/2$, dropping out fast varying terms in (A.23) yields,

$$\dot{\alpha}\omega = -\frac{1}{2}\varepsilon b\alpha\omega + \frac{1}{16}\varepsilon\gamma_3\alpha^3\sin(2(2\omega - 1)t + 4\beta) \tag{A.32}$$

Because $\omega \approx 1/2$,

$$\dot{\alpha}\omega = -\frac{1}{4}\varepsilon b\alpha + \frac{1}{16}\varepsilon\gamma_3\alpha^3\sin(4\beta) \tag{A.33}$$

Similarly, the time derivative of β is

$$\dot{\beta}\omega = \frac{1}{2}(\delta - \omega^2) + \frac{3}{8}\varepsilon\delta_3\alpha^2 + \frac{1}{16}\varepsilon\gamma_3\alpha^2[\cos(2(2\omega - 1)t + 4\beta)] \tag{A.34}$$

Plugging in $\omega \approx 1/2$ and using the conclusion from (A.28) and (A.29) yield

$$\dot{\beta}\omega = \frac{1}{8}\varepsilon\left[3\delta_3\alpha^2 - 8\omega_1 + \frac{1}{2}\gamma_3\alpha^2\cos(4\beta)\right] \tag{A.35}$$

160

The averaged equations of α and β in the case of $\omega \approx 1/2$ correspond to a secondary parametric resonance that happens near $\tilde{\omega} = \tilde{\omega}_r$. This is beyond the content of this thesis and its full description can be found in [6].

When ω is away from 1 and 1/2, the parametric resonance condition no longer holds, and all the terms on the right-hand side of (A.24) are fast varying terms with zero time-average. Thus by setting $\dot{\alpha} = 0$ and $\dot{\beta} = 0$, the constant and trivial zero solution branches are derived.

$\boxed{\text{Case: } \omega \neq 1}$

A.3.   STEADY-STATE SOLUTIONS

The steady-state equilibrium point $X^* = [\alpha^* \ \beta^*]^T$ satisfies $\dot{X}\big|_{X=X^*} = f(X^*) = 0$. Consider the case when the effect of the air damping can be neglected, three nontrivial and one trivial (zero) steady-state responses [17] are derived by setting $\dot{\alpha} = 0$ and $\dot{\beta} = 0$.

$\boxed{\text{Normalized steady-state solution}}$

$\alpha_1^* = \pm 2\sqrt{\dfrac{1+2\omega_1}{3\delta_3 - 2\gamma_3}}$;	(A.36a)	$\beta_1^* = \pm \pi\left(n + \dfrac{1}{2}\right)$, where $n = 0, 1, 2, \ldots$;	(A.36b)
$\alpha_2^* = \pm 2\sqrt{\dfrac{-1+2\omega_1}{3\delta_3 + 2\gamma_3}}$;	(A.36c)	$\beta_2^* = \pm n\pi$, where $n = 0, 1, 2, \ldots$;	(A.36d)
$\alpha_3^* = \pm\sqrt{-\dfrac{4}{\gamma_3}}$;	(A.36e)	$\beta_3^* = \pm\dfrac{1}{2}\arccos\left(-\dfrac{3\delta_3}{\gamma_3} - 2\omega_1\right)$;	(A.36f)
$\alpha_4^* = 0$,	(A.36g)	$\beta_4^* = \pm\dfrac{1}{2}\arccos(2\omega_1)$,	(A.36h)

The resulting four equilibria are $X_i^* = [\alpha_i^*\ \beta_i^*]^T$, where $i = 1, 2, 3$, and 4. The matrix form of the equilibrium is $X^* = [X_1^*\ \ X_2^*\ \ X_3^*\ \ X_4^*]$. The denormalized steady-state amplitude solutions $a_i = a_i^* x_o$ and phase solutions $\beta_i = \beta_i^*$ are shown in (1.23).

Four normalized steady-state solutions are plotted in Figure A-1. The stability of the solutions noted on the figure is explained in section A.4.
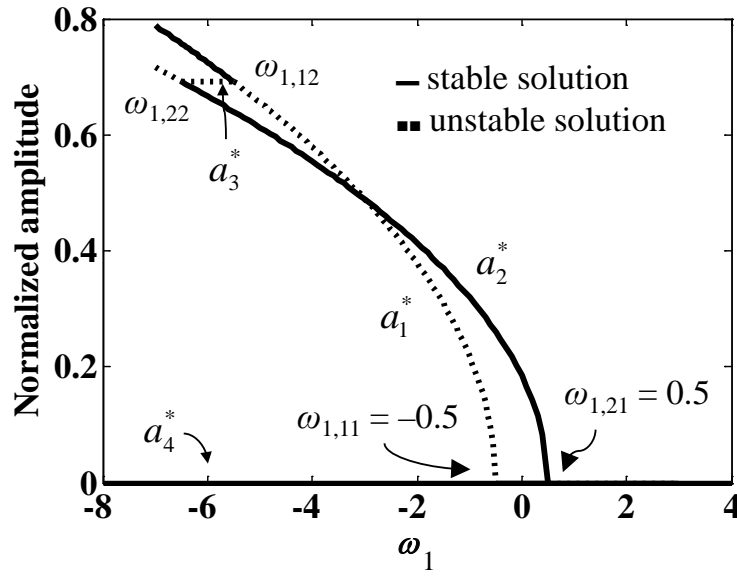
Figure A-1: Normalized steady-state response of a nonlinear parametric resonator.

A.4.   STABILITY ANALYSIS

The stability of the response amplitude and phase in (A.36) was extensively studied in [29] and [31]. A special case of the generalized stability analysis is included in this section to derive the "boundaries" between the stable and unstable solution branches. A two-step intuitive linear

transformation is used to analyze the branching of the multi-valued solutions in (A.36) and the frequencies where the bifurcation "jump" takes place.

To perform stability analysis, (A.26) and (A.31) are expanded into a Taylor series only to the first order terms around equilibrium points X_i^* (i = 1, 2, 3, and 4).

$$\dot{X} \cong J|_{X_i^*} \cdot \left(X - X^* \right). \qquad (A.37)$$

where $\dot{X} = [\dot{\alpha}\ \dot{\beta}]^T = [f_1\ f_2]^T$ and the Jacobian matrix, J, is

$$J|_{X_i^*} = \frac{\partial f(X)}{\partial X}\bigg|_{X=X_i^*} = \begin{bmatrix} \dfrac{\partial f_1}{\partial \alpha} & \dfrac{\partial f_1}{\partial \beta} \\[2mm] \dfrac{\partial f_2}{\partial \alpha} & \dfrac{\partial f_2}{\partial \beta} \end{bmatrix}\Bigg|_{X=X_i^*}. \qquad (A.38)$$

Defining a linear coordinate transformation $R = [r1, r2]^T = X - X^*$, because

$$\dot{R} = \dot{X}, \qquad (A.39)$$

this yields a nonlinear partial differential equation (PDE)

$$\dot{R} \cong J|_{X_i^*} \cdot R. \qquad (A.40)$$

In polar coordinates, ignoring damping, b, the coefficients of the Jacobian matrix are

$$\begin{aligned} \frac{\partial f_1}{\partial \alpha} &= \frac{1}{8}\varepsilon\left(4 + 3\gamma_3\alpha^2\right)\sin(2\beta) \\[2mm] \frac{\partial f_1}{\partial \beta} &= \frac{1}{4}\varepsilon\alpha\left(4 + \gamma_3\alpha^2\right)\cos(2\beta) \\[2mm] \frac{\partial f_2}{\partial \alpha} &= \frac{1}{4}\varepsilon\left[3\alpha\delta_3 + 2\alpha\gamma_3\cos(2\beta)\right] \\[2mm] \frac{\partial f_2}{\partial \beta} &= -\frac{1}{2}\varepsilon\left(2 + \gamma_3\alpha^2\right)\sin(2\beta) \end{aligned}. \qquad (A.41)$$

The eigenvalues λ_i and eigenvectors U_i of J satisfy

$$\lambda^2 - \text{trace}(J)\lambda + D(J) = 0, \qquad (A.42)$$

and

$$M^{-1}JM = J_d \equiv \begin{bmatrix} \lambda_1 & 0 \\ 0 & \lambda_2 \end{bmatrix}, \qquad (A.43)$$

where $D(J)$ denotes the determinant of a square matrix J, J_d is the Jordan matrix and M denotes the eigenvector pair $[U_1\ U_2]$. The eigenvalues determine the stability of the nonlinear system in the neighborhood of the equilibrium points. The trace of J equals to zero for the equilibria of the nonlinear system considered herein, because

$$\frac{\partial f_1}{\partial \alpha} = \frac{\partial f_2}{\partial \beta} = 0, \quad \text{for } \left(\alpha_1^*, \beta_1^*\right) \text{and} \left(\alpha_2^*, \beta_2^*\right),$$

$$\qquad (A.44)$$

$$\frac{\partial f_1}{\partial \alpha} = -\frac{\partial f_2}{\partial \beta} = -\varepsilon \sin(2\beta), \quad \text{for } \left(\alpha_3^*, \beta_3^*\right).$$

Hence the eigenvalue, λ, is given in terms of steady-state amplitude, phase, and normalized system parameters:

$$\lambda = \pm\sqrt{-D(J)} = \pm\frac{1}{4}\varepsilon\sqrt{\left(4+3\gamma_3\alpha^2\right)\left(2+\gamma_3\alpha^2\right)\sin^2(2\beta) + \alpha^2\left(4+\gamma_3\alpha^2\right)\left[3\delta_3 + 2\gamma_3\cos(2\beta)\right]\cos(2\beta)} .(A.45)$$

By a second coordinate transform $Z = M^{-1}R$, the PDE $\dot{R} \cong J \cdot R$ is linearized to

$$\dot{Z} = M^{-1}\dot{R} \cong M^{-1}JR = M^{-1}JMZ = J_d Z . \qquad (A.46)$$

The solution to (A.46) is

$$Z = \begin{bmatrix} z_1(0)e^{\lambda_1 t} & z_2(0)e^{\lambda_2 t} \end{bmatrix}^T . \qquad (A.47)$$

where $z_1(0)$ and $z_2(0)$ are the two initial states of Z. When $D(J) < 0$, λ_i are real and $\lambda_1\lambda_2 < 0$. If z_1 exponentially increases then z_2 decreases, and vice versa. One of the solutions always grows without bound and is hence unstable. This case results in an unstable *saddle* point, which is not physically realizable. When $D(J) > 0$, λ_i are complex conjugates $\lambda_i = \pm j\theta$. The zero real part

leads to a marginally stable *center* point (*i.e.* the solution follows a circular trajectory, thus bounded or ultimately bounded). Thus the roots of $D(J) = 0$ mark the "transition" between the stability and instability, defined as the "bifurcation" point.

For each equilibrium $\left(\alpha_i^*, \beta_i^*\right)$, $i = 1,2,3$ in (A.36), a Jacobian matrix is uniquely defined as a function of ω_1. Calculating the roots of its determinant yields four distinct normalized transition frequencies $\omega_{1,ij}$, where i denotes the ith equilibrium, and j denotes the jth transition.

(margin note: Normalized bifurcation frequencies)

$$\omega_{1,11}\Big|_{\left(\alpha_1^*,\beta_1^*\right)} = -0.5$$

$$\omega_{1,12}\Big|_{\left(\alpha_1^*,\beta_1^*\right)} = 0.5 - \frac{3\delta_3}{2\gamma_3}, \tag{A.48a}$$

$$\omega_{1,21}\Big|_{\left(\alpha_2^*,\beta_2^*\right)} = 0.5$$

$$\omega_{1,22}\Big|_{\left(\alpha_2^*,\beta_2^*\right)} = -0.5 - \frac{3\delta_3}{2\gamma_3}, \tag{A.48b}$$

$$\omega_{1,31}\Big|_{\left(\alpha_3^*,\beta_3^*\right)} = 0.5 - \frac{3\delta_3}{2\gamma_3}$$

$$\omega_{1,32}\Big|_{\left(\alpha_3^*,\beta_3^*\right)} = -0.5 - \frac{3\delta_3}{2\gamma_3}. \tag{A.48c}$$

Out of six transition frequencies, there are four distinct bifurcation points. The transition points of equilibrium $\left(\alpha_3^*, \beta_3^*\right)$ coincide with those of the other two equilibria:

(margin note: Four distinct bifurcation frequencies)

$$\omega_{1,12}\Big|_{\left(\alpha_1^*,\beta_1^*\right)} = \omega_{1,31}\Big|_{\left(\alpha_3^*,\beta_3^*\right)},$$

$$\omega_{1,22}\Big|_{\left(\alpha_2^*,\beta_2^*\right)} = \omega_{1,32}\Big|_{\left(\alpha_3^*,\beta_3^*\right)}. \tag{A.49}$$

The fourth solution $\left(\alpha_4^*, \beta_4^*\right)$ is always stable, thus $D(J) > 0$.

With the presence of a small perturbation from thermomechanical noise, the bifurcation Graphical representa-
"jump" event occurs at the transition frequency where stable and unstable regions meet [17]. As tion

graphically presented in Figure A-1, the normalized frequency transitions $\omega_{1,11}$ and $\omega_{1,21}$

represent the "pitchfork" bifurcation from the zero (trivial) solution branch α_4^* to the nontrivial

branches α_1^* and α_2^*, and $\omega_{1,12}$ ($\omega_{1,31}$) and $\omega_{1,22}$ ($\omega_{1,32}$) are the "saddle-node" bifurcation on the

frequency boundaries of the constant solution α_3^*. The stable solution regions are the ones with

$D(J) > 0$, while the unstable regions are determined by $D(J) < 0$.

(end)

APPENDIX B   DESIGNS AND SCRIPTS

T he non-interdigitated finger (NIF) comb, the tangential drive "T-drive", and the "shaped-finger" comb resonators are chosen as verification vehicles for the nonlinear parametric resonance theory and the behavioral simulation. Using symmetrical drives, these designs provide a force-displacement curve with an odd symmetry about the origin. The work on the NIF resonator verifies the parametric resonance theory and the behavioral modeling approach for complex nonlinear systems, which lays the foundation for the thesis work. A canonical NIF resonator, its analytic model, and experimental validation are described in detail in Chapter 2. Appendix B.1 includes the scripts in generating the steady-state frequency responses using the Mathieu equation perturbation solutions from Chapter 1 and Appendix A. The investigation of a tangential parametric drive is our first demonstration of a large-stroke parametric response and is included in Appendix B.3 to supplement Chapter 3. The "quadratic-shaped-finger" comb layout is synthesized using the SKILL scripts described in Appendix B.4. Customizing the finite-element simulator with Matlab® scripting language helps to facilitate electrostatic simulation and parametric sweeps, as described in Appendix B.5. Exploring independent tuning of linear and cubic electrostatic spring constants enables a "quartic-shaped-finger" comb in Appendix B.6.

B.1. NIF RESONATOR STEADY-STATE FREQUENCY RESPONSE SCRIPTS

Normalized steady-state frequency response of the nonlinear Mathieu Equation in Figure A-1, denormalized frequency response in Figure 1-4 and Figure 3-12 are generated with the following Matlab® scripts:

```
function steadyFreqResMathieuCMU
clear; clc
global omg_r f_n f_r eps delta3 gamma3
% linear electrostatic spring constant, uN/(um*V^2)
r1 = 0.000604990744449093;
% cubic electrostatic spring constant, uN/(um^3*V^2)
r3 = -101234078.913912;
% linear mechanical spring constant, uN/um
k1 = 3.3;
% cubic mechanical spring constant, uN/um^3
k3 = 4.79E+06;
% mass of the resonator, kg
m = 4.928E-10;
% damping
b_tilde = 1.410E-07;

% distance between two capacitive comb fingers, units in meters
x0 = 5e-6;

% applied voltages in (1.8)
Vdc = 40;
Vac = 20;
% natural frequency
omg_n = sqrt(k1/m);
% resonant frequency
omg_r = sqrt((k1 + r1*Vdc^2)/m);
f_n = omg_n/2/pi
f_r = omg_r/2/pi
% around parametric resonance of 2*omg_r
omg = 2*omg_r;

% dimensionless parameters
```

```
eps = 2*r1*Vac^2/m/omg^2
delta3 = 4*(k3 + r3*Vdc^2)*x0^2/m/omg^2/eps
gamma3 = 4*Vac^2*x0^2/m/omg^2*r3/eps
b = 2*b_tilde/eps/m/omg


% Min and max of the omg value specifying plotting range
omgSta = -7; omgEnd = 3;
step1 = 0.05; step2 = 0.1; step3 = 0.1;



%-------------------------------------------------------------------------%
% Determine the bifurcation and define the frequency ranges
% The bifurcation points where a stable center bifurcates to an unstable
% saddle. omgij denotes the boundary in the normalized frequency response
% (the amplitude-excitation frequency detuning parameter curve), where i =
% 1,2, refers to the bifurcation point corresponding to solution branch i,
% and j = 1 denotes the bifurcation emanates from the trivial solution,
% whereas j = 2 denotes the bifurcation to the constant amplitude branch.
%------------------------solution branch 1------------------------%
omg11 = -0.5
omg12 = 0.5 - 3*delta3/2/gamma3
% Calculated and print denormalized frequency, using function rfrq defined later
freq11 = rfrq(omg11)
freq12 = rfrq(omg12)

% Determine whether it's hardening nonlinearity depending on the value of omg11 and omg12
if omg11 < omg12
    fHard1 = 1;
    omgReg11 = omgSta:step1:omg11;
    omgReg12 = omg11:step1:omg12;
    omgReg13 = omg12:step1:omgEnd;
else
    fHard1 = 0;
    omgReg11 = omgSta:step1:omg12;
    omgReg12 = omg12:step1:omg11*0.85;
    omgReg13 = omg11:step1:omgEnd;
end

%smaller value of omg11 and 12
omg1s = (omg11*fHard1+omg12*(1-fHard1));
%the larger value of 11 and 12
omg1l = (omg12*fHard1+omg11*(1-fHard1));
```

```
%------------------------solution branch 2------------------------%
omg21 = 0.5
omg22 = -0.5 - 3*delta3/2/gamma3
% Print denormalized frequency
freq21 = rfrq(omg21)
freq22 = rfrq(omg22)

if omg21 < omg22
    fHard2 = 1;
    omgReg21 = omgSta:step2:omg21;
    omgReg22 = omg21:step2:omg22;
    omgReg23 = omg22:step2:omgEnd;
else
    fHard2 = 0;
    omgReg21 = omgSta:step2:omg22;
    omgReg22 = omg22:step2:omg21*1.15;
    omgReg23 = omg21:step2:omgEnd;
end
omg2s = (omg21*fHard2+omg22*(1-fHard2));
omg2l = (omg22*fHard2+omg21*(1-fHard2));

%------------------------solution branch 3------------------------%
% The solution branch 3 always connects the two center-saddle bifurcation
% points, as picked by the determinant of Jacobian matrix evaluated at the
% equilibria of solution branch 3
omgReg3 = min(omg12,omg22):step3:max(omg12,omg22);


%-------------------------- Normalized frequency response --------------------------%
figure

% Plot line color and linewidth handle, used to globally change the line properties
ColorSta = 'k-';
ColorUnsta = 'k:';
lineW = 3;

%Calculate the amplitudes of each of the three regions for the three solution branches
a11 = 2.*sqrt((1 + 2.*omgReg11)./(3*delta3 - 2*gamma3));
a12 = 2.*sqrt((1 + 2.*omgReg12)./(3*delta3 - 2*gamma3));
a13 = 2.*sqrt((1 + 2.*omgReg13)./(3*delta3 - 2*gamma3));
a21 = 2.*sqrt((-1 + 2.*omgReg21)./(3*delta3 + 2*gamma3));
a22 = 2.*sqrt((-1 + 2.*omgReg22)./(3*delta3 + 2*gamma3));
```

```matlab
a23 = 2.*sqrt((-1 + 2.*omgReg23)./(3*delta3 + 2*gamma3));
a3 = sqrt(-4./gamma3) .* ones(1,length(omgReg3));

% Calculate and display amplitude at bifurcation
a_bif = x0*2*sqrt((-1 + 2*omg11)/(3*delta3 + 2*gamma3))

% Determine the stability of the solution branches
% Use the sign of the determinant of the Jacobian matrix for the state-space
% model (the RHS of dot(x) and dot(y)), solved at omg's neighborhood

%------------------------solution branch 1------------------------%
% Plot region 1 of solution branch a1
if det1(omg1s-0.01) > 0
    %omgReg11 is a locally stable region
    plot(omgReg11, a11, ColorSta, 'Linewidth', lineW)
else
    %omgReg11 is a locally unstable region
    plot(omgReg11, a11, ColorUnsta, 'Linewidth', lineW)
end
hold on

%Plot region 2 of solution branch a1
if det1(omg1s+0.01) > 0
    %omgReg12 is a locally stable region
    plot(omgReg12, a12, ColorSta, 'Linewidth', lineW)
else
    %omgReg12 is a locally unstable region
    plot(omgReg12, a12, ColorUnsta, 'Linewidth', lineW)
end
text((omg1s+omg1l)/3,2*sqrt((1 + 2*(omg1s+omg1l)/3)/...
    (3*delta3 - 2*gamma3)),'a1 \rightarrow','HorizontalAlignment','right');

%Plot region 3 of solution branch a1
if det1(omg1l+0.01) > 0
    %omgReg13 is a locally stable region
    plot(omgReg13, a13, ColorSta, 'Linewidth', lineW)
else
    %omgReg13 is a locally unstable region
    plot(omgReg13, a13, ColorUnsta, 'Linewidth', lineW)
end
```

```
%------------------------solution branch 2------------------------%
%Plot region 1 of solution branch a2
if det2(omg2s-0.01) > 0
    %omgReg21 is a locally stable region
    plot(omgReg21, a21, ColorSta, 'Linewidth', lineW)
else
    %omgReg21 is a locally unstable region
    plot(omgReg21, a21, ColorUnsta, 'Linewidth', lineW)
end
%Plot region 2 of solution branch a2
if det2(omg2s+0.01) > 0
    %omgReg22 is a locally stable region
    plot(omgReg22, a22, ColorSta, 'Linewidth', lineW)
else
    %omgReg22 is a locally unstable region
    plot(omgReg22, a22, ColorUnsta, 'Linewidth', lineW)
end
text((omg2s+omg2l)*.2*0.8,2*sqrt((-1 + 2*(omg2s+omg2l)*.2)/...
    (3*delta3 + 2*gamma3)),'\leftarrow a2','HorizontalAlignment','left');
%Plot region 3 of solution branch a2
if det2(omg2l+0.01) > 0
    %omgReg23 is a locally stable region
    plot(omgReg23, a23, ColorSta, 'Linewidth', lineW)
else
    %omgReg23 is a locally unstable region
    plot(omgReg23, a23, ColorUnsta, 'Linewidth', lineW)
end

%------------------------solution branch 3------------------------%
% Plot constant amplitude solution branch a3
% omgReg3 is a locally unstable region since its determinant is always negative
if -4/gamma3 > 0
    plot(omgReg3, a3, ColorUnsta, 'Linewidth', lineW)
    text((omg12+omg22)/2/0.93,sqrt(-4/gamma3)*1.01, ...
        'a3\downarrow','VerticalAlignment','bottom', ...
        'HorizontalAlignment','center');
end

xlabel('\omega_1'); ylabel('Normalized amplitude');
title('Normalized frequency response');
set(gca,'FontName','Times New Roman','FontWeight','bold','FontSize', 18);
set(get(gca,'YLabel'),'FontName','Times New Roman','FontWeight','bold','FontSize', 18)
```

```matlab
set(get(gca,'XLabel'),'FontName','Times New Roman','FontWeight','bold','FontSize', 18)




% ---------------------Denormalized frequency response ------------------------%
figure
%-----------------------solution branch 1-----------------------%
% Plot region 1 of solution branch a1
if det1(omg1s-0.01) > 0
    %omgReg11 is a locally stable region
    plot(rfrq(omgReg11), x0.*a11, ColorSta, 'Linewidth', lineW)
else
    %omgReg11 is a locally unstable region
    plot(rfrq(omgReg11), x0.*a11, ColorUnsta, 'Linewidth', lineW)
end
hold on

% Plot region 2 of solution branch a1
if det1(omg1s+0.01) > 0
    %omgReg12 is a locally stable region
    plot(rfrq(omgReg12), x0.*a12, ColorSta, 'Linewidth', lineW)
else
    %omgReg12 is a locally unstable region
    plot(rfrq(omgReg12), x0.*a12, ColorUnsta, 'Linewidth', lineW)
end

%Plot region 3 of solution branch a1
if det1(omg1l+0.01) > 0
    %omgReg13 is a locally stable region
    plot(rfrq(omgReg13), x0.*a13, ColorSta, 'Linewidth', lineW)
else
    %omgReg13 is a locally unstable region
    plot(rfrq(omgReg13), x0.*a13, ColorUnsta, 'Linewidth', lineW)
end

%-----------------------solution branch 2-----------------------%
%Plot region 1 of solution branch a2
if det2(omg2s-0.01) > 0
    %omgReg21 is a locally stable region
    plot(rfrq(omgReg21), x0.*a21, ColorSta, 'Linewidth', lineW)
else
    %omgReg21 is a locally unstable region
```

```matlab
    plot(rfrq(omgReg21), x0.*a21, ColorUnsta, 'Linewidth', lineW)
end

% Plot region 2 of solution branch a2
if det2(omg2s+0.01) > 0
    %omgReg22 is a locally stable region
    plot(rfrq(omgReg22), x0.*a22, ColorSta, 'Linewidth', lineW)
else
    %omgReg22 is a locally unstable region
    plot(rfrq(omgReg22), x0.*a22, ColorUnsta, 'Linewidth', lineW)
end

% Plot region 3 of solution branch a2
if det2(omg2l+0.01) > 0
    %omgReg23 is a locally stable region
    plot(rfrq(omgReg23), x0.*a23, ColorSta, 'Linewidth', lineW)
else
    %omgReg23 is a locally unstable region
    plot(rfrq(omgReg23), x0.*a23, ColorUnsta, 'Linewidth', lineW)
end

%-----------------------solution branch 3-----------------------%
% Plot constant amplitude solution branch a3
% omgReg3 is a locally unstable region since its determinant is always negative
if -4/gamma3 > 0
    plot(rfrq(omgReg3), x0.*a3, ColorUnsta, 'Linewidth', lineW)
end

%--------------------Trivial solution branch ----------------------%
% Plot trivial (zero) solution branch a4
% Trivial solution is physically stable in an aligned comb setup
omgReg4 = omgSta:min(step2,step1):omgEnd;
plot(rfrq(omgReg4), zeros(length(omgReg4)), ColorSta, 'Linewidth', 4)

xlabel('Frequency [Hz]'); ylabel('Amplitude [m]');
title('Un-normalized frequency response');


%----------------Functions to avoid duplicate calculations--------------------%
% Determinants of the Jacobian matrix evaluated at an equilibrium point
function d1 = det1(omg1)
global delta3 gamma3
```

d1 = (1+2*omg1)*(3*delta3 - gamma3 + 2*omg1*gamma3)/(3*delta3 - 2*gamma3);

function d2 = det2(omg1)
global delta3 gamma3
d2 = (1-2*omg1)*(3*delta3 + gamma3 + 2*omg1*gamma3)/(3*delta3 + 2*gamma3);

% Calculate denormalized electrical excitation frequency
function denormfre = rfrq(normfreq)
global f_r eps
denormfre = 2.*f_r.*(1 + eps.*normfreq);

B.2.   TRANSIENT CHIRP SIMULATION VERILOG-A MODEL

The transient chirp simulation using Cadence® Spectre is used to sweep the excitation VCF model frequency to yield the frequency response curve. A key element in this simulation is a voltage-controlled force source (VCF) model whose output, $F_{out}(t)$, is controlled by a piecewise-linear voltage $v_{in}(t)$. The VCF model is implemented in Verilog-A. This section describes the encoding of the model and its performance in benchmark simulations.

The oscillation frequency of the VCF is related to the control voltage by

$$f_{out}(t) = f_{center} + G_{VCO} v_{in}(t), \tag{B.1}$$

where f_{center} is the center frequency and G_{VCO} is the frequency gain. Typically, a VCF behavior model integrates the oscillation frequency to compute the phase of the output force

$$\psi_{out}(t) = 2\pi \int_{-\infty}^{t} f_{out}(\tau)\, d\tau . \tag{B.2}$$

and assign it to a sinusoidal function to form the output force waveform

$$F_{out}(t) = F_m \sin\left[\psi_{out}(t) + \psi_0\right]. \tag{B.3}$$

175

where Ψ_0 is the initial phase and F_m is the force amplitude.

The control voltage $v_{in}(t)$ generally varies slower than the frequency of the output sinusoidal

force $F_{out}(t)$. Thus the VCF model must be capable of "tracking" the fast varying output signal

whose frequency is not a constant. The Verilog-A code of the VCF model starts with the

calculation of controlled frequency and then notify the simulator of the fast-varying sinusoidal

output waveform whose frequency is modulated by a slowly varying control voltage.

```verilog
module vco_sin(va, fout);
// Port declaration and the assignment of the corresponding disciplines
  input va;
  output fout;
  electrical va;
  mems_kinematic_translational fout;

// Definition of the parameters
  parameter real  amplitude = 1;
  parameter real  center_freq = 1K;
  parameter real  vco_gain = 1;
  parameter real  phase = 0;
// Time steps per output waveform period
  parameter integer step = 32;

  real frequency;
  real inst_phase;
  real ini_phase;

  analog begin
    // Calculate the controlled frequency and the initial phase
    frequency = center_freq + V(va) * vco_gain;
    ini_phase = phase * `M_PI / 180.0;
    // Limit the internal simulator time step so it's always within 1/step of the period
    $bound_step(1.0 / (step*frequency));

    // Calculate the instantaneous phase using the idtmod function
    inst_phase  = idtmod(frequency,0.0,1.0,-0.5);
```

```
    // Assign the output using the instantaneous phase
    f(fout) <+ amplitude*sin(2* `M_PI * inst_phase + ini_phase);
  end
endmodule
```

The instantaneous phase is calculated by the *idtmod* function, a bounded "circular integrator" defined in Verilog-A. Unlike *idtmod*, the *idt* function (integration of time) is unbounded. The function *idtmod* always keeps the sinusoidal function within the range of $[-\pi, \pi]$. On the other hand, the *idt* produces unbounded output which is susceptible to tolerance and round-off errors.

idtmod function

It's important to notify the simulator to limit the internal time step, so that simulator can successfully "keep track of" the smooth changes in a sinusoidal waveform. Using the simulator directive $bound_step(1.0 / (step*frequency)), the simulator changes the output at specified time points specified by the user even if there's no change in the input. "Step" (unitless) is the time step per period that is used to specify at what phase point the output must be updated. The larger the step, the smoother the output waveform becomes.

bound_step function

B.3.   TANGENTIAL DRIVE (T-DRIVE) RESONATOR

A "tangential drive" parametric resonator is our first device to study the parametric resonance in systems with high energy storage. In a prior demonstration by [48], one way of electrostatically achieving a large motional stroke is through the use of the tangential motion of a "T-drive" (short for the name "tangential drive"): rotor electrode suspended by a slanted-beam flexure, as shown in Figure B-1.

T-drive topology
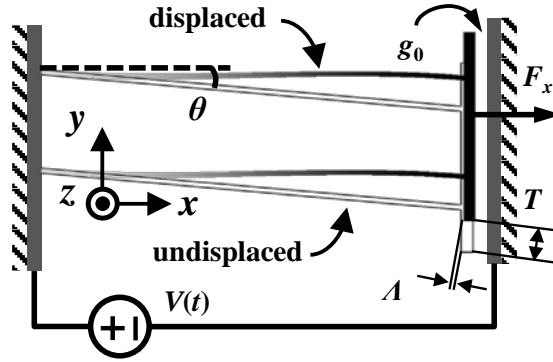
Figure B-1: Plane view of the T-drive flexure and its finite element simulated deformed shape. Λ and T indicate the axial and lateral displacements of the rotor electrode, respectively.

Figure B-2 shows a slanted flexure design exhibiting nonlinear in-plane motion used as a Device suspension to a parallel-plate capacitor. The bases of the slanted beams are attached to a curl-match frame. The plate mass in the center of Figure B-2 is connected to the T-drive rotor electrode through the decoupling springs. The design parameters are shown in Table B-1.

Table B-1: T-drive resonator geometric parameters

Symbol	Parameter	Layout	Fabricated
w_f	slanted flexure width	2.00 μm	2.62 μm
l_f	slanted flexure length	221.8 μm	222.3 μm
θ	slanted flexure angle	5.0°	
w_r	drive electrode width	6.0 μm	6.2 μm
l_r	drive electrode length	100.0 μm	99.8 μm
t	structure thickness	4.83 μm	
g_0	initial electrode gap	1.00 μm	0.89 μm
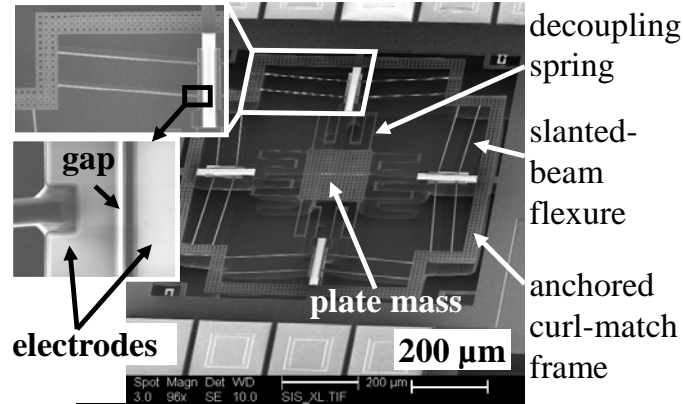
Figure B-2: A large displacement T-drive parametric resonator, with zoom-in view of the electrode gap.
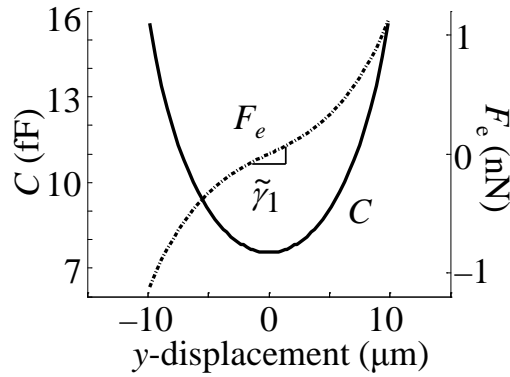
Figure B-3: Capacitance and force versus the *y*-displacement for a symmetric T-drive.

The large displacement is realized by taking advantage of the large parallel-plate motion C-x and F_e-x curves capability in *y* and the high electrostatic force in *x* due to the small gap. The T-drive generates a large parallel-plate electrostatic force while the flexures constrain motion parallel to the electric field, which allows large-amplitude motion. Figure B-3 is the force-displacement relationship of

a symmetric T-drive (force calculation includes both the top and bottom slanted flexures in Figure B-2). Nonlinearly varying the gap between the aligned electrodes leads to electrostatic cubic stiffness when the slanted beam deflects.

Both harmonic and parametric responses are directly excited with the T-drive. Figure B-4 is Harmonic response the measured frequency response in air under a harmonic drive voltage. The first and second in-plane resonance modes are at 18.67 kHz and 44.60 kHz, respectively. Out-of-plane modes at 22.67 kHz and 38.20 kHz are also observed which can be moved far away from the in-plane modes by an increased device layer thickness.
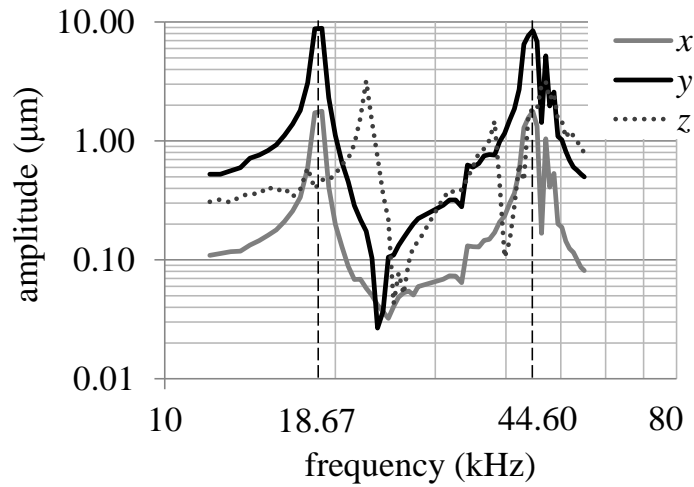
Figure B-4: The measured frequency response of the T-drive resonator under a single-sided excitation.

The analytic parametric steady-state response is experimentally validated by a frequency up- Parametric response sweep. The electric excitation frequency was swept around the predicted principal parametric resonance at $f_{21} = 87.08$ kHz until a "jump" in amplitude was observed. The measured parametric

180

resonance response is shown in Figure B-5. At 88.27 kHz a jump occurs from a small driven response to a large amplitude of around 7 μm.
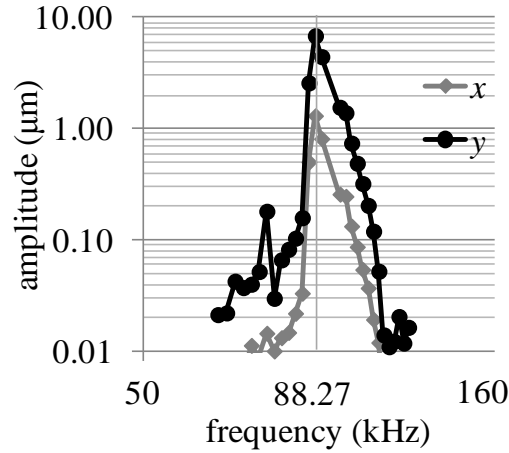
Figure B-5: The measured parametric resonance response corresponding to the second in-plane resonance mode.

B.4.   QUADRATIC-SHAPED-FINGER COMB LAYOUT SYNTHESIS

SKILL scripts are used to synthesize the shaped-finger comb layout. The scripts are made Intro to SKILL from the Pcells commands in the Cadence Virtuoso® environment. Pcells (parameterized cells) enable a designer to generate a canonical line or shape, assign parameters that describe the profile of the shape and then instantiate the Pcell with parameter values that span the design space. SKILL scripts using Pcell eases layout generation and enable users to create a wider range of shapes than allowed by the graphical user interface of the Pcell.

This section documents the Pcell SKILL scripts for generating shaped-finger comb layout in the Cadence Virtuoso® environment. Details about the use of Pcell commands to create an initial SKILL script can be found in the Cadence documentation.

```
; library and name of the cell that will be generated
pcDefinePCell(list(ddGetObj("soi001")    "shaped_stator_half_noTip_go5_gov3_xov16_1260pt"
"layout") nil
; user-specified parameters
              go = 5.0
              gov = 3.0
              xov = 16.0
              xo = xov/(go/gov - 1.0)
              ; finger length
              length = 15.0 + xov
              ; impose the smallest tip width (determined by litho, mask etc)
              ; calculate the tip location "xstart"
              tipWidth = 0.8
              xstart = xo*(go/(-tipWidth/2.0 + go) - 1.0)

              ; number of points excluding the last point that encloses the shape
              numpt = 1260
              ; make a null point list "ptList"
              ptList = nil

; add first two points which define the straight portion of the tip
firstListEntry = list((xstart:0.0) (xstart:-tipWidth/2.0))
; append the first two entries to the point list
ptList = append(ptList firstListEntry)

; calculate the point coordinates defined by the shape function and
; the list operation that appends calculated coordinates to the end of the list
for( i 0 numpt-1
              x = length/(numpt - 1.0)*i
              ; only generate the points other than the "tip region"
              if( (x >= xstart) then
                            ; enter the function that governs the shape here
                            y = go/(1.0 + x/xo) - go
                            ; make a new list entry based on the x and y coordinates
```

```
                              newListEntry = list((x:y))
                                 ; append the new entry to the point list
                                 ptList = append(ptList newListEntry)
; for debugging purpose, one can print the list out using: printf("x = %f, y = %f\n" x y)
                      )
)



; finally append the last point which encloses the polygon
x = length*1.0
y = 0.0
lastListEntry = list((x:y))
; append the last entry to the point list
ptList = append(ptList lastListEntry)



; let function scopes the variables so they can only be referenced within this function
   let((pcMember pcStretchGroup stretchOffsetX stretchOffsetY pcLib
                pcMaster pcInst pcTerm pcPin pcPinName
                pcNet pcTermNet pcNetName pcTermNetName pcMosaicInst
                pcParameters pcParamProp pcStep pcStepX pcStepY
                pcRepeat pcRepeatX pcRepeatY pcIndexX pcIndexY
                pcLayer pcPurpose pcLabelText pcLabelHeight pcPropText
                pcParamText pcCoords pcPathWidth pcPolygonMargin
              )
              (pcLib = (pcCellView~>lib))
              (pcParameters = ((pcCellView~>parameters)~>value))
; "pcLayer" specifies drawing layer
              (pcLayer = 1)
              (pcPurpose = "drawing")
; generate the shape using the list of coordinates that defines the freeform shape – ptList
              (pcInst = dbCreatePolygon(pcCellView
                              list(pcLayer pcPurpose)
; point list variable that stores the list that defines the polygon
                              ptList
              )) t
   )
)
```

B.5. ELECTROSTATIC SIMULATION OF THE SHAPED-FINGER COMB

Comsol Multiphysics® (3.5a with Matlab®) is used to perform electrostatic simulation of the shaped-finger comb and provide the capability for parametric sweeping. The model m-file was built in Matlab® R2012a.

```
function [C, skipedDisp] = swp_func_shapedComb_3rotor_SEM(numPt,plotV,plotW,plotE)
flclear fem

% COMSOL geometric file, saved with the help of COMSOL GUI
flbinaryfile='shapedComb_3rotor_SEM_v2.mphm';


% Draw the initial geometry, take the geometries from the .mphm file
% Alternatively, one can use geomedit or similar commands to build the geometry from scratch
clear draw
g1=flbinary('g1','draw',flbinaryfile);
g4=flbinary('g4','draw',flbinaryfile);
g8=flbinary('g8','draw',flbinaryfile);
draw.s.objs = {g1,g4,g8};
draw.s.name = {'CO1','CO2','R1'};
draw.s.tags = {'g1','g4','g8'};
fem.draw = draw;
% Plot enable
% Enables postplot of electric potential
plotEnable_V = plotV;
% Enables postplot of electric energy density
plotEnable_W = plotW;
% Enables postplot of electric field
plotEnable_E = plotE;

% Number of straight rotor fingers
N = 47;

% Thickness of electrodes from SEM
thickness = 13.15E-06;
```

```
% Start to sweep the displacement
ini_disp = -10e-6;
fin_disp = 10e-6;
step_disp = (fin_disp - ini_disp) / numPt;
% index of capacitance matrix
i = 1;



% Begin sweeping the lateral motion
% Initially move the rotor electrode to the ini_disp (negative max disp)
% Move the electrode in x direction
g1=move(g1,[ini_disp,0]);

% skipedDisp records the skipped displacement values in case of mesh difficulty
skipedDisp = [];



for disp = ini_disp: step_disp : fin_disp
    % Define constants since fem will be cleared at the end of each loop
    fem.const = {'Vnlosc','1'};

    % Re-analyze geometry
    clear s
    s.objs={g1,g4,g8};
    s.name={'CO1','CO2','R1'};
    s.tags={'g1','g4','g8'};

    fem.draw=struct('s',s);
    fem.geom=geomcsg(fem);

    % Initialize mesh
    % It is possible to have mesh difficulties when the finger engagement changes
    % because this also changes the instantaneous gap
    flag_skip = 0;
    try
        fem.mesh=meshinit(fem,'hauto',2);
    catch
        fprintf('An error occurred when trying extra fine mesh at x = %e. Try finer mesh.\n',disp);
        try
            fem.mesh=meshinit(fem,'hauto',3);
        catch
            fprintf('->An error occurred while trying the finer mesh. Now try normal mesh.\n');
```

```
      try
         fem.mesh=meshinit(fem,'hauto',5);
      catch
         fprintf('->An error occurred when trying normal mesh.Try extremely coarser mesh.\n');
         try
            fem.mesh=meshinit(fem,'hauto',9);
         catch
            fprintf('-->An error occurred while trying the extremely coarser mesh. \n');
            fprintf('Now skip displacement = %e.\n',disp);
            flag_skip = 1;
            skipedDisp = [skipedDisp disp];
         end
      end
   end
end


% If there is an error on mesh even for the extremely coarse mesh, skip this
% block and move g1 to the next iteration
if (~flag_skip)
   % Refine mesh
   fem.mesh=meshrefine(fem, 'mcase',0, 'rmethod','regular');

   % Application mode 1
   clear appl
   appl.mode.class = 'EmElectrostatics';
   appl.module = 'MEMS';
   appl.sshape = 2;
   appl.border = 'on';
   appl.assignsuffix = '_emes';

   % Define boundary conditions
   clear bnd
   bnd.V0 = {0,'Vnlosc',0};
   bnd.type = {'V0','V','nD0'};
   bnd.name = {'gnd','nlosc','zero charge'};


   % --------------------Boundary condition assignment----------------------%
   % Find the boundary index number from each object
   % The corresponding boundary conditions (BC) and their indices are
```

%	object	rotor	air	stator
%	s.objs	g1	g8	g4
%	s.name	CO1	R1	CO2
%	BC	gnd	zero	nlosc
%	bnd.ind	1	3	2

```
% Get boundary index (stored in matrices in ctx) that corresponds to
% each of the objects in the object list
ctx = geomcsg({g1, g4, g8},'Out','ctx');
% NOTE: ctx is a cell so ctx{1,1} retrieves the first sparse matrix that
% corresponds to the first g1 on the list enclosed in {};

% COMSOL stores all the boundary indices in a sparse matrix whose
% nonzero element row index is just the boundary index.
% "find" function locates the nonzero indeces in a sparse matrix
% and thus gets the boundary indices and store them in ctxbndind1.

[ctxbndind1, col1] = find(ctx{1,1});
for p = 1:length(col1)
    if col1(p) ~= p
        fprintf('Something seems to be wrong in ctx structure at col1 index = %e.\n',p)
    end
end

[ctxbndind2, col2] = find(ctx{1,2});
for p = 1:length(col2)
    if col2(p) ~= p
        fprintf('Something seems to be wrong in ctx structure at col2 index = %e.\n',p)
    end
end

[ctxbndind3, col3] = find(ctx{1,3});
for p = 1:length(col3)
    if col3(p) ~= p
        fprintf('Something seems to be wrong in ctx structure at col3 index = %e.\n',p)
    end
end

% Sweep all the ctxbndind matrices to find boundaries that
% correspond to their own BC and assign the BC number.
% Total number of boundaries
totalnoboundaries = length(ctxbndind1) + length(ctxbndind2) + length(ctxbndind3);
```

```
% create empty bnd.ind matrix
bnd.ind = zeros(1,totalnoboundaries);

% Store boundary indices into bnd.ind which is then used by COMSOL to
% solve for the boundary value problem
bnd.ind(ctxbndind1) = 1;
bnd.ind(ctxbndind2) = 2;
bnd.ind(ctxbndind3) = 3;


appl.bnd = bnd;
clear equ
equ.epsilonr = {1,'mat1_epsilonr'};
equ.name = {'air','Si'};
equ.ind = [1,2,2];
appl.equ = equ;
fem.appl{1} = appl;
fem.frame = {'ref'};
fem.border = 1;
clear units;
units.basesystem = 'SI';
fem.units = units;

% Library materials
clear lib
lib.mat{1}.name='Si(c)';
lib.mat{1}.varname='mat1';
lib.mat{1}.variables.nu='0.28';
lib.mat{1}.variables.E='170e9[Pa]';
lib.mat{1}.variables.epsilonr='11.7';
lib.mat{1}.variables.alpha='2.6e-6[1/K]';
lib.mat{1}.variables.C='700[J/(kg*K)]';
lib.mat{1}.variables.rho='2329[kg/m^3]';
lib.mat{1}.variables.k='130[W/(m*K)]';


fem.lib = lib;

% ODE Settings
clear ode
clear units;
units.basesystem = 'SI';
```

```
        ode.units = units;
        fem.ode=ode;

        % Multiphysics
        fem=multiphysics(fem);

        % Extend mesh
        fem.xmesh=meshextend(fem);

        % Solve problem
        fem.sol=femstatic(fem, 'solcomp',{'V'}, 'outcomp',{'V'}, 'blocksize','auto');

        % Save current fem structure for restart purposes
        fem0=fem;

        % Calculate and save capacitance by integrating it along the fingers
        % energy per thickness, Comsol assumes thickness = 1 m
        C(1,i) = disp;
        C(2,i) = postint(fem,'We_emes','unit','J/m','recover','off','dl',1);

        % This simulation is for 3 comb fingers, N is the total number of straight rotor fingers
        % C = 2*thickness*energy per thickness
        C(2,i) = N / 3 * thickness * 2 * C(2,i);

        % clear fem in case the new instance of simulation overwrites the previous one
        flclear fem

        % Plot electric energy density and normal electric field
        plotfemsoln(fem0,plotEnable_V,plotEnable_W,plotEnable_E)

        % increase the index
        i = i + 1;

    % end of flag_skip block
    end


    % Move the rotor electrode
    g1=move(g1,[step_disp,0]);

% end of for block
end
```

```
function plotfemsoln(fem,plotEnable_V,plotEnable_W,plotEnable_E)
% Plot solutions from fem

% Axis limit for COMSOL postplot function
axis_limit_postplot = [1.5E-5,8.4E-5,2.27E-5,5.0E-5];

% Plot electric potential
if plotEnable_V
   figure; postplot(fem, ...
          'tridata',{'V','cont','internal','unit','V'}, ...
          'trimap','Rainbow', ...
          'title','Surface: Electric potential [V]', ...
          'axis',axis_limit_postplot);
end


% Electric energy density heatmap rendering
if plotEnable_W
   figure; postplot(fem, ...
          'contdata',{'We_emes','cont','internal','unit','J/m^3'}, ...
          'contlevels',[colon(0,0.5/49,0.5)], ...
          'contlabel','off', ...
          'contmap','Thermal', ...
          'contmapstyle','reverse', ...
          'contfill','on', ...
          'title','Contour: Electric energy density [J/m^3]', ...
          'axis',axis_limit_postplot);
   box on
end


% Normal electric field heatmap rendering
if plotEnable_E
   figure; postplot(fem, ...
          'contdata',{'normE_emes','cont','internal','unit','V/m'}, ...
          'contlevels',50, ...
          'contlabel','off', ...
          'contmap','Thermal', ...
          'title','Contour: Electric field, norm [V/m]', ...
          'axis',axis_limit_postplot);
end
```

B.6.   QUARTIC-SHAPED-FINGER COMB RESONATOR

To deliver a well-designed electrostatic nonlinearity, a revised comb shape can be synthesized to incorporate a nonlinear cubic displacement term in the denominator of (3.1). This leads to the design and analysis of a "quartic-shaped-finger" comb parametric drive. It is used to provide independent control of both linear and cubic electrostatic spring constants.

<div style="text-align:right">Quartic-
shaped-
finger comb</div>
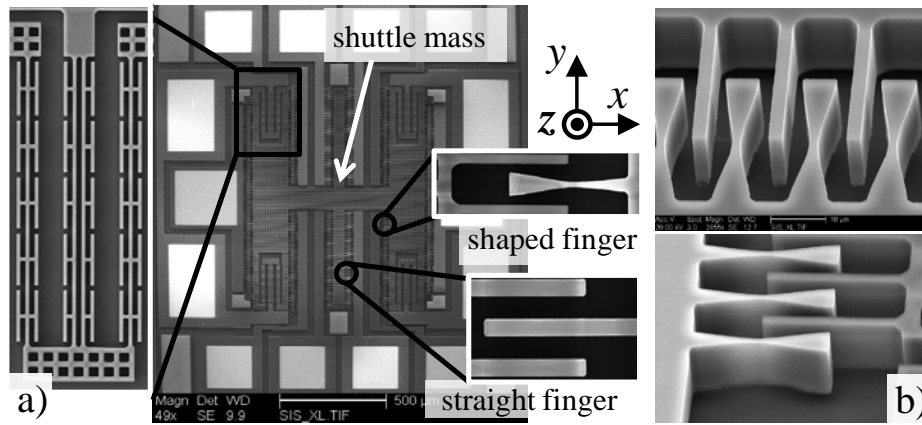
Figure B-6: SEM of (a) an SOI quartic-shaped comb parametric resonator that moves in *x*, (b) perspective view of the quartic-shaped comb fingers.

The "quartic-shaped-finger" comb resonator investigates the saddle-node bifurcation at a high amplitude solution branch shown as f_{22} in Figure 1-4. A fabricated SOI resonator with quartic-shaped-finger combs is shown in Figure B-6(a) with the perspective view of the finger shape in Figure B-6(b). Suspended by a linear flexure that only moves in *x*, the plate mass is

<div style="text-align:right">Device</div>

perforated for the purpose of release. The flexure beams have fins on both sides to protect the sidewall from lateral etch during the silicon DRIE step of the SOI-MEMS process [25].

The gap profile takes the form of

$$g(x_1) = \frac{g_o}{1 + x_1/x_{o1} + x_1^3/x_{o3}}.$$

(B.4)

The capacitance, $C(x)$, of this class of quartic-shaped-finger comb is a 4th order polynomial:

$$C(x) = C_{n0} - \gamma_1 x^2 - 0.5\gamma_3 x^4.$$

(B.5)

where the capacitance when the displacement is zero is

$$C_{n0} = \frac{2N\varepsilon_o h}{g_o}\left(2x_{ov} + \frac{x_{ov}^2}{x_{o1}} + \frac{x_{ov}^4}{2x_{o3}}\right),$$

(B.6)

the linear electrostatic spring constant is

$$\gamma_1 = -\frac{2N\varepsilon_o h}{g_o}\left(\frac{1}{x_{o1}} + \frac{3x_{ov}^2}{x_{o3}}\right),$$

(B.7)

and the cubic electrostatic spring constant is

$$\gamma_3 = -\frac{2N\varepsilon_o h}{g_o x_{o3}}.$$

(B.8)

Taking the derivative of the capacitance and multiply by $V_p^2/2$ give the electrostatic force,

$$F_e(x) = -\left(\gamma_1 x + \gamma_3 x^3\right)V_p^2.$$

(B.9)

where V_p is the voltage applied across the comb finger gap. The capacitance and the force are plotted in Figure B-7.

192
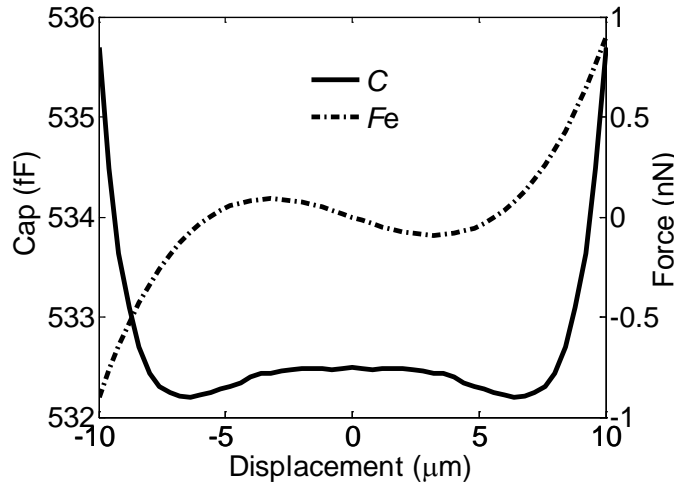
Figure B-7: Force-engagement and capacitance-engagement curves for the symmetrically-placed shaped comb.

The geometry-related parameters x_{o1} and x_{o3} are optimized to yield a maximum $|\gamma_3|/\gamma_1$ ratio [Choice of design parameters] given the fabrication constraints and the linear spring constant is chosen such that the saddle-node bifurcation amplitude is well below the stroke of the comb.

The analytic frequency response of this type of nonlinear resonator provides a high amplitude [Steady-state frequency response] bifurcation response shown in Figure B-8. The frequency down sweep indicated by the green arrow can possibly follow two directions: one bifurcates to the zero solution, the other follows the purple arrow to point F where a maximum stroke is reaches and then drops to zero again. This design can be used to explore a large-stroke saddle-node bifurcation from point D to E.
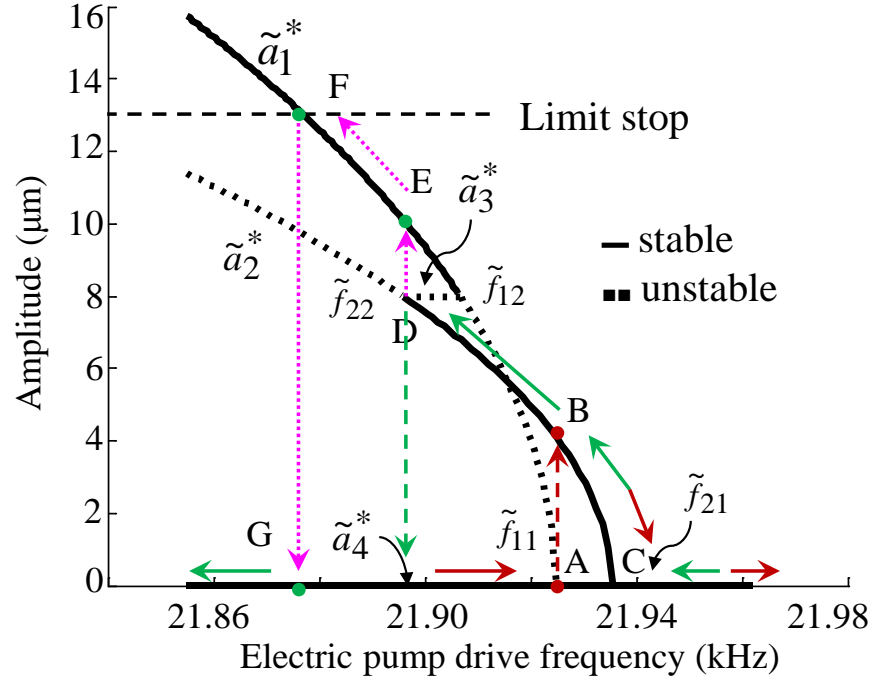
Figure B-8: Steady-state frequency response of the quartic-shaped-finger comb.

The device was successfully fabricated using the SOI-MEMS process. The experimental Future work validation can serve as a validation vehicle for large-amplitude saddle-node bifurcation. Applying the quartic-shaped-finger comb to the controller in Chapter 4, a bi-state bifurcation-point controller may be realized that works at large-displacement saddle-node bifurcations. It is possible to implement a amplitude-state controller that servos at the falling edge of the saddle-node bifurcation point. The design and modeling can be validated through behavioral modeling and by the closed-loop implementation with off-chip electronics. However, this type of bifurcation and its control are beyond the current scope of this thesis work.

(end)

APPENDIX C   SOI-MEMS FABRICATION PROCESS

C.1.   PROCESS FLOW

The shaped comb resonators are prototyped by a silicon-on-insulator MEMS (SOI-MEMS) process. The development of the SOI process is for MEMS ideation and prototyping and while this kind of process is now common, it represents a contribution of this thesis work by providing the capability at CMU.


(a)   (b)
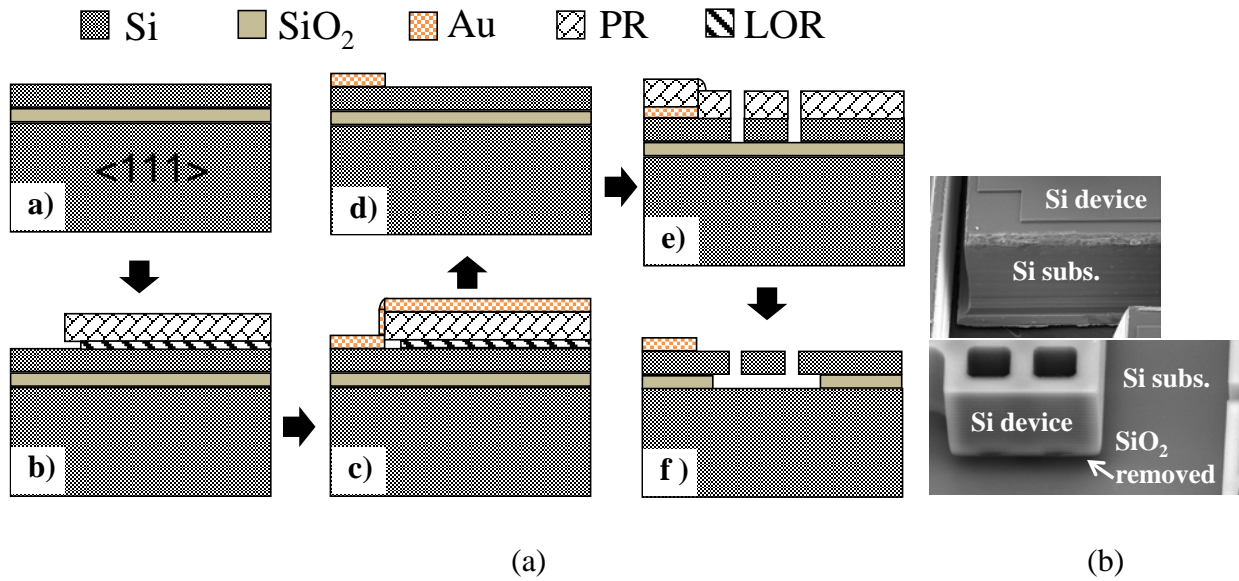
Figure C-1: (a) Schematic cross-section of the SOI process. (b) SEM of the released device cross-section.

The fabrication flow is schematically shown in Figure C-1. The process starts with a bare <u>Description of steps</u> SOI wafer [Figure C-1 (a)] with a 15 μm thick Si <111> 0.001~0.003 Ω-cm device layer, a 2 μm buried oxide layer (BOX), and a 480 μm handle substrate. The handle resistivity is 1~20 Ω-cm to avoid floating substrate potential. A lift-off process is developed in patterning the Au pads. In Figure C-1 (b), a bi-layer lift-off resist (LOR 5B) is used to create an undercut layer beneath the photoresist (PR) to limit sidewall deposition of metal in order to facilitate a clean lift-off. Electrical contact is realized through a sputtered 380 nm thick Cr / Au pad layer [Figure C-1 (c)]. The Si trenches to define the microstructures are formed with DRIE (Deep Reactive-Ion Etching) in Figure C-1 (e). The device is released by a timed BHF (buffered HF) etch of the BOX layer [Figure C-1 (f)], followed by DI water, IPA and methanol rinse to avoid stiction of the device to the substrate. A Tousimis Automegasamdri®-915B, Series B critical point drier had also been used in replace of the wet method to facilitate a stiction-free release.

C.2.   DETAILED RECIPES

C.2.1. AU PAD PATTERNING

The pad layer lithography is graphically described in Figure C-1 (a-d). The bi-layer resists used in this process are the LOR 5B resist and the AZ4210. The detailed recipe is listed in Table C-1.

Table C-1: Au pad layer patterning recipe using the LOR resist

Purpose	Process detail	Unit	Condition
Surface treatment	wash		acetone + IPA + DI
	dehydrate time	min	5~10
	dehydrate temp.	℃	185
LOR spin-coating	resist		LOR 5B
	LOR spin recipe		600 RPM, 10 s + 2500 RPM, 45 s; Ramp = 600 [†]
	LOR bake	min	5.5 (± 0.5)
	LOR bake temp	℃	185
	LOR thick	μm	0.7
	LOR undercut	μm	4.5~5.5
AZ4210 coating	resist		AZ4210
	res spin recipe		600 RPM, 6 s + 3000 RPM, 30 s
	soft bake	min	2
	res thick	μm	2.69
Litho	exposure type		Vacuum contact ("VAC" in MA-6)
	exposure	s	190
	developer		1:3 AZ400K
	develop	min	0.8~0.9
Bake	Hard bake		0.7min @ 100C
Surface treatment	descum	min	2
	BHF	s	45
Au sputtering	metal		Cr
	Cr recipe		10 min presputter + 45 s sputter
	Cr thickness	nm	10
	metal		Au
	Au recipe		1 min PS + 2min SP + 1 min PS + 2min SP + 30s PS + 2min SP + 30s PS + 2min SP
	Au thickness	μm	0.4
Lift-off	lift-off chemical		PG remover (PG)
	lift-off		PG overnight + IPA rinse + 5min US in PG + IPA + DI + Acet + PG + IPA + DI
	Piranha recipe		1 H_2SO_4: 1 H_2O_2
	Piranha time	min	10

† Recipe applicable on the Solitec Photoresist Spinner. The ramp has no unit. The higher the number is, the slower the acceleration is reached.

C.2.2. SILICON DRIE

The structural trenches to define mechanically isolated microstructures are formed with silicon DRIE in Figure C-1 (e). The detailed recipe is listed in Table C-2.

Table C-2: Silicon structure patterning recipe

Purpose	Process detail	Unit	Condition
Surface treatment	descum		if start wafer with previous PR striped
	HMDS oven		10min dehydration + 2min HMDS vapor
AZ4210 coating	resist		AZ4210
	res spin recipe	RPM	600 RPM, 6 s + 4000 RPM, 30 s
	soft bake	min	2
	res thick	μm	2.18
	pad mesa thick	μm	0.4
Litho	exposure type		Vacuum contact ("VAC" in MA-6)
	exposure	s	42.5
	developer		1:4 AZ400K
	develop time	min	1.0 (±0.5)
Si DRIE	DRIE recipe		stdaniso (12s etch + 8s passivation)
	DRIE cycles		31+6
	DRIE time	min	10.33+2
	DRIE depth	μm	16.8 (PR included, measured at the 100 μm dicing lane)

C.2.3. BUFFERED HF RELEASE

The device is released by a timed BHF etch of the BOX layer in Figure C-1 (f). The detailed recipe is listed in Table C-3.

Table C-3: Buffered HF release recipe

Purpose	Process detail	Unit	Condition
PR coating†	resist		AZ4620
	res spin recipe		600 RPM, 6 s + 2000 RPM, 45 s
	bake time	min	~15
	bake temperature	℃	gradually increase from 20 to 40 to 60 and finally to 90
Dicing	wafer dicing		
	die wash		2min ultrasonic in DI + 1min acetone (partial stripe PR) + DI + complete PR stripe in acetone + DI + piranha x 2
BHF	BHF release		50~60 min + DI x 2
Release method 1	deplete DI		IPA x 3, each time for 5 min
	release		use CO_2 critical point drier
Release method 2	wet release		acetone + IPA + methonal

† AZ4620 coating to cover the whole wafer to protect the devices from dicing particles

(end)

REFERENCES

[1] W. Zhang and K. Turner, "Application of parametric resonance amplification in a single-crystal silicon micro-oscillator based mass sensor," *Sens. Actuators A, Phys.*, vol. 122, no. 1, pp. 23–30, Jul. 2005.

[2] Z. Yie, M. A Zielke, C. B Burgner and K. L Turner, "Comparison of parametric and linear mass detection in the presence of detection noise", *J. Micromech. Microeng.* vol. 21 (025027), 2011.

[3] M. V. Requa, "Parametric resonance in microcantilevers for applications in mass sensing," Ph.D. dissertation, University of California, Santa Barbara, 2006.

[4] C.B. Burgner, W.S. Snyders, and K.L. Turner, "Control of MEMS on the edge of instability," *Solid-State Sensors, Actuators and Microsystems Conference (TRANSDUCERS),* pp.1990-1993, 5-9 June 2011.

[5] N. Kacem, S. Hentz, S. Baguet, and R. Dufour, "Forced large amplitude periodic vibrations of non-linear Mathieu resonators for microgyroscope applications," *International Journal of Non-Linear Mechanics*, vol. 46, no. 10, pp. 1347-1355, Dec. 2011.

[6] K. Turner, S. Miller, P. Hartwell, N. MacDonald, S. Strogatz, and S. Adams, "Five parametric resonances in a microelectromechanical system," *Nature*, vol. 396, no. 6707, pp. 149–152, Nov. 1998.

[7] C. Ataman and H. Urey, "Modeling and characterization of comb-actuated resonant microscanners", *J. Micromech. Microeng.*, vol. 16, no. 1, pp. 9–16, Jan. 2006.

[8] G. Prakash, A. Raman, J. Rhoads, R. Reifenberger. "Parametric noise squeezing and parametric resonance of microcantilevers in air and liquid environments," *Review of Scientific Instruments*, vol. 83, no. 6, pp. 065109-065109-12, Jun 2012.

[9] M. J. Thompson and D. A. Horsley, "Lorentz force MEMS magnetometer," in *Solid-State Sensors, Actuators, and Microsystems Workshop*, pp.45-48, 6-10 Jun. 2010.

[10] M. Koskenvuori and I. Tittonen, "GHz-range FSK-reception with microelectromechanical resonators," *Sens. Actuators A, Phys.*, vol. 142, no. 1, pp. 346-351, Mar. 2008.

[11] B. DeMartini, H. Butterfield, J. Moehlis, and K. Turner, "Chaos for a microelectromechanical oscillator governed by the nonlinear Mathieu equation," *J. Microelectromech. Syst.*, vol. 16, no. 6, pp. 1314–1323, Dec. 2007.

[12] B. DeMartini, J. Rhoads, K. Turner, S. Shaw, J. Moehlis, "Linear and nonlinear tuning of parametrically excited MEMS oscillators," *J. Microelectromechanical Systems*, vol.16, no.2, pp.310-318, April 2007.

[13] J. F. Rhoads, S. W. Shaw, K. L. Turner, and R. Baskaran, "Tunable microelectromechanical filters that exploit parametric resonance", *Journal of Vibration and Acoustics*, vol. 127, no. 5, pp. 423–430, 2005.

[14] H.B. Chan, M.I. Dykman, and C. Stambaugh, "Paths of fluctuation induced switching", *Physical Review Letters*, vol. 100, p.p.130602, 2008.

[15] A.H. Nayfeh, *Introduction to Perturbation Technique*, John-Wiley and Sons, 1981, pp. 234–256.

[16] C. Guo and G. K. Fedder, "Behavioral modeling and testing of a CMOS-MEMS parametric resonator governed by the nonlinear Mathieu equation," in *the 25th Int. Conf. Micro Electro Mechanical Systems, (MEMS 2012)*, pp. 535–538, Paris, France, 29 Jan–2 Feb 2012.

[17] C. Guo, K. M. Shah, and G. K. Fedder, "Electrically driven CMOS-MEMS nonlinear parametric resonator design using a hierarchical MEMS circuit library," in *Solid-State Sensors, Actuators and Microsystems Conference (TRANSDUCERS)*, pp. 2402–2405, 5–9 June 2011.

[18] J. Rhoads, S. Shaw, K. Turner, J. Moehlis, B. DeMartini, and W. Zhang, "Generalized parametric resonance in electrostatically actuated microelectromechanical oscillators," *Journal of Sound and Vibration*, vol. 296, no. 4–5, pp. 797–829, Oct. 2006.

[19] S. Adams, F. Bertsch, and N. MacDonald, "Independent tuning of linear and nonlinear stiffness coefficients," *J. Microelectromech. Syst.*, vol. 7, no. 2, pp. 172–180, 1998.

[20] L.A. Oropeza-Ramos, C.B. Burgner, and K.L. Turner, "Robust micro-rate sensor actuated by parametric resonance," *Sens. Actuators A: Phys.*, vol. 152, no. 1, pp. 80-87, 2009.

[21] T. Hirano, T. Furuhata, K.J. Gabriel, and H. Fujita, "Design, fabrication, and operation of submicron gap comb-drive microactuators," *J. Microelectromech. Syst.*, vol. 1, no. 1, pp. 52–59, 1992.

[22] B.D. Jensen, S. Mutlu, S. Miller, K. Kurabayashi, and J.J. Allen, "Shaped comb fingers for tailored electromechanical restoring force," *Journal of Microelectromechanical Systems*, vol. 12, no. 3, 373-383, 2003.

[23] O'Brien G J 2001 Actuator and method of manufacture *U.S. Patent 6307298.*

[24] Graham A B 2012 Method of forming non-planar membranes using CMP *U.S. Patent Application 0264301.*

[25] C. Guo, E. Tatar, and G. K. Fedder, "Large-displacement Parametric Resonance using a Shaped Comb Drive", in *the 26th International Conference on Micro Electro Mechanical Systems (MEMS 2013)*, pp. 173–176, Taipei, Taiwan, 20 – 24 Jan 2013.

[26] C. B. Burgner, L. A. Shaw, K. L. Turner, "A new method for resonant sensing based on noise in nonlinear MEMS," in *the 25th Int. Conf. Micro Electro Mechanical Systems, (MEMS 2012)*, pp. 511–514, Paris, France, 29 Jan–2 Feb 2012.

[27] M. V. Requa and K. L. Turner, "Precise frequency estimation in a microelectromechanical parametric resonator", *Applied Physics Letters*, vol. 90, p.p. 173508, 2007.

[28] C. Guo, G. Fedder, "A quadratic-shaped-finger comb parametric resonator," *Journal of Micromechanics and Microengineering*, vol. 23, no. 9, pp. 095007. 2013.

[29] J. Rhoads, S. Shaw, and K. Turner, "Nonlinear dynamics and its applications in micro- and nanoresonators," *J. Dyn. Sys., Meas., Control*, vol. 132, no. 3, pp. 034001, May 2010.

[30] C. E. Crockett, "An introduction to the method of averaging," Dept. of Mathematical Sciences, USAF Academy, Colorado Springs, CO, Rep. USAFA–TR 92–6, Dec. 1992.

[31] R. Baskaran, "Parametric resonance and amplification in single and coupled micro electro mechanical systems," PhD Thesis, University of California, Santa Barbara, September 2003.

[32] G. K. Fedder and Q. Jing, "A hierarchical circuit-level design methodology for microelectromechanical systems," *Circuits and Systems II: Analog and Digital Signal Processing, IEEE Transactions on*, vol. 46, no. 10, pp.1309–1315, Oct 1999.

[33] A.H. Nayfeh and D.T. Mook, *Nonlinear Oscillations*, John-Wiley and Sons, 1979, pp. 283–301.

[34] C. Guo and G. K. Fedder, "Bi-state control of a Duffing resonator on the falling edge of instability," in *Tech. Dig., Int. Conf. Solid-State Sensors, Actuators and Microsystems (TRANSDUCERS)*, Barcelona, Spain, Jun. 2013.

[35] C Guo and G K Fedder, "Bi-state bifurcation control of a shaped-comb parametric resonator", in *Proc. ASME 2013 International Design Engineering Technical Conferences*, Portland, Oregon, USA, August 4-7, 2013, pp DETC2013-13001.

[36] G. K. Fedder, S. Santhanam, M. L. Reed, S. C. Eagle, D. F. Guillou, M. S. C. Lu, and L. R. Carley, "Laminated high-aspect-ratio microstructures in a conventional CMOS process," *Sensors and Actuators A: Physical*, vol. 57, no. 7, pp. 103-110, 1996.

[37] W. Hemmert, M. Mermelstein, and D. Freeman, "Nanometer resolution of three-dimensional motions using video interference microscopy," in *the 12th Int. Conf. Micro Electro Mechanical Systems, (MEMS 1999)*, Orlando, USA, pp. 302–308, 17–21 Jan 1999.

[38] B. Halg, "On a nonvolatile memory cell based on micro-electro-mechanics," in *Micro Electro Mechanical Systems Workshop*, pp.172-176, 11-14 Feb 1990.

[39] C. Guo, G. Fedder, "Bi-state control of parametric resonance," *Applied Physics Letters*, under review for publication.

[40] C. Guo and G. K. Fedder, "Behavioral modeling of a CMOS-MEMS nonlinear parametric resonator," *J. Microelectromech. Syst.*, doi: 10.1109/JMEMS.2013.2262589, 2013.

[41] R. Schreier, G. Temes, Understanding Delta-Sigma Data Converters, John-Wiley and Sons, 2005.

[42] A. Wung, R.V. Park, K.J. Rebello, G.K. Fedder, "Tri-axial high-g CMOS-MEMS capacitive accelerometer array," in *the 21th Int. Conf. Micro Electro Mechanical Systems, (MEMS 2008)*, pp.876-879, 13-17 Jan. 2008.

[43] S. G. Adams, F. M. Bertsch, K. A. Shaw, P. G. Hartwell, N. C. MacDonald, and F. C. Moon, "Capacitance based tunable micromechanical resonators," in *8th Int. Conf. Solid-State Sensors and Actuators, (Transducers'95)*, Stockholm, Sweden, pp. 438–441.

[44] S. G. Adams, F. Bertsch, N. C. MacDonald, "Independent tuning of the linear and nonlinear stiffness coefficients of a micromechanical device," in *Micro Electro Mechanical Systems, (MEMS '96)*, pp. 32-37, 11-15 Feb 1996.

[45] S E Alper, Y Temiz, T Akin, "A compact angular rate sensor system using a fully decoupled silicon-on-glass MEMS gyroscope", *J. Microelectromech. Syst.*, vol. 17, no. 6, pp. 1418-1429, 2008.

[46] C. Guo and G. K. Fedder, "2-DoF twisting electrothermal actuator for scanning laser rangefinder application," in *the 24th International Conference on Micro Electro Mechanical Systems*, Cancun, MEXICO, pp. 1205-1208, Jan 23-27, 2011.

[47] Texas Instruments, "Pulse-width-modulation control circuits", TL5001 datasheet, Apr. 1994 [Revised Jan. 2002].

[48] R. Brennen, M. Lim, A. Pisano, and A. Chou, "Large displacement linear actuator," in *IEEE Solid-State Sensor and Actuator Workshop, 4th Technical Digest.,* pp.135–139, 4–7 Jun 1990.

[49] A. Raman, A. K. Bajaj, and P. Davies, "On the slow transition across instabilities in non-linear dissipative systems", *Journal of Sound and Vibration*, vol. 192, no. 4, pp.835-865, 1996.

[50] D.S. Greywall, B. Yurke, P. A. Busch, A. N. Pargellis, and R. L. Willett, "Evading amplifier noise in nonlinear oscillators", *Phys. Rev. Lett.* vol. 72, no. 19, pp. 2992-2995, 1994.

(This page is intentionally left blank)